Università degli Studi di Siena

Facoltà di Scienze Matematiche Fisiche e Naturali

Tesi di Dottorato in Fisica Sperimentale
PhD Thesis in Experimental Physics

XIX Ciclo

Precision Measurement of the Top Quark Mass at CDF

Candidate:		**Michele Giunta**
Supervisor:	Prof.	**Giorgio Bellettini**
Supervisor:	Dr.	**Georgui Velev**
Internal Supervisor:	Prof.	**Angelo Scribano**

Contents

Introduction

The announcement of the Top Quark discovery was made in 1995 at the Fermilab Tevatron, ten years after the W and Z discovery at CERN. The Top completed the present picture of the fundamental hadrons in nature, the six quarks and their antiquarks.

Since then, a strong effort has been pursued by the CDF and the DØ Collaborations to measure its properties better. The mass of the Top quark is enormously larger than that of the previously known quarks, about 170 GeV versus the about 4.5 GeV of the Bottom quark. The suspect that a complete picture of its properties might give a glimpse on new physics beyond the Standard Model is justified. Among these properties, by far the most significant and important one is its mass.

This Thesis details an on-going effort to measure the Top quark mass with a new method which could eventually allow to make the most precise measurement at the Tevatron.

We improve one of the standard mass analysis techniques, the Template Method. We apply to this method a statistical technique in order to recover a portion of the information contained in the data which is usually not exploited.

The idea of increasing the efficiency of a study is very common in the high-energy particle field, where huge economic and manpower efforts are needed over large timescales. The interest in the Physics itself goes frequently together with the effort in making an experiment more efficient.

The idea is either to speed-up the study, or to obtain better results with the same means (hardware, time, money, manpower, ...).

The present study is naturally located in this framework, since the measurement of a very important physic parameter is made by applying a new technique to enhance the analysis power.

Acknowledgements

Even if it doesn't happen frequently, I had three supervisors: Giorgio Bellettini, Angelo Scribano, Georgui Velev. I also had a Tutor who I could meet when I was at Fermilab: Guram Chlachidze.

I really appreciated, and I am grateful to him for that, Giorgio's patience and kindness in continuously taking care about my progress in this work, in reading, re-reading, re-re-re-reading (yes, three passages!) my notes and Thesis chapters, in keeping the group together, in discussing about particle special tendency of confusing the experimentalists. Once I went to Giorgio's office while he was very busy in reading some papers. I asked him if he had some time to discuss with me about backgrounds, and he answered: "I have no time at all, but for you I always can find it. Seat down.".

George (Georgui) is an expert guide in a work like the one presented here: he deeply knows either the physics either the analysis methods and the code to apply them. Actually he largely wrote it! Thanks George for the time you dedicated to untangle my many questions!

I also benefited from the friendly help by Guram, who introduced me to the CDF code and helped me in many cumbersome code-debugging sessions. It was also nice to lighten with him some strong work period with pleasant non-physics discussions. Guram always smiles, an this, believe me, is an additional help I received from him!

Many people gave their particular contribution to me and to this Thesis: I acknowledge Franco Bedeschi for having shown me that an unbiased statistical method can be affected by a bias (it's true, I'm not joking!), Aldo Menzione for his objective sight which helps to reduce problems back to reality, Giuseppe Latino for the long discussions about the evil of jets, Giovanni Punzi for discussing with me about the Fisherman's information owned by a W and other funny topics (especially statistical paradoxes), Fedor Prokoshin for having fought on the field with me against codes, Alberto Annovi for his brilliant comparison between track reconstruction and kinematical systems, Paolo Mastrandrea and Jose Garcia for wise and smart `ROOT` tricks, Chiara Ferrazza for clarifying to me many b and c tagging details and for correcting together with

me the always-wrong Kolmogorov-Smirnov ROOT routine, Gabriele Compostella for quickly solving CAF problems that could need years of brainstorming to us human people.

Impossible to forgive the dinners and evenings at Fermilab that, day by day, were the longed rewards to the hard work-days. What could these dinners be without (in random order) Paolo, GianPiero, Anna, Chiara, Jose, Stefano G&T, Alberto A&B, Fedor, Gianluca, Gabriele, Silvia, Melisa, Giusepp(e), Daniel, Youko, Marco, Fabrizio, Roberto?

I acknowledge Francesca for having encouraged and supported me during the beginning of my Ph.D. when all things seemed to be too difficult to be faced. She gave me very powerful tricks to do that.

I acknowledge Chiara for her ability to early detect my bad humor and change it in a smile. She also can teach to everybody how to deal with all that strange strings of letters and symbols which are printed on the pages of book!

I obviously thank my family who thought I could complete this Ph.D and gave me all the necessary tools, and I'm not talking about money!

The soundtrack of this work was provided by Rammstein, Megaherz and Eisbrecher.

Chapter 1

Top Quark Physics

1.1 The Standard Model

Our present understanding of the fundamental constituents of matter and of their interactions is expressed in a theory called the Standard Model (SM). The SM was developed in the 1960's and 70's and has been extensively tested experimentally. Whenever a prediction for an experimental observable could be made by the Model, excellent agreement with experiment was found [1].

The SM integrates two gauge theories: Quantum Chromodynamics (QCD), describing the strong interactions, and the electroweak (EW) theory of Glashow-Weinberg-Salam (GWS), which unifies the weak and the electromagnetic interactions. These are both quantum field theories, and therefore the Standard Model is consistent with both quantum mechanics and special relativity.

1.1.1 Particle Classification

The most basic question in studying the composition of matter is:

"which are the fundamental bricks of this world?"

Since science was born, humans tried to answer this question by using more and more sophisticated means. When new unstable particles could be produced at particles accelerators in the past century, a natural question was to what extent they could be considered *fundamental* [1]

In the SM there are two families of elementary particles, *fermions* (with spin 1/2) and *bosons* (with spin 1). There are 12 elementary fermions and their

[1] A particle can be considered elementary if no internal structure can be revealed. Therefore, for example, the nucleus could be considered elementary until its composition in terms of protons and neutrons was discovered.

associated antiparticles.
The 6 elementary fermions interacting by the EW force only are named leptons and the 6 ones interacting by both the EW and the strong force are named quarks.

Leptons The elementary leptons comprise three weak isospin doublets, the charged electron (of unit electric charge by definition) and its neutrino of zero charge, the charged muon and its neutrino, and the charged tau lepton and its neutrino. Being neutrinos electrically neutral, they only experience the weak force.

Quarks Also the elementary quarks comprise three weak isospin doublets, each with an "up" and a "down" element. Quarks are electrically charged. Within a doublet, the down-type quark has a unit of electric charge less then the up-type quark, the charges being $+2/3$ in the up and $-1/3$ in the down. The quark types are conventionally named "flavours".

The first doublet comprises the up and down quark flavours, the second comprises the charm and strange quarks, and the third the Top and beauty (or bottom) quarks (u,d,c,s,t,b). Quarks also carry a strong interaction charge which is called "color". Color is a triplet in color space with three projections of the same intensity, named *red*, *green*, *blue* such that a composition of these colors is color-neutral. Antiquarks carry anticolor charges. The strong force strenght is supposed to increase to infinity with increasing quark-quark distance (single free quarks were never observed), bounding quarks in color-neutral groups of three (called *barions*) or quark/antiquark pairs (called *mesons*); all barions and mesons are color composed so that to be globaly colorless.

Gauge Bosons The other fundamental particles, the gauge bosons, are the interaction mediators. The carrier of the electromagnetic force is the photon γ, which is massless and chargeless. The weak force is mediated by three vector bosons: W^+, W^-, Z^0, the strong force is mediated by gluons (g), which are an octet in color space. A spin 2 graviton is supposed to be the carrier of the gravitational force but has never been observed.

Each particle, elementary or not, has a corresponding anti-particle (indicated in the following with an upper bar) with opposite electric charge and magnetic moment. A neutral particle can be its own antiparticle (examples are the photon and the neutral pion).

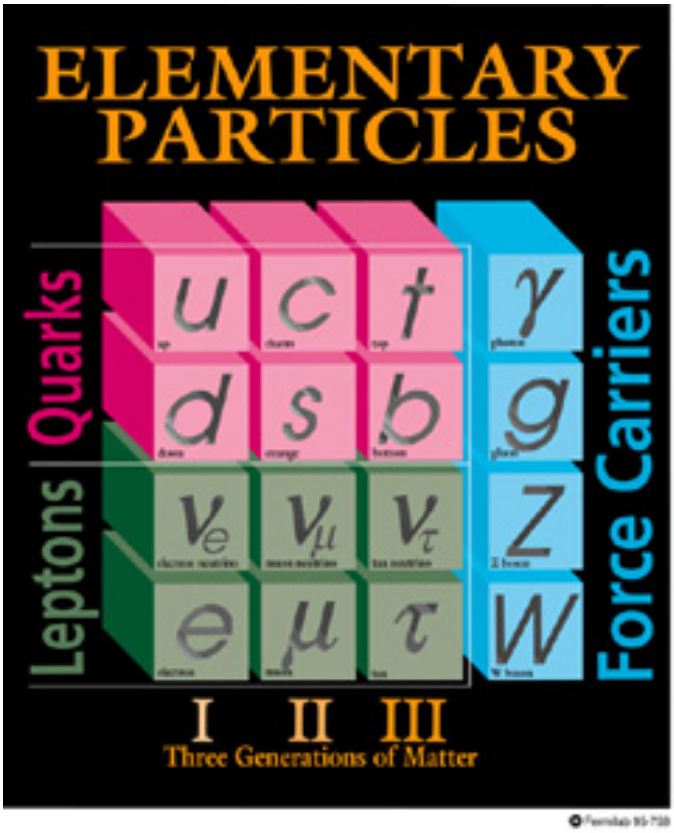

Figure 1.1: *The three families for elementary particles in the Standard Model Theory.*

1.1.2 The Electroweack Theory

The Electroweak (EW) theory unifies the weak isospin non-Abelian group $SU(2)$ and the weak hypercharge (Abelian) group $U(1)$ in $SU(2) \times U(1)$. The weak force distinguishes between left and right handed components of fermions and allows parity and charge conjugation violations in weak processes.

Before the EW unification in a single theory, the electromagnetic group had a $U_Q(1)$ symmetry generated by the electric charge and the weak interactions had a $SU_L(2)$ from the charged and neutral current interaction[2].

In order to preserve the $SU_L(2)$ symmetry when constructing the isospin triplet of weak currents, it became necessary to modify the U_1 electromagnetic group generator to account for the right-handed interactions. The hypercharge

[2] L stands for left-hand and Q for electric charge.

Y was then introduced to replace the electric charge as a group generator with the definition $Y = 2(Q + T_3)$, where Q is the electric charge and T_3 the third component of the particle weak isospin. The EW theory is built around the conservation of the weak isospin and weak hypercharge making the Lagrangian invariant under local gauge transformations. The gauge invariance of the electroweak Lagrangian is though complicated by the non-zero mass of the carriers of the weak force $W^{\pm}$ and Z_0. To generate those masses a weak-isospin doublet of fundamental scalar fields $\Phi = (\phi^-, \phi_0)$ was introduced in the Lagrangian with a potential like:

$$V(\Phi^\dagger\Phi) = \mu^2(\Phi^\dagger\Phi) + |\lambda|(\Phi^\dagger\Phi)^2 \tag{1.1}$$

where λ is the self coupling of the scalar field.
If μ^2 is chosen to be negative, the EW symmetry is spontaneously broken when the field is about its non-zero vacuum expectation value.

This mechanism, called *spontaneous symmetry braking*, was proposed by Peter Higgs in 1964 and permits to introduce the new field in the vacuum without loosing the local gauge invariance. It gives rise to the quark and W and Z bosons masses as well as to a massive and chargeless scalar gauge boson called *Higgs Boson*.
The Higgs boson interaction is thus responsible for generating the large masses for the weak gauge bosons ($m_W \simeq 80\ GeV$, $m_Z \simeq 91\ GeV$) explaining the short range of the weak force, and for lepton and quark masses including the extremely large mass of the Top quark ($M_{top} \simeq 170\ GeV$). The astonishing large value of the top quark mass justifies the suspect that this quark might play a special interface role between the SM and a more fundamental theory bejond it.

1.1.3 Quantum Chromodynamics

Quantum Chromodynamics (QCD) is a renormalizable theory modeled after the Quantum Electrodynamics (QED), the gauge theory of the electromagnetism. In QED the $U_Q(1)$ symmetry requires the electric charge to be conserved. Similarly, the QCD $SU(3)$ symmetry requires the *color* to be conserved. However, unlike QED, the gauge symmetry is non-Abelian, causing gluons to possess color charge and consequently interact with themselves as well as with quarks. Moreover, the additional gluon-gluon interactions cause the strong coupling constant α_s to have a qualitatively different behaviour with Q^2 (the interaction momentum transfer scale) than the QED coupling constant α_{QED}. To a first approximation in Q^2/Λ^2_{QCD} one has:

$$\alpha_s(Q^2) = \frac{4\pi}{11 - \frac{1}{2}N_f \ln \frac{Q^2}{\Lambda^2_{QCD}}} \tag{1.2}$$

where N_f is the number of flavors with mass less than Q and Λ_{QCD} is a parameter which, qualitatively, indicates the magnitude of the scale at which $\alpha_s(Q^2)$ becomes strong.

Λ_{QCD} is experimentally determined to be about 0.22 GeV.

Asymptotic freedom $\alpha_s(Q^2)$ becomes small at large Q^2, and a perturbative description of the strong force is possible. However, at small momentum transfer comparable with the mass of the light hadrons ($Q^2 \simeq 1\ GeV$), α_s becomes of the order unity and the perturbation approximation breaks down.

This large value of the coupling constant is the source of most mathematical complications and uncertainties in QCD calculations at low Q^2. On the other hand, it is of great importance that $\alpha_s(Q^2)$ tends to zero in the infinite Q^2 limit. This property, called *asymptotic freedom*, allows perturbation theory to be used in theoretical calculations to produce experimentally verifiable predictions for hard scattering processes.

Hadronization If colored particles are forced to be separated by a large Q^2 the energy density in the binding color string increases and energy is materialized into colored quark pairs. The quark coalescence into color singlets yields final state color-neutral hadrons rather than free quarks and gluons. Thus a hard scattered parton evolves into a shower of partons and finally into hadrons. This process is called *parton shower evolution* or *hadronization*.

1.2 The Top Quark

The Top quark of charge +2/3 is included in the Standard Model as the weak isospin partner of the charge −1/3 bottom quark in the third generation of elementary fermions. With its extraordinarly large mass of $\sim 170\ GeV$ the Top quark is the heaviest known elementary particle.

1.2.1 Top Quark Production

The Top quark was discovered during the Run 1 of the Tevatron collider in $p\bar{p}$ collisions at 1.80 TeV c.m.s. energy. With a mass larger than the W mass, the Top quark is expected to be produced at the Tevatron predominantly as $t\bar{t}$ pairs, 85% of the times from $q\bar{q}$ annihilation and 15% from gluon-gluon fusion [2] [3].

$$p\bar{p} \rightarrow t\bar{t} + X \tag{1.3}$$

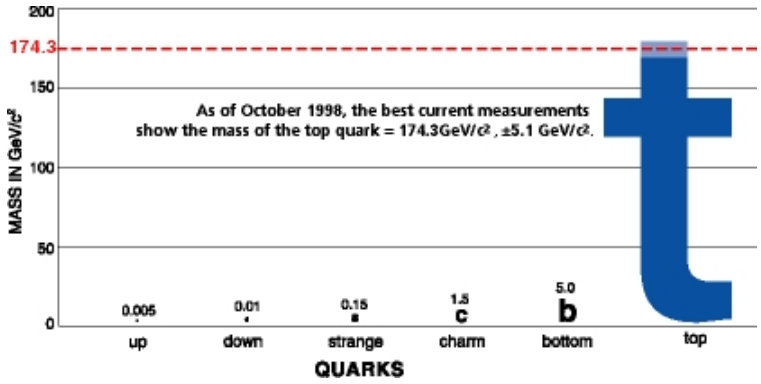

Figure 1.2: *The Top quark mass compared with other quark masses. The Top is about 38 times heavier than the second heaviest quark, the b.*

With a cross section about 3 times smaller, the Top quark is also expected to be produced as a single quark via the weak wirtual W-exchange process (see also section 4.3.1):

$$p\bar{p} \to t\bar{b} + X \tag{1.4}$$

$$p\bar{p} \to tqb + X \tag{1.5}$$

In the factorization approximation, all allowed parton-parton interaction channels contribute to the experimental $t\bar{t}$ production cross section to an amount depending on their distribution functions in the primary hadrons and by their QCD interaction cross section, as:

$$\sigma(p\bar{p} \to t\bar{t}) = \sum_{i,j} \int dz_i dz_j f_{i/p}(z_i, \mu^2) f_{j/\bar{p}}(z_j, \mu^2) \hat{\sigma}(ij \to t\bar{t}; \hat{s}, \alpha_s(\mu^2), M_{top}) \tag{1.6}$$

where the sum is over all partons: gluons, light quarks and antiquarks.

1.2.2 Top Quark Decay

The Top quark decay is mediated by the weak force.

The dominant Top quark decay branching ratio is $\mathcal{B}(t \to bW) > 0.998$ with a minimal contribution by $t \to Ws$, $t \to Wd$. These additional decay channels are allowed by SM [4], but are highly suppressed due to the very small values of the off-diagonal elements in the quark flavor mixing into weak eigenstates (the Cabibbo-Kobayashi-Maskawa CKM matrix).

The final states of the $t\bar{t}$ system are determined by the independent decays of the two W bosons from t and $\bar{t}$ decay:

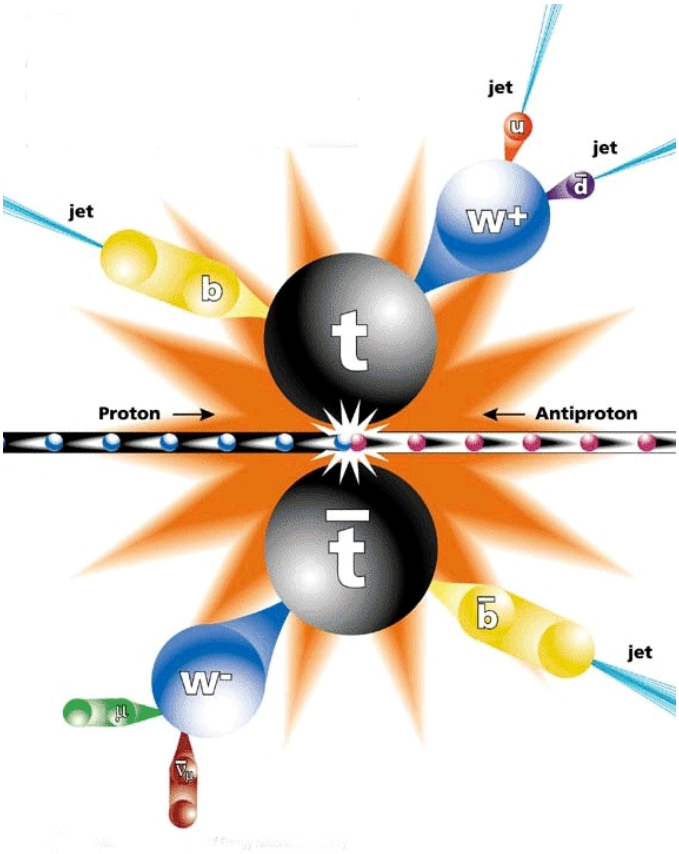

Figure 1.3: *The picture illustrates $t\bar{t}$ production at tree level by $q\bar{q}$ annihilation followed by the pair decay into the muon + jets channel.*

$$t\bar{t} -> (bW^+)(\bar{b}W^-) \tag{1.7}$$

Each of the two produced W bosons can decay leptonically in the three modes:

$$W^-(W^+) \rightarrow e^-(e^+)\bar{\nu_e}(\nu_e) \tag{1.8}$$

$$W^-(W^+) \rightarrow \mu^+(\mu^-)\bar{\nu_\mu}(\nu_\mu) \tag{1.9}$$

$$W^-(W^+) \rightarrow \tau^+(\tau^-)\bar{\nu_\tau}(\nu_\tau) \tag{1.10}$$

(with the same branching ratios) or hadronically into a pair of the two lower doublets quarks

$$W^-(W^+) \rightarrow d\bar{u}(u\bar{d}) \tag{1.11}$$

Decay mode	BR	Channnel category
$t\bar{t} \to (q\bar{q'}b)(q\bar{q'}\bar{b})$	36/81	Full-hadronic
$t\bar{t} \to (q\bar{q'}b)(e\nu\bar{b})$	12/81	Lepton + jets
$t\bar{t} \to (q\bar{q'}b)(\mu\nu\bar{b})$	12/81	Lepton + jets
$t\bar{t} \to (q\bar{q'}b)(\tau\nu\bar{b})$	12/81	Lepton + jets (τ)
$t\bar{t} \to (e\nu b)(\mu\nu\bar{b})$	2/81	Dilepton
$t\bar{t} \to (e\nu b)(\tau\nu\bar{b})$	2/81	Lepton + jets (τ)
$t\bar{t} \to (\mu\nu b)(\tau\nu\bar{b})$	2/81	Lepton + jets (τ)
$t\bar{t} \to (e\nu b)(e\nu\bar{b})$	1/81	Dilepton
$t\bar{t} \to (\mu\nu b)(\mu\nu\bar{b})$	1/81	Dilepton
$t\bar{t} \to (\tau\nu b)(\tau\nu\bar{b})$	1/81	Dilepton (τ)

Table 1.1: *Relative branching ratios (BR) for the different decay modes of the $t\bar{t}$ system.*

$$W^-(W^+) \to s\bar{c}(c\bar{s}) \tag{1.12}$$

Therefore we can have a fully-leptonic, fully-hadronic or semileptonic $t\bar{t}$ final state, depending of the W's decay paths. The branching ratios (BR) of the various decay channels are reported in table 1.1.

Different channels produce different experimental signatures in the detector. The leptonic channels involving τ's are difficult to isolate because of the poor tau signature. The fully hadronic channels suffer from a large QCD background of multijet states. The measurement of the Top mass in the dilepton channel is complicated by the two non-observable neutrinos in the final state. The single-lepton final states involving electrons or muons, which can be fully reconstructed from the experimental observables and are best suited for the Top mass measurement will be described in section 4.3.

1.2.3 Top Quark Cross Section

The $t\bar{t}$ production cross section has been calculated to $O(\alpha_s^3)$ in perturbative QCD (figure 1.5). An estimate at order $O(\alpha_s^4)$ was also made with soft gluon resummation techniques. Higher order corrections are expected to increase the tree-level cross section by $\sim$ 30%. For a Top mass of 170 GeV the theory predicts a cross section of $\sigma_{t\bar{t}} \sim 6$ pb. The expected Top quark rate at the Tevatron is thus extremely weak. Since the total $p\bar{p}$ inelastic cross section is about 80 $mbarn$, we expect one Top quark event every about 10^{10} interactions. This huge background of undesired events is a real challenge in the search for

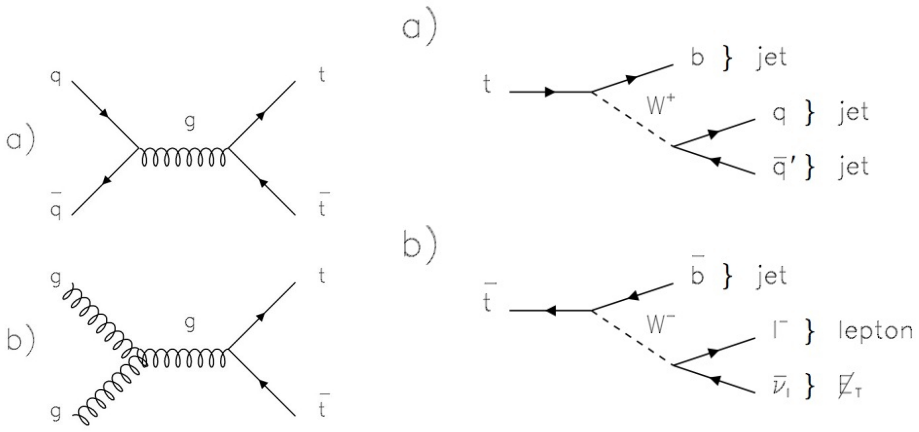

Figure 1.4: *Left: the picture shows the two $t\bar{t}$ Top production Feynman diagrams which dominagte at the tevatron. Diagram a) is parton-parton annihilation which occurs $\simeq 85\%$ of times, diagram b) shows the gluon-gluon fusion process which occurs $\sim 15\%$ of times. Right: diagram a) shows the hadronic W decay channel, diagram b) shows the leptonic W decay channel. In all $t\bar{t}$ final states channels two jets initiated by b-quarks are present.*

top events.

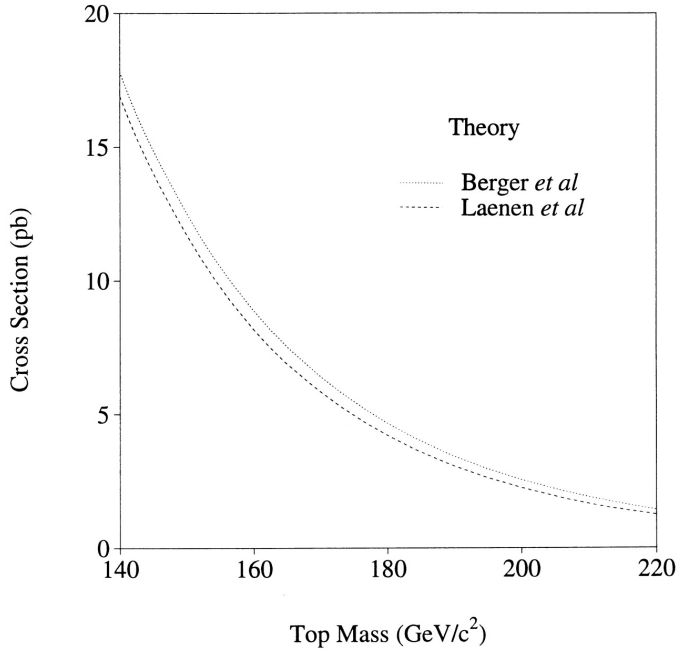

Figure 1.5: *Cross section of Top quark production as a function of Top mass.*

The most recent cross-section measurements by CDF are reported in figure 1.6.

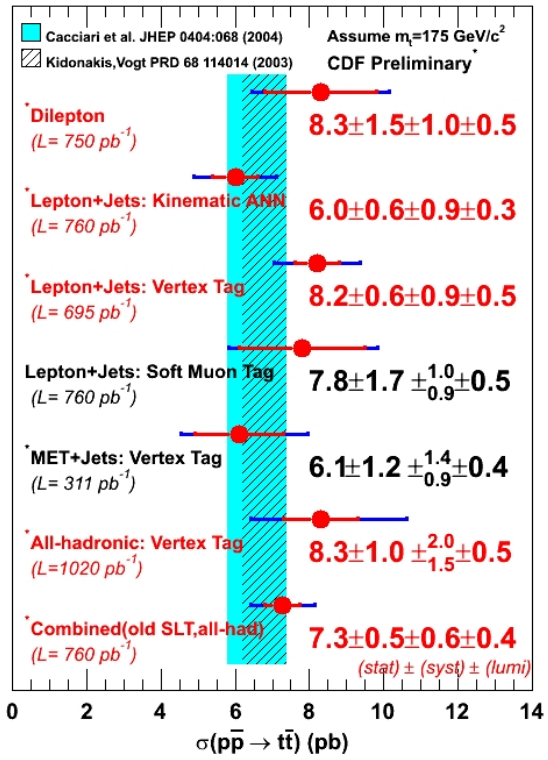

Figure 1.6: *Cross section measurements by CDF compared with theoretical predictions (shaded). This plot is updated to March 2007.*

1.3 Importance of Top Mass Measurement

Before the discovery of vector bosons $W^{\pm}$ and Z_0, a fairly reliable prediction of their mass was available since fits to neutrino and charged lepton scattering at low energy had provided the Weinberg angle θ_W. The W,Z production cross sections could therefore be calculated in terms of the Fermi coupling constant G_F and of the Weinberg angle. The Higgs boson mass is not predited in the SM, but some indication on its value can be derived from the size of virtual Higgs exchange loops in next to leading order (NLO) diagrams of a number of EW observables.

These higher order diagrams impact significantly the W and the Top masses, since the Higgs coupling to fermions and bosons is proportional to their mass. Measuring with the highest possible precision the W and Top masses thus pro-

vides in the SM bounds to the Higgs mass. This situation is illustrated in figure 1.7.

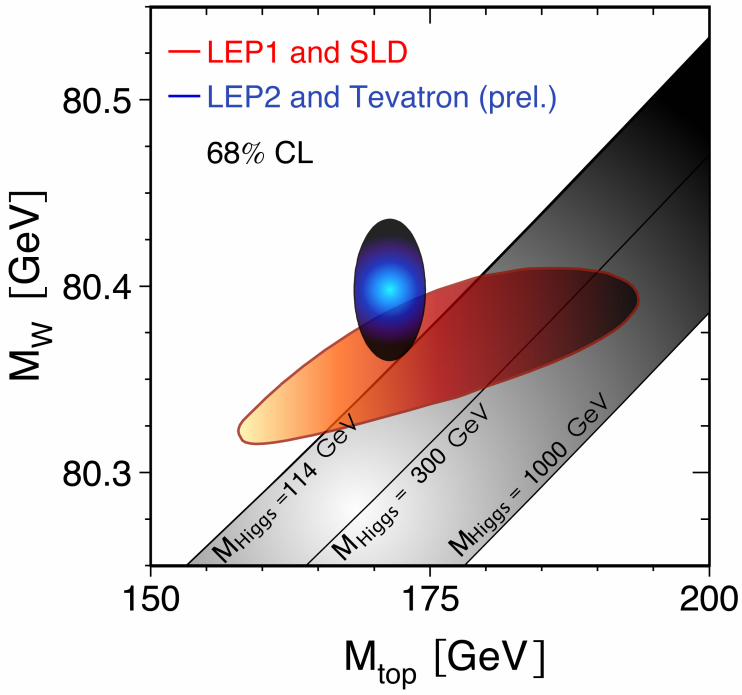

Figure 1.7: *Relationship between M_W and M_t as a function of the Higgs mass. Expectations for a number of H masses are shown within the shaded band. Available EW data and Run1 Tevatron measurements of M_W and M_{top} favour low M_H values. The small ellipse (1σ radius in the two observables) indicates the expected constraint by higher precision measurements of M_W, M_{top} at the end of Run 2.*

An accurate measurement of M_{top} is also important in some extension of the SM. In the minimal supersymmetric extension of the SM there is an upper bound on the mass of the lightest neutral Higgs h which depends strongly on the Top mass. Given the present value of M_{top} one expects that M_H should be below 140 GeV. If no h would be found in the future below this mass, the minimal SUSY would be ruled out.

1.4 Top Lifetime

From the dominant Top decay into the $t \rightarrow Wb$ channel the Top lifetime and width can be derived as a function of M_{top} in the limit $M_{top} >> M_W$. From the equation:

$$\Gamma(t \to bW) = \frac{G_F M_{top}^3}{8\pi\sqrt{2}} |V_{tb}|^2 \simeq 170\ MeV \Big(\frac{M_{top}}{M_W}\Big)^3 \tag{1.13}$$

one derives an approximate Γ value: for $M_{top} \simeq 2M_W$ we get $\Gamma(t) \simeq 1\ GeV$, then $\tau_t \simeq 10^{-24} s$. Thus, the Top quark will decay before it has a chance to hadronize.

Chapter 2

Reaching the Top

2.1 Indirect Evidence for the Existence of the Top Quark

Well before direct evidence for the Top quark was claimed by CDF in 1994, the scientific community was convinced that the Top quark existed. The search for the Top begun soon after the discovery of the Bottom quark. The Bottom quark was discovered in 1977 in a fixed target experiment at Fermilab[1] where a resonance at $\simeq 9.5\ GeV$ was observed in the μ-pair mass spectrum. The resonance, which was named Υ and was followed by several excited states of slightly higher masses, was soon understood as a quark-antiquark bound state of a new quark, which was named Bottom (or Beauty).

In the study of the meson families of the new quark it was also soon understood that the Bottom was the down-type member of a new doublet. It was already well known that weak decays of the second generation quarks occur via charged current (as in $s \rightarrow u$), while neutral current decays are highly suppressed[2]. The Bottom quark was observed to obey the same rule, with nearly exclusive decays to the upper member of the second doublet, the Charm quark. Therefore, the Bottom was the lower member of a third generation.

A robust although indirect argument for the existence of the Top was the observation that the weak isospin of the Bottom is 1/2. This parameter could be measured by the polar angular distribution of beauty jets in the electron-positron annihilation at $\simeq 40\ GeV$ cms energy. The weight of the asymmetrical $\cos\theta$ term in this distribution is the quark isospin, which was measured to be 1/2 to within 10%. In a 1/2 isospin multiplet there are two terms. The Top quark would be the second one.

[1] By the 288 Experiment team headed by Leon Lederman.

[2] This process is known as FCNC, Flavour Changing Neutral Current.

Another observable which depends on the beauty weak isospin is the Z^0 coupling to the b quark. The measured Z^0 partial decay width into b-pairs to the full hadronic width is:

$$\Gamma(Z^0 \to b\bar{b}) = 384 \pm 4 \; MeV \tag{2.1}$$

fully consistent with the value of 381 MeV expected for $I_3^b = 1/2$ and incompatible with the value of 24 MeV expected if $I_3^b = 0$. Alltogether, the Top quark ought to exist for the Standard Model to survive.

2.2 Past Direct Searches for Top Quark

2.2.1 e^+e^- machines

An electron-positron machine can produce top pairs in the annihilation process as $e^+e^- \to t\bar{t}$. The expected signal would be much freeer from background than at hadron colliders because leptons (are supposed to) have no internal structure. Past e^+e^- machines were not powerful enough to produce top pairs but were able to set increasing lower limits to its mass.
Around 1980 at the TRISTAN collider (Tsukuba, Japan) a lower limit of 30 GeV at 95% CL was obtained. In 1990 a limit $M_{top} > 42$ GeV was set at LEP. This is still now the strongest constraint obtained in e^+e^- production. The search for Top was not performed at LEP2, where the energy could only reach a mass limit of about 100 GeV, because the Top had already been discovered at a larger mass at the Tevatron. Accurate studies of $t\bar{t}$ pairs are an important program at the electron-positron International Linear Collider of 500 GeV initial energy which is presently planned (section 2.5).

2.2.2 $p\bar{p}$ Machines

UA1/UA2 searches

Single production in the decay $W \to t\bar{b}$ was expected to be the dominant Top production process if the Top mass were lower than ~ 75 GeV (which is about the difference $M_W - M_b$). Hopes for discovery were raised by a fake signal in the UA1 experiment[3] at $M_{top} \simeq 40$ GeV at the CERN $p\bar{p}$ collider $Sp\bar{p}S$. in 1990 UA1 set a limit $M_{top} > 56$ GeV from the non-observation of the decay $W \to t\bar{b}$ in both the electron and the muon channels.

[3]This is an interesting example of the difficulties facing searches of new particles at hadron colliders. Due to the internal structure of the projectiles a large number of competing processes generate a dangerous physical background.

In 1992 the UA2 experiment extended the limit to $M_{top} > 69\ GeV$, based on the non observation of off-shell W decays in the electron channel in the W candidate sample. In the same year the CDF experiment at the Fermilab Tevatron Collider, at $\sqrt{s} = 1.8\ GeV$) obtained a lower mass limit of $M_{top} > 91\ GeV$ by searching both for single and for pair production of top.
This limit was higher than the kinematic limit allowed for top in the decay of real W's, and forced the search at the CERN SpS collider, whose energy was too low to allow for an appreciable pair production rate at higher Top masses, to be stopped. The last lower mass limit before evidence for Top was announced by CDF, was obtained as $M_{top} > 131\ GeV$ at $95\%CL$ by the DØ experiment at the Tevatron in January 1994.

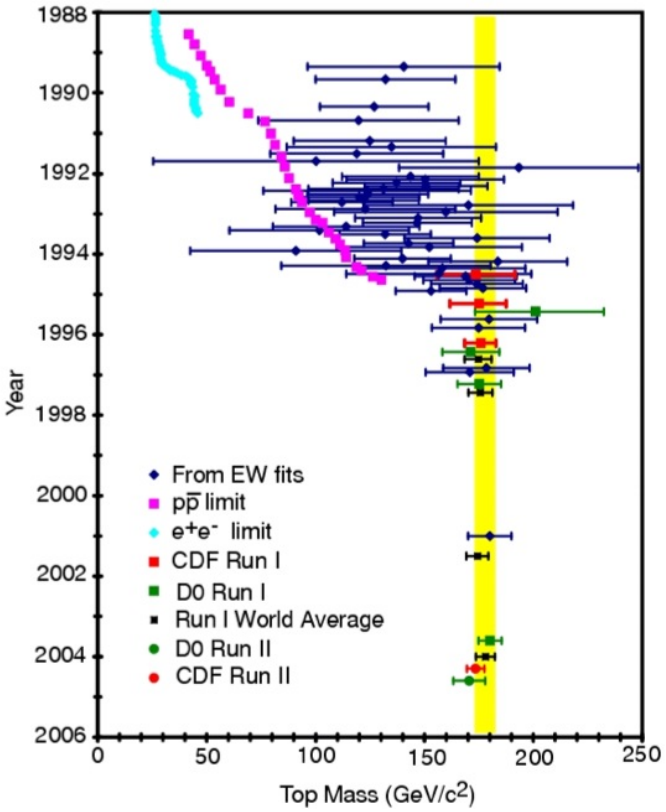

Figure 2.1: *Top quark mass SM predictions and direct measurements as a function of time. The vertical stripe ($\pm 1\sigma$ wide) represents the average mass from measurements made at the Tevatron in Run 1. A few Run 2 measurements (year 2004), which are consistent with Run 1 findings, are also shown.*

2.3 1994: Direct Evidence of the Top Quark

Evidence[4] for the existence of the Top quark was first obtained by CDF in June 1994 from the analysis of 19.3 pb^{-1} of data [5].

The evidence was provided by the excesses of $t\bar{t}$-like events in two channels. An excess over expectations from known processes was found in events passing the cuts to select final state with both W's decaying leptonically ("dilepton events"). Another excess was found in final states with a single W leptonic decay accompanied by beauty-tagged jets as expected in $t\bar{t}$ events. For this study, two b-tagging methods were used[5].

Two dilepton events where found while the expectation from non-Top processes was 0.54±0.28 events. 6 single lepton events containing jets SVX b-tagged by a displaced vertex were found, while the expectation from background or mistags was 2.3 ± 0.3. 7 events containing jets SLT b-tagged by a lepton in the jet were also found, while the background expectation was 3.1 ± 0.3 events. The combined probability for backgrounds to generate these fluctuations was computed to be 0.26%, corresponding to 2.8 sigma for a gaussian distribution. In addition, seven single lepton events could be fully reconstructed as $t\bar{t}$, and a Top mass of $174 \pm 10^{+13}_{-12}$ GeV was obtained by fitting their mass distribution. This result, even if insufficient to claim the Top discovery, raised a great enthusiasm in the scientific community and was a strong incentive for an aggressive analysys of the data being collected.

2.4 1995: The Top Quark Discovery

The Top quark was discoved assuming its decay channels to be as predicted by the SM, i.e. $t \to W + b$, $\bar{t} \to W + \bar{b}$, followed by independent decays of the two W's. Within the large errors, the observed rates in the dilepton (both W's decaying into e, μ and neutrino) and in the single lepton channel were consistent with the SM, as well as the $t\bar{t}$ production cross section. On the other hand, its amazingly large mass of about 170 GeV, although indirectly suggested by fits to electroweak observables, came to a big surprise.

The Tevatron was the only machine with enough center of mass energy and luminosity to be able to shoot at discovering a Top of such a large mass. Enough

[4]Evidence for a new phenomenon is customarely claimed when a $\simeq 3\sigma$ anomaly is found over expectations. A discovery can be claimed when the anomaly reaches 5σ.

[5]These were SVX tagging, when a secondary vertex is indicated by the Silicon Vertex detector (section 4.4.3) and SLT tagging for Soft Lepton Tagging where a lepton is found in one of the event jets.

statistics had been collected by CDF in March 1995 ($67\ pb^{-1}$) to be able to turn the evidence of the previous year into a discovery. At that time also the DØ collaboration had reached the same result.

The 1995 CDF result was based on the observation 6 dilepton events and of 37 b-tagged events in the single lepton channel (27 being SVX tagged and 23 SLT tagged, with 13 double tags). These observations were equivalent alltogether to a 4.8σ fluctuation of background.
The increaed statistics allowed an improved measurement of the Top mass, $176 \pm 8(stat) \pm 10(syst)\ GeV$. The production cross section was $6.8^{+3.6}_{-2.4}\ pb$, fully consistent with SM predictions.

2.5 A Glimpse on The Future: LHC and ILC

The Large Hadron Collider (LHC) is a $\sqrt{s} = 14\ TeV$ proton-proton collider under construction in the former LEP tunnel at CERN. It is espected to start operation in 2008. Its design luminosity is $\sim 10^{34}\ cm^{-2}s^{-1}$. At these energy and luminosirty the Top pair production is expected to be close to $40000/year$, i.e. about 100 times the maximum Tevatron rate. Therefore the LHC can be considered a $t-$factory. High precision measurements of Top properties can be expected with confidence.

The ILC (International Linear Collider) is presently (year 2007) only a preliminary project, but in the HEP community many efforts and ideas are converging to it. The machine will consist of two aligned electron/positron LINACs pointing to the interaction zone, for a total length of $30 - 40\ Km$. The design luminosity is $3.4 \cdot 10^{34}\ cm^{-2}s^{-1}$ at the initial energy of $\sqrt{s} = 500\ GeV$, upgradable to $\simeq 1\ TeV$. The luminosity at the $t\bar{t}$ threshold ($\simeq 350\ GeV$) will be about $2 \cdot 10^{34}\ cm^{-2}s^{-1}$, and will allow detailed studies of the Top quark properties in very favourable background conditions.

Chapter 3

The Tevatron and the CDF Detector

Figure 3.1: *An airplane view of the Fermilab laboratory. The ring at the bottom of the figure is the Main Injector, the above ring is the Tevatron. On the left are clearly visible the paths of the external beamlines: the central beamline is for neutral beams and the side beamlines are for charged beams (protons on the right, mesons on the left).*

High Energy Physics (HEP) can be studied in cosmic ray interactions, where

the primary particle energy can reach 10^{20} eV. However, events at the highest energies are extremely rare and are not under our control. We can produce high energy interactions of nuclear particles in the laboratory by means of particle accelerators, providing a much higher event rate and under much cleaner experimental conditions, albeit at less extreme reaction energies.

The largest particle accelerator ever built was LEP, an e^+e^- ring which reached the C.M.S[1] energy $\sqrt{s} = 205$ GeV running in a 27 km circular underground tunnel close to the city of Geneva (Switzerland). After the shut-down of LEP at the end of the year 2000, the largest machine presently in operation is the **Tevatron**, a $p\bar{p}$ collider reaching the energy of $\sqrt{s} = 1.96$ TeV in a 6.4 Km ring. The Tevatron is located about 50 km west of Chicago (USA) in Fermilab, a scientific laboratory run by a consortium of universities (URA) and by the University of Chicago ("Fermi Research Alliance") on behalf of the American Department of Energy (DOE).

Two detectors along the Tevatron collider collect physics events: CDF and DØ. After the first evidence for the existence of Top quark shown by CDF in 1994, the CDF and DØ Collaborations announced the discovery the Top quark in 1995.

At present (year 2007) the Large Hadron Collider (LHC) is being built at CERN in the LEP tunnel. This new machine will start operating in late 2007 and will eventually reach an energy of $\sqrt{s} = 14$ TeV.

3.1 The Tevatron

The Tevatron is the final and largest element of the Fermilab accelerator complex, whose structure is illustrated in figure 3.2. The Tevatron works primarily as a $p\bar{p}$ collider. However, it can also accelerate a single proton beam and operate in fixed target mode to provide a number of neutral and charged particle beams. The Tevatron collider obtained the first collisions in 1985. In the course of time it provided several physics runs as listed in table 3.1.

3.1.1 H^- Source

A 25 KeV H^- electrostatic source provides negative hydrogen ions.

[1] Center of Mass System.

Run	Period	Int Lum pb^{-1}
First Test	1997	0.025
Run 0	1988-1989	4.5
Run 1A	1992-1993	19
Run 1B	1994-1995	90
Run 1C	1995-1996	1.9
Run 2A	2001-2004	400
Run 2B	2004-	>2000

Table 3.1: *Integrated luminosity delivered by Tevatron in its physics runs. Run2B is stilll in progress.*

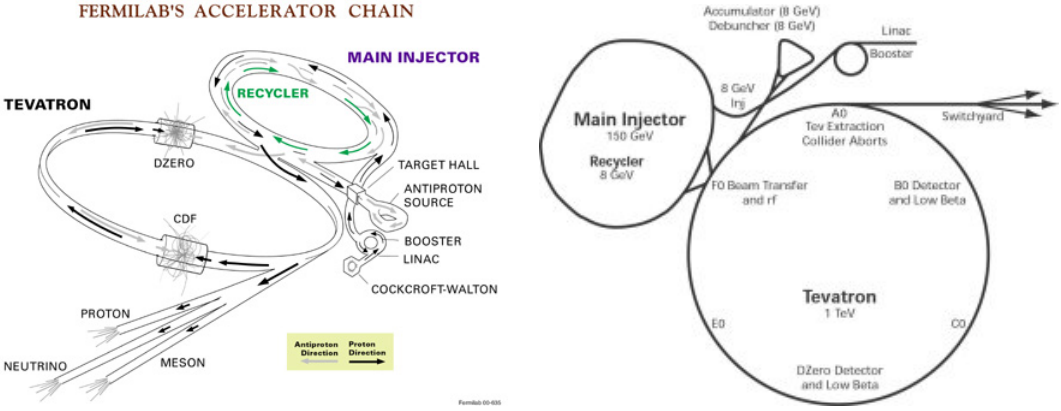

Figure 3.2: *Layouts of the acceleration chain at Fermilab Tevatron, from the source to the collision.*

3.1.2 Cockcroft-Walton Electrostatic Accelerator

The proton acceleration cycle begins with a Cockcroft-Walton electrostatic accelerator (see figure 3.3) feeding a linear accelerator with H^- at an energy of 750 KeV.

3.1.3 Linac

The Linac accelerates negative proton ions up to 400 MeV energy. The linac was upgraded to this energy in 1993 when the final energy was doubled, as well as the number of protons per bunch. Figure 3.4 (left) shows a portion of the Linac accelerator.

3.1.4 Booster

Negative ions are stripped at the linac exit through a carbon foil and bare protons are delivered to the Booster. This is a 8 GeV syncrotron 150 m in

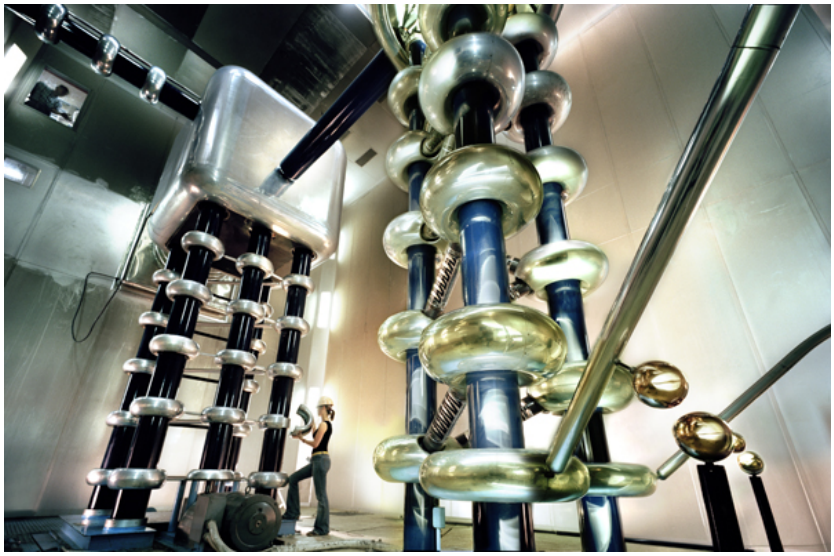

Figure 3.3: *The Cockcroft-Walton accelerator is the starting point of the proton acceleration chain.*

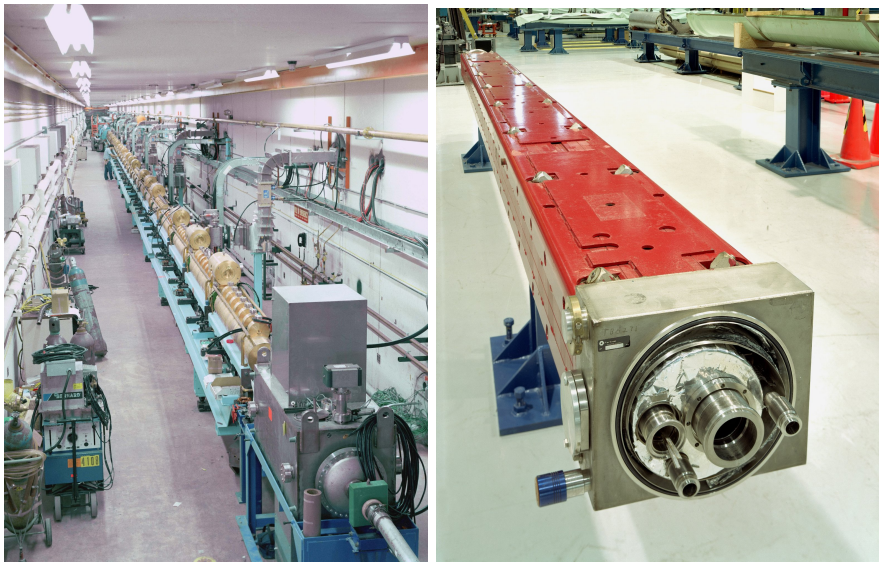

Figure 3.4: *Left: upstream view of the* 400 MeV *section of the Linac. Right: Tevatron Superconducting Dipole Magnet.*

diameter with a design maximum frequency of 15 Hz. The Booster trasfers protons to the Main Injector with an efficiency of $\sim 75\%$. Figure 3.5 shows the Booster tunnel.

Figure 3.5: *The Booster tunnel. A klystron is visible in the center of the picture.*

3.1.5 Main Injector

The Main Injector, completed in 1999 for Run 2, is located in a 3 Km circumference tunnel (which houses also the antiproton Recycler, see section 3.1.6 and figure 3.6), and is approximately tangent to the Tevatron. The Main Injector has a number of functions:

- It accelerates protons from 8 GeV to 150 GeV and feeds them to the Tevatron (in the clockwise direction).
- In the antiproton production phase it accelerates protons to 120 GeV. Protons are extracted and directed to the antiproton production target. Antiprotons are accumulated and cooled at 8 GeV in the Antiproton Source.
- It receives antiprotons from the Antiproton source, boosts their energy to 150 GeV and transfers them to the Tevatron (in the anti-clockwise direction).

The Main Injector maximum stored beams are $\sim 3{\cdot}10^{13}$ protons and $\sim 2{\cdot}10^{12}$ antiprotons. Beams are stored in 36 bunches in the Tevatron.

3.1.6 Antiproton Production and Recycler

Antiprotons ($\bar{p}$) are produced from the 120 GeV proton beam extracted from the Main Injector and focused on a nikel target.

Antiprotons are collected at 8 GeV with wide acceptance around the forward direction, injected into a Debuncher Ring, debunched into a continuos beam

Figure 3.6: *Main Injector (blue magnets on bottom) and the Recycler (green magnets on top) in the Main Injector tunnel.*

and stochastically cooled. The beam is then transferred between cicles (about 2" long) to the Accumulator were antiprotons are stored at a rate of about $25 \cdot 10^{10}$ $\bar{p}/hour$ (improvements in the storage rate are still being made).

Stacking within the accumulator acceptance is limited to a stored beam of about 10^{12} antiprotons. The accumulated beam is then transfered to the large acceptance Recycler, an 8 GeV permanent magnet ring housed in the Main Injector tunnel which has an acceptance about twice as large as the accumulator. In normal conditions every $30'$ the Recycler receives about $2 \cdot 10^{11}$ antiprotons from the Accumulator with a current of about 10 mA. Recently (2005) the *electron-cooling* technique was succesfully applied to the Recycler to cool the antiproton beam by a 4.3 MeV electron beam, which is provided by a Pelletron accelerator adjacent to the ring.

3.1.7 Tevatron

The Tevatron is a 1 Km-radius circular syncrotron employing superconducting bending magnets (figure 3.4, right), where the protons and antiprotons beams orbit in the same pipe in opposite directions. Undesired bunch crossings are avoided by electrostatic separators.

The Tevatron receives protons and antiprotons at 150 GeV and ramps[2] them

[2]The magnetic field is ramped up together with the energy in order to mantain the revolution radius constant. The final condition when the magnetic field is maximum and is kept

to 980 GeV (in Run 2) where they are kept circulating in opposite directions at constant energy for physics runs lasting up to $\sim$ 30 hours. Stable running conditions and data-taking by the experiments are reached after beams are scraped with remotely-operated collimators to remove the beam halo.

The beam revolution time is 21 μs. The beams are split in 36 bunches organized in 3 trains each containing 12 bunches (see figure 3.7). Within a train the time spacing between bunches is 396 ns. An empty sector 139 buckets-long (2.6 μs) is provided in order to allow the kickers to raise to full power and abort the full beam into a dump in a single turn. This is done at the end of a run or in case of an emergency.

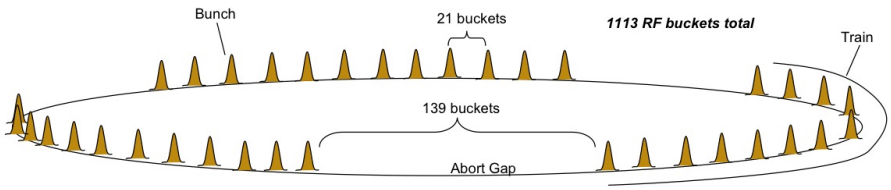

Figure 3.7: *Bunch structure of the Tevatron beams in Run 2.*

During data-taking runs the luminosity decreases approximately exponentially with time (figure 3.8, right). The record initial luminosity reached by the Tevatron as of March 2007 has been about $286 \cdot 10^{30}\ cm^{-2}s^{-1}$.

Figure 3.8 shows the luminosity integrated in Run 2 up to summer 2006 (left) and an example of time dependence of the luminosity during a store together with delivered and acquired integrated luminosity (right).

Figure 3.9 shows the weekly integrated luminosity during the same Run 2 period as a function of time.

At the end of a run, when the luminosity is too low to allow a significant data-taking (tipically $13 \cdot 10^{30} cm^{-2}s^{-1}$), the beams are aborted and the *shotsetup* procedure is started to prepare for a new store. In optimal conditions runs last about 30 hours.

A number of reasons can cause unwanted early termination of runs. Typical failures are a magnet quench[3], a vacuum leak, a power supply failure.

constant is called *flattop*.

[3]A quench is the loss of magnet superconductivity. If at some point a magnet coil turns into ohmic, the whole coil is artificially and immediatly heated, so that the stored energy spreads all over the magnet volume with reduced risk for the magnet integrity. The beam is also promptly aborted in a single turn.

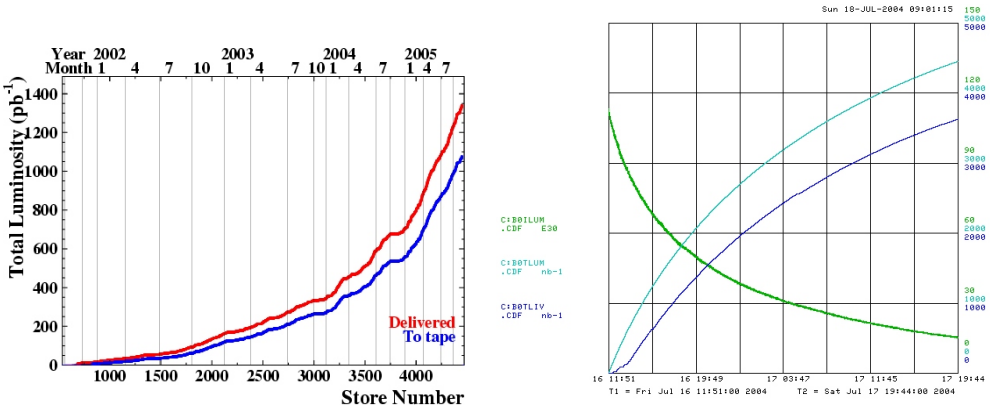

Figure 3.8: *Left: Delivered and CDF-acquired integrated luminosity as a function of the Store number. Right: the best store up to fall 2005. The decreasing line is the instantaneous $p\bar{p}$ luminosity, the increasing lines are the delivered (above) and the acquired integrated luminosity (below).*

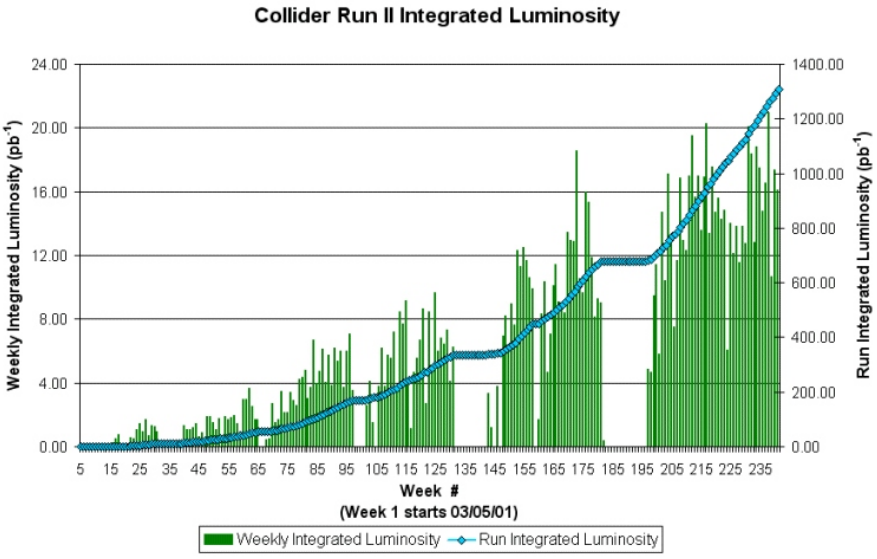

Figure 3.9: *The integrated luminosity in Run 2 weeks. The empty periods of time correspond to Tevatron shutdowns.*

3.2 The CDF Detector in Run 2

The CDF detector described here below is as configured for Run 2. A detector elevation view is presented in figures 3.11 and 3.12.

The CDF architecture is quite common for this type of detectors. Radially

Figure 3.10: *The Tevatron Control Room in a wide angle view.*

from the inside to the outside it features a tracking system contained in a superconducting solenoid, calorimeters (electromagnetic and hadronic) and muon detectors. The whole CDF detector weights about 6000 tons.

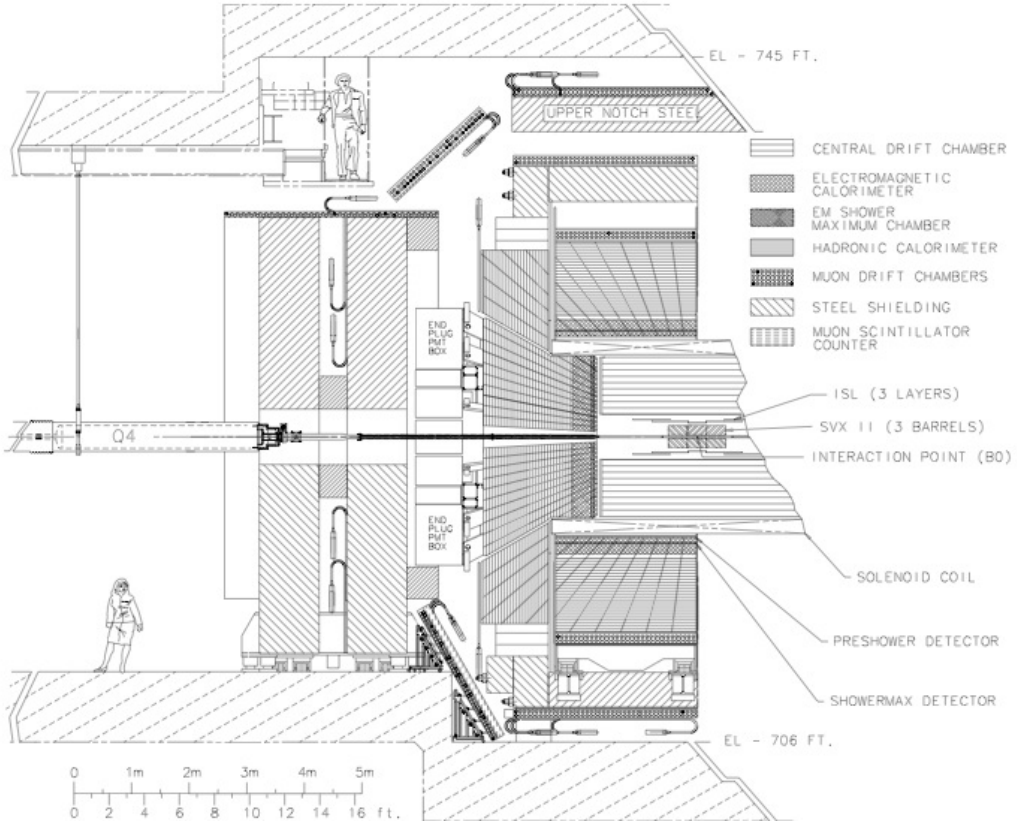

Figure 3.11: *Elevation view of the CDF II detector.*

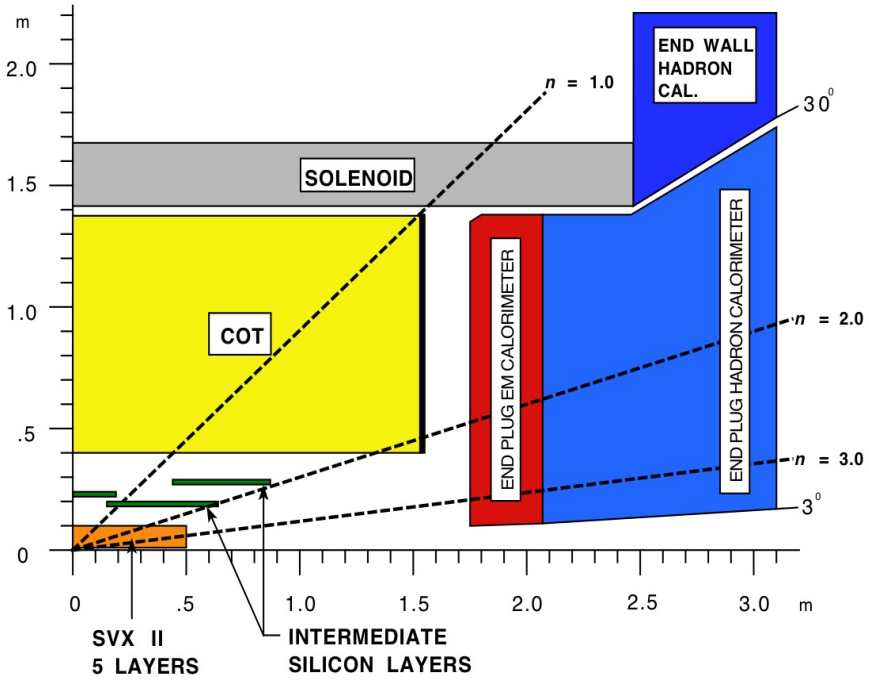

Figure 3.12: *The CDF II detector projected on the z/y plane.*

3.2.1 System Reference

The CDF detector is approximately cylindrically symmetric around the beam axis. Its geometry can be described in cartesian as well as in cylindrical coordinates.

The left-handed cartesian system is centered on the nominal interaction point with the $\hat{z}$ axis laying along the proton beam and the $\hat{x}$ axis on the Tevatron plane pointing radially outside.

The cylindrical coordinates are the azimuthal angle φ ($\varphi = 0$ on the $\hat{x}$ direction) and the polar angle ϑ ($\vartheta = 0$ along the positive $\hat{z}$ axis):

$$\varphi = \tan^{-1}\frac{y}{x} \qquad \vartheta = \tan^{-1}\frac{\sqrt{x^2+y^2}}{z} \tag{3.1}$$

A momentum-dependent particle coordinate named *rapidity* is also commonly used. The rapidity is defined as:

$$Y = \frac{1}{2}\ln\frac{E+p_z}{E-p_z} \tag{3.2}$$

Relative particle distances in rapidity are invariant under Lorentz boosts along the z axis.

A very useful approximation to rapidity which depends only on the polar angle is the *pseudorapidity* η, defined as:

$$\eta = -\ln\left(\tan\frac{\theta}{2}\right) \tag{3.3}$$

3.2.2 The Tracking System

The CDF tracking system is immersed in the 1.4 T magnetic field of a solenoid parallel to the beams. Particles are bent depending on their charge sign and transverse momentum.

There are two tracking systems at CDF, an inner Silicon tracker and a Central Outer Tracker (COT) drift chamber (figures 3.11 and 3.12).

Silicon Tracker

The silicon system (figure 3.13) employs stripped silicon wafers of an excellent space resolution of $\sim 12\ \mu m$. It was designed to sustain the large radiation dose to be integrated in a long running period. Simulations predict that the performances of the silicon tracker will remain unaffected up to $\sim 5\ pb^{-1}$ integrated luminosity.

The full CDF Silicon Detector is composed of three approximately cilindrical coaxial subsystems: radially towards the outside, the $L00$ (Layer 00), the SVX (Silicon VerteX), the ISL (Intermediate Silicon Layer). A total of 400k signals are provided from the silicon detector.

L00 is a 90 cm long, radiation hard, single sided, longitudinally stripped silicon detector which was added to the system in Run 2. It is mounted direcly on the beam pipe at $1.35 - 1.62\ cm$ from the beam axis. The detector support structure is in carbon fiber with integrated cooling system. The sensors are silicon wafers 250 μm thick with inprinted strips with 0.25 μm technology.

Being so close to the beal, L00 allows to reach a resolution of $\sim 25/30\ \mu m$ on the impact parameter of tracks of moderate p_T, providing a powerful help to signal long-lived hadrons containing a b quark.

L00 is backed by the **SVX**, a set of three cylindrical barrels 29 cm long each along z (see figure 3.14). Barrels are radially organized in five layers of double-sided silicon wafers extending from 2.5 cm to 10.7 cm. Three of those layers provide φ measurement on one side and 90^o z on the other, while the other two provide φ measurement in one side and a z measurement by small angle 1.2^o stereo on the other. The total SVX active length corresponds to nominal pseudorapidity coverage of $|\eta| < 2$. This is about 3σ of the gaussian longitudinal spread of the interaction points.

The alignement of the beamline along the axis of the SVX barrel is accurately monitored and corrected if needed. This is important in order to avoid φ-dependent spurious non-zero measurements of the impact parameter d_0 of traks

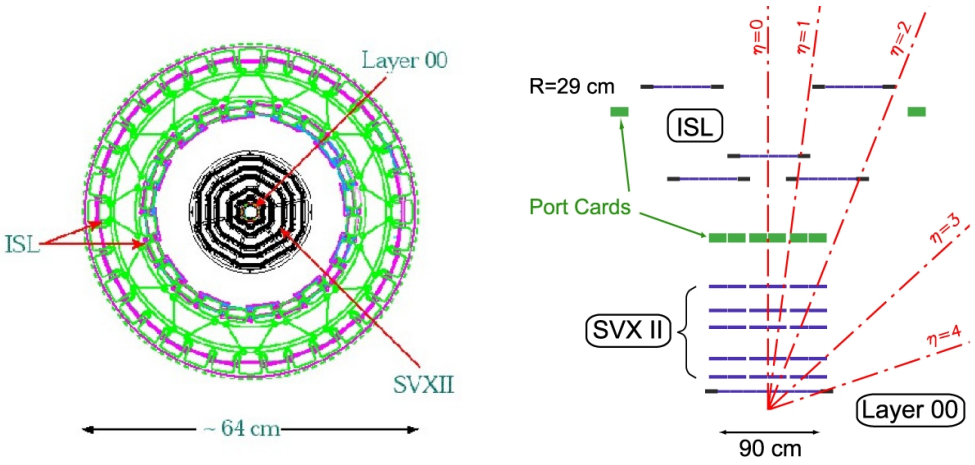

Figure 3.13: *Left: cutaway transverse to the beam of the three subsystems of the silicon vertex system. Right: sketch of the silicon detector in a z/y projection showing the η coverage of each layer.*

generated from the primary vertex. This is a very undesired effect since the track impact parameter is used to trigger on B hadron decays.

The **ISL** consists of 5 layers of double sided silicon wafers: four are assembled in two telescopes at 22 *cm* and 29 *cm* radial distance from the beamline covering $1 < |\eta| < 2$. One is central at $r = 22$ *cm*, covering $|\eta| < 1$. The two ISL layers at $1 < |\eta| < 2$ are important to help tracking in a region where the COT coverage is incomplete.

COT

The Central Outer Tracker (COT) is a 310 *cm* long open-cell drift chamber, positioned at $43 < r < 137$ *cm* radial distance just outside the ISL and covering the pseudorapidity range $|\eta| < 1$. The COT[4] is the most important detector for charged particle tracking in CDF.

It has 4 axial and 4 stereo[5] *superlayers*, alternating with each other and consisting of 12 wire layers each for a total of 96 layers and over 30k wires. The sense wires of each layer are alternated with field shaping wires. The chamber is filled with a fast gas mixture (Ar-Ethane-CF_4).

In the COT solenoid magnetic field the electrons drift at $\simeq 35^o$ (Lorentz angle) with respect to the direction of the cell electric field. The resolution in the transverse to radial direction is maximized by tilting the cell by the same

[4]The central tracking system in Run 1 (CTC) was changed to a tracker with shorter drift cells in order to cope with the six times shorted interbunch time of Run 2. This made the COT to employ a much higher number of sense wires, approximately 5 times more than the CTC. The gas mixture was also changed to a faster gas to help getting a shorter drift time.

[5]The stereo wires are tilted at $\pm 2^o$ with respect to the z direction.

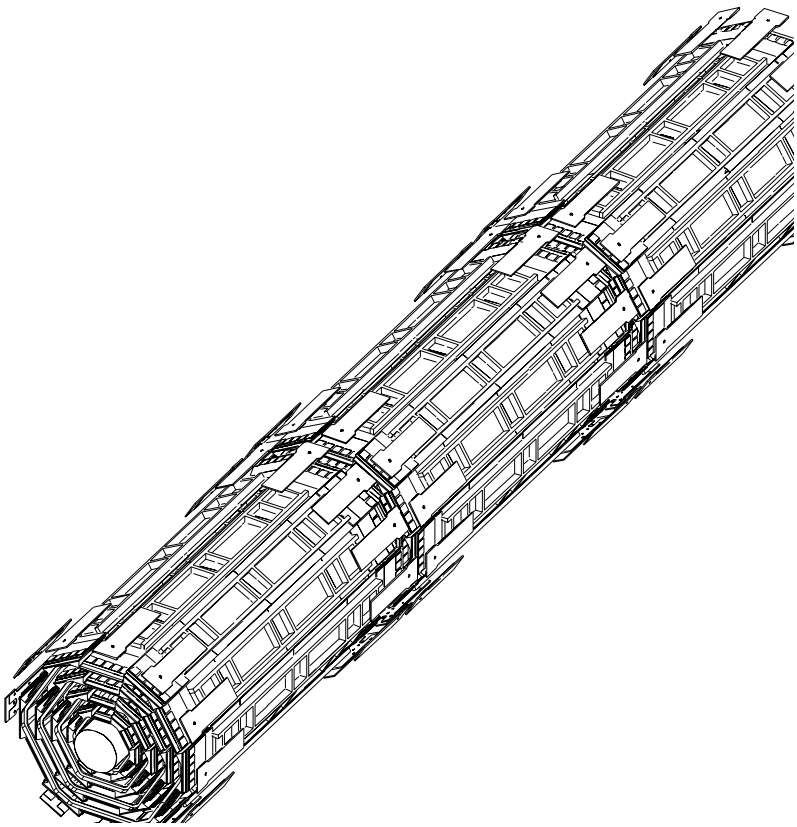

Figure 3.14: *The SVX silicon detector consists of three barrels with five layers of silicon detectors each.*

angle to make the drift path perpendicular to the radius. This geometry also makes hight p_T track crossing cells at different relative distances from sense wires thereby reducing the systematic errors due to drift field distorsions within a cell. The single hit position resolution has been measured to be $\sim 140\ \mu m$ which translates into an overall transverse momentum resolution of:

$$\frac{\partial p_T}{p_T} = 0.15\% \frac{p_t}{[GeV/c]} \tag{3.4}$$

3.2.3 Time of Flight

The Time of Flight (TOF) detector is a recent upgrade of the CDF detector. TOF is an array of approximately4 cm thick and wide, 279 cm long scintillator bars [6] parallel to the beam, which is laied as a cylindrical sheet of 216 elements on the inner solenoid wall, at a radial distance $r = 138\ cm$. Photomultiplier

[6]Bars have a slightly trapezoidal-cross section. They are so shaped in order to minimize particle losses through the cracks between bars.

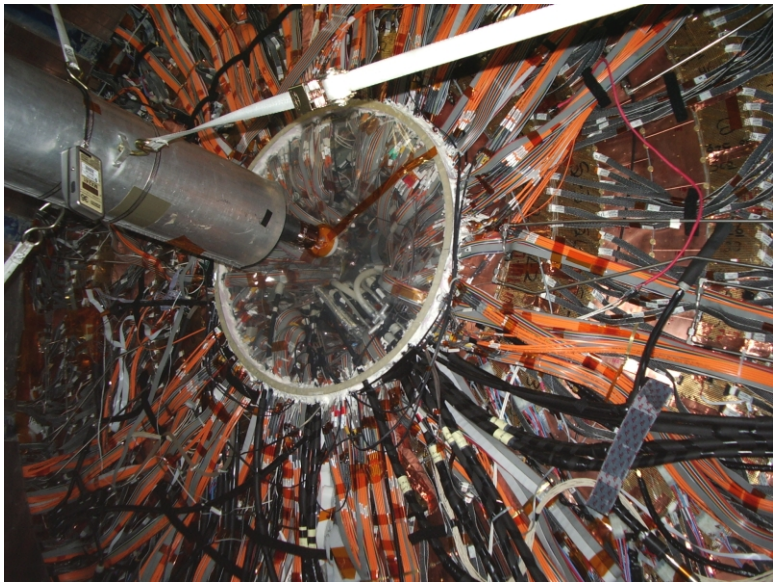

Figure 3.15: *The beampipe at SVX entrance. The messy radial structures are cooling pipes and cables carrying power and detector signals.*

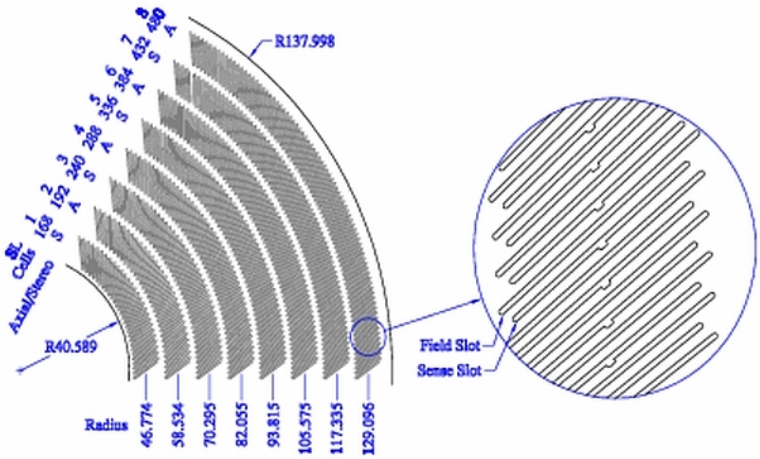

Figure 3.16: *One sixth of the COT endplate. The wires are grouped in 8 superlayers.*

tubes, that are capable to provide adequate gain even in presence of the magnetic field, are connected at both ends of the bars and provide time and pulse hight measurements. By comparing the two measurements, the z coordinate can also be determined.

A resolution of $\sim 110\ ps$ has been achieved which allows a 2σ separation of kaons from pions up to $\sim 1.6\ GeV$ at $|\eta| < 1$.

3.2.4 The Solenoid

The CDF detector is built around a solenoid providing a longitudinal magnetic field of 1.4 T. All the tracking system is inside this field. The solenoid volume is a cylinder 3.5 m long and 2.8 m in diameter (see figure 3.12).

The coil is an Al-stabilized NbTi superconductor operating at liquid helium temperature. The operation current is 4660 A. After carefull cool-down procedures during Run 1, the solenoid could be reused in Run 2.

The solenoid radial thickness correponds to 1.075 X_0 and initiates EM showers of crossing electrons and photons that are sampled by a pre-radiator detector (the CPR2 system, see section 3.2.5).

A picture of the wrapped solenoid being shipped from Japan to US in 1984 is shown in figure 3.17.

Figure 3.17: *The CDF coil was the largest superconducting solenoid ever built at that time. The picture shows the solenoid arriving to the Chicago airport from Japan in 1984. It was transported by a military airplane, which was the only one wide enough to be able to house it.*

3.2.5 CPR2: the Central Preshower system

The solenoid coil is 1.075 X_0 and as such initiates the particle showering to be sampled and integrated fully in the outer calorimeters. Radially behind the coil, in front of the calorimeters, a scintillator layer acts as a Central Pre-Radiation

detector (CPR) [6] for electrons and photons. A Central Crack Radiation detector (CCR) extends the preshower to the mechanically intrigued regions between calorimeter wedges. The 2 *cm* thick CPR scintillators provide a clear signature of the electromagnetic showers initiated in the solenoid coil. Information from the CPR is also useful to complement the calorimeter response for better jet energy resolution.

Figure 3.18 (left) shows one CPR2 module just before the top cover was installed. The figure shows the individually wrapped tiles and fibers exiting them.

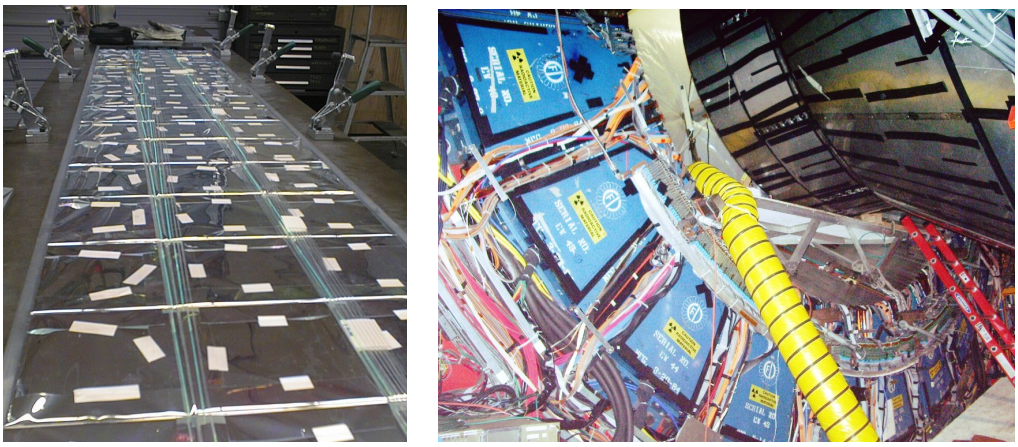

Figure 3.18: *Left: one CPR module during assembly in summer 2004. Tiles are wrapped in reflecting paper to avoid cross-talks and to maximize the light collection. The clear fibers are merged together into four groups at the end of the module and connected to R5900 photomultipliers. Right: the Plug calorimeter being removed away from the main detector body. A number of elements of the wall hadron calorimeter (in blue) are also visible.*

3.2.6 Calorimeters

The CDF calorimetric system is designed to absorb up to $\sim 98\%$ the hadronic and electromagnetic energy over most of the solid angle[7]. The calorimeters are split into cells projecting from the nominal interaction point in order to associate the single cell response to energy flow in a solid angle bin.

The CDF calorimeters are sandwiches of active and converter material covering two large η regions: the Central Calorimeter covers $|\eta| < 1.1$ and the Run 2 plug calorimeters cover $1.1 < |\eta| < 3.64$.

[7] A really 4π coverage is not possible. The beam pipe aperture cannot be covered and additional dead regions cannot be avoided at the edges of calorimeter wedges and cells.

Particles coming from the interaction point cross only relatively light detectors (the tracking system and the solenoid coil) before entering the calorimeters where they start showering. The scintillator light signals are collected separately from the front lead-scintillator electromagnetic and from the rear iron-scintillator hadronic compartments. Both signals are roughly proportional to the released energy in the shower. Accurate calibrations of response to particles of known energy and detailed MC simulations are necessary to reconstruct the incoming particle and jet energy.

Figure 3.19: *A CEM/CHA wedge during assembly. The absorber black iron frames are clearly visible as well as the light guides transporting the light from the scintillators to the photomultipliers (housed in tubes on the top of figure).*

Central

The Central Calorimeter has been preserved intact from Run 1 to Run 2. It consists of two coaxial barrels (east and west), each divided in two arches (left and right around the 90^o polar angle). Each arch is split into 12 azimuthal wedges of 15^o aperture. Finally, each wedge is split into 10 projective towers of width $\delta\eta \simeq 0.11$.

All calorimeters are radially split into an electromagnetic compartment, with lead as converter, and an hadronic compartment, with iron as converter. The light emitted in the plastic scintillator is collected in wavelenght shifting bars

(central calorimeter) or fibers (plug calorimeter) and transported to the PMT's.

The CEM electromagnetic compartment has 31 layers of 5.0 mm polystyrene scintillator alternate with 2.5 mm thick lead tiles. The Wall Hadron calorimeter (see figure 3.18, right) comprises 24 elements which are embedded in the front walls of the detector body. At variance with the central calorimeter these detectors are part of the magnetic field return joke.

The Central and Wall Hadronic Calorimeters (CHA, WHA) use iron as radiator. The CHA (WHA) has 32 (15) layers, and each layer is composed of 2.5 (5.1) cm of iron absorber and 1.0 (1.0) cm of plastic scintillator. The total calorimeter thickness is $\sim 4.7\lambda_0$ (λ_0 is the absorption length) for both CHA and WHA.

	CEM	**CHA**	**WHA**	**PEM**	**PHA**
η coverage	< 1.1	< 0.9	$0.7 < \|\eta\| < 1.3$	$1.3 < \|\eta\| < 3.6$	$1.3 < \|\eta\| < 3.6$
n. of modules	48	48	48	24	24
η towers/mod	10	8	6	12	10
n. of channels	956	768	676	960	864
Absorber (mm)	Pb (3.0)	Fe (25.4)	Fe (50.8)	Pb(4.6)	Fe (50.8)
Thickness	$19X_0, 1\Lambda_0$	$4.5\Lambda_0$	$4.5\Lambda_0$	$21X_0, 1\Lambda_0$	$7\Lambda_0$
Position res.	0.2×0.2	10×5	10×5		
Energy res.	$\frac{13.5\%}{\sqrt{E_T}} \oplus 1.7\%$	$\frac{75\%}{\sqrt{E_T}} \oplus 3\%$	$\frac{80\%}{\sqrt{E_T}}$	$\frac{16\%}{\sqrt{E_T}} \oplus 1\%$	$\frac{80\%}{\sqrt{E_T}} \oplus 5\%$

Table 3.2: *Geometry, parameters and performance resumée of the CDF Calorimetric System. The position resolution is given in $r \cdot \phi \times z$ cm^2 and is measured for a 50 GeV incident particle.*

Figure 3.19 shows one CEM/CHA wedge before installation. The iron tiles alternate with the scintillator tiles. The light guides to the photomultipliers are clearly visible.

CES

At the radial depth of ~ 5.9 X_0 in the CEM, i.e. close to the maximum in the longitudinal development of the electromagnetic showers, a proportional chamber named Shower Max Detector (CES, see figure 3.20), measures the local released ionisation projected in the two transverse directions.

The CES resolution is about 1 cm in z and about 1 mm in $r \cdot \phi$. During the Run 1 the CES information helped to reduce the fake electron trigger rate by a factor ~ 2. A similar measurement is performed in the forward electromagnetic calorimeter by means of planes of crossed scintillator bars.

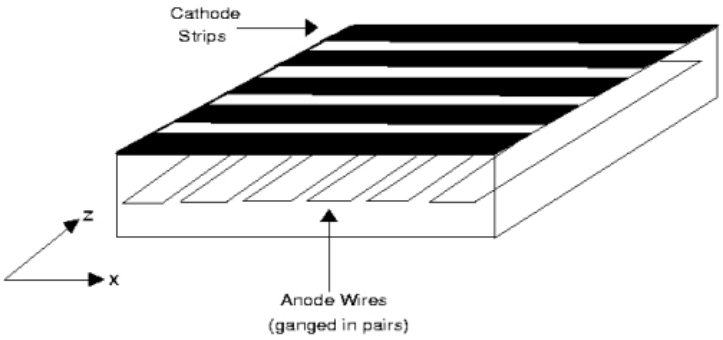

Figure 3.20: *The CES detector in CEM. The cathode strips run in the x direction and the anode wires run in the z direction providing x and $(r \cdot \varphi)$ measurements.*

Plug Calorimeters

The plug calorimeters of Run 2 employ the same technology as the central ones and extend the coverage to $\eta \simeq 3.6$.

Each Plug Calorimeter is divided in 12 concentric η regions (figure 3.21), which are further segmented in azimuthal wedges (48 φ wedges at $|\eta| < 2.11$, 7.5^o wide each, and 24 wedges at $|\eta| > 2.11$, 15^o wide each) with transverse dimensions depending on depth in order to build an array of projective towers.

As in the central calorimeter, there is a front EM compartment and a rear hadronic compartment (PEM and PHA). The first has 4.5 mm thick lead tiles alternating with 4.0 mm thick scintillators for a total of 23 layers equivalent to 21 X_0, the second has again 23 layers, but composed of 50.8 mm iron and 6 mm scintillator, for a total absorption length of ~ 7.0 Λ_0.

As in the central region, also PEM contains a shower maximum detector (PES) at ~ 6 X_0 depth. The PES consists of two layers of 200 scintillating bars each, oriented at crossed relative angles of 45^o ($\pm 22.5^o$ with respect to the radial direction). The position of a shower on the transverse plane is measured with a resolution of ~ 1 mm.

In the Plug region the first scintillator layer is thicker and is read out separately to work as a pre-radiator (PPR). The Plug assembly is very compact, so that plug cracks are negligible.

The most important calorimeter parameters are given in table 3.2.

3.2.7 Muon Detectors

After hadrons are (close to) fully absorbed in the calorimeters, muon detectors CMU, CMX, CMP, IMU (see figure 3.22) signal traversing muons. They

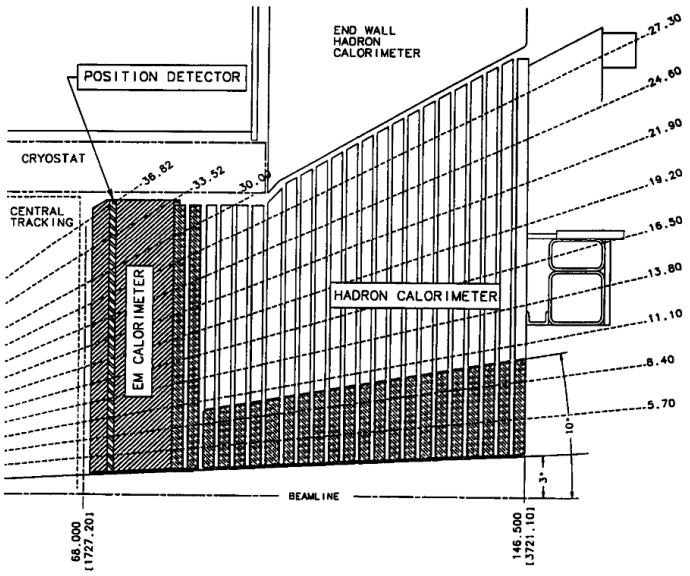

Figure 3.21: *Plug Calorimeter (PEM and PHA) inserted in the Hadron End Wall calorimeter WHA and into the solenoid.*

are important as trigger elements as well as in the off-line analysis of muon events.

Additional steel layers are added in front of the muon detectors in a number of areas. These additional hadron shields impose an increased energy to the travering muons. As a consequence, for each muon detector there is a specific lower detection threshold.

CMU

The Central Muon Chambers (CMU) [7] is a set of four layered drift chamber sandwiches housed on the back of wedges inside the central calorimeter shells covering the region $|\eta| < 0.6$. CMU is largely unchanged from Run 1, except for the fact that it operates now in proportional mode rather than in limited-streamer mode.

CMP

The Central Muon Upgrade (CMU) consists of a 4-layer sandwich of wire chamber operated in proportional mode covering most of the $|\eta| < 0.6$ region where it overlaps with CMU (see figure 3.22). Unlike mostly of the CDF components, this subdetector is not cylinrically-shaped but box-like, because CMP uses the magnet return yoke steel as an absorber, along with some additional

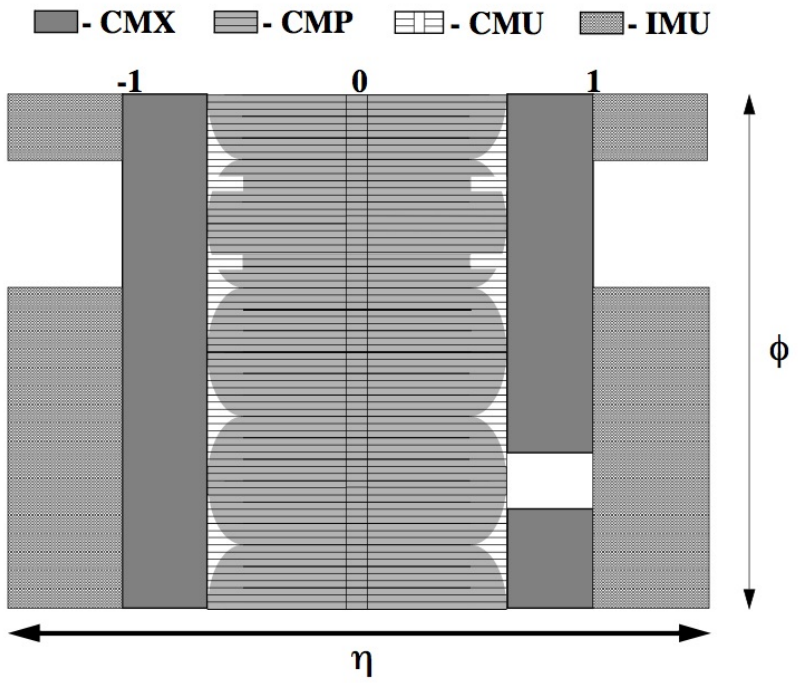

Figure 3.22: *The η/φ coverage of the muon detector system. The shape is irregular because of the obstruction by systems such as cryo pipes or structural elements.*

pieces of steel to fill gaps in the yoke. On the outer surface of CMP a scintillator layer, the Central Scintillator Upgrade (CSP), measures the muon traversal time.

The system CMU/CMP, which is called CMUP, detects muons having a minimum energy of $\sim 1.4\ GeV$.

CMX

The muon extension CMX is a large system of drift chambers-scintillator sandwiches arranged in two truncated conical arches detached from the main CDF detector to cover the region $0.6 < |\eta| < 1.0$. The low occupancy in this detector has allowed using wide gap drift cells whose signals can be read out over several bunch crosses.

IMU

Muons in a more forward region at $1.0 < |\eta| < 1.5$ are detected by the Intermediate Muon Extensions (IMU) on the back of the Plug Calorimeters. A telescope of two toroidal iron shields IMU from the hot hadron flux in this

angular region.

3.2.8 Cherenkov Luminosity Counter: CLC

In Run 2 CDF measures the collider luminosity with a coincidence between two arrays of Cherenkov counters, the CLC, placed around the beam pipes on the two detector sides. The counters measure the average number μ of interactions per bunch crossing. The luminosity is derived from the known average number of secondaries and inelastic cross section over the CLC angular coverage:

$$\mathcal{L}_{inst} = \frac{\mu f_{bunch}}{\sigma_{p\bar{p}}} \tag{3.5}$$

In this expression, $\sigma_{p\bar{p}}$ is the value of the inelastic $p\bar{p}$ cross section at 1.96 TeV and f_{bunch} is the rate of bunch crossing. This method measures the luminosity with about the 6% systematic uncertainty.

Each CLC module contains 48 gas Cherenkov counters of conical shape projecting to the nominal interaction point, organized in concentric layers. It works on the principle that light produced by any particle originated at the collision point is collected with a much higher efficiency than for background stray particles. The CLC signal is thus approximately proportional to the number of traversing particles produced in the collision.

3.2.9 Forward Detectors

The CDF Forward Detectors (whose scheme is shown in figure 3.23) include the Roman Pots detectors (RPS), beam shower counters (BSC) and two forward Mini Plug Calorimeters (MP). These detectors enhance the CDF sensitivity to production processes where the primary beam particles scatter inelastically in large impact parameter interactions (*pomeron exchange interactions*).

The Tevatron complex allowed to arrange a proper spectrometer making use of the Tevatron bending magnets only on the antiproton side. On this side, at appropriate locations, scintillating fiber hodoscopes inside three RPS measure the momentum of the inelastically scattered antiproton. Only the direction of the scattered proton is measured on the opposite side. The BSC counters at $5.5 < |\eta| < 7.5$ measure the rate of charged particles around the scattered primaries.

The MiniPlugs calorimeters at $3.5 < |\eta| < 5.1$ measure the very forward energy flow. MiniPlugs are a single compartment integrating calorimeter, consisting of alternate layers of lead and liquid scintillator read by longitudinal wavelenght shifting fibers (WLS) pointing to the interaction vertex. Althrough the miniplug is not physically split into projective towers, its response can be

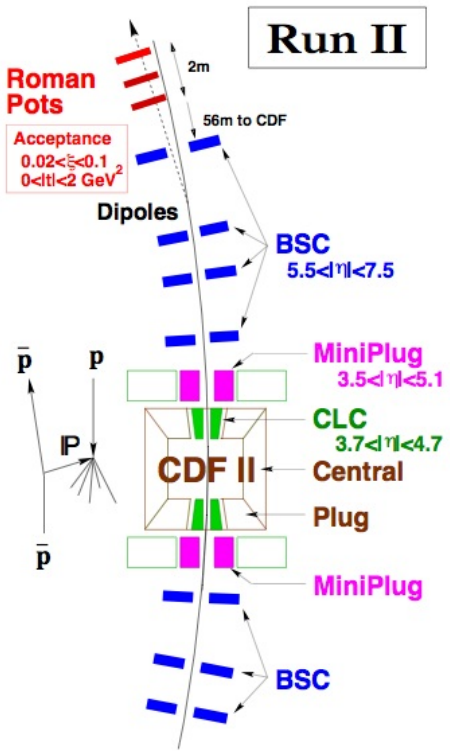

Figure 3.23: *The forward detectors system in CDF, as arranged for Run 2.*

split into solid angle bins in the off-line analysis. The MiniPlug energy resolution is about $\frac{\sigma}{E} = \frac{18\%}{\sqrt{E}}$ for single electrons.

3.2.10 Trigger System

The trigger system selects and stores interesting events for physics. Since the total inelastic cross section for $p\bar{p}$ is about $\sigma_{inel} \simeq 70\ mb$, and the collider luminosity can reach the $L = 10^{32} cm^{-2} s^{-1}$, the event rate can reach several 10^6 events per second, while storage can only register events at about 120 Hz. If an appropriate selection is made at trigger level, a major loss of physics information can be avoided because the rate of really interesting events is very low.

As an example, one may note that the top quark production cross section is about 6 pb, which is $\sim 10^{-10}$ of the total inelastic cross section. A top event is then expected every 10 billion interactions. The top event rate whould be one event in 10000 seconds at a luminosity of $10^{32} cm^{-2} s^{-1}$. If non-top events were efficiently rejected by the trigger the data logging power of CDF whould be much more than adequate to collect all Top quark production events.

Level 1 Trigger

The CDF Trigger system is organized in three levels.
The front-end electronics of all detectors is interfaced to a syncronous pipeline where up to 42 subsequent events can be stored for 5544 ns while the hardware is making a decisions. If by this time no decision is made, the event is lost. By doing so, since all the Level 1 decisions are made within about 4 μs, no dead time is caused by the trigger at Level 1.

The Level 1 rejection factor is about 150 and the typical output rate is about 50 kHz.

The Level 1 accepts are generated by:

- XFT (eXtremely fast Tracker), which reconstructs approximate tracks on the transverse plane of the COT. These tracks can be propagated to the calorimeter and to the muon chambers to contribute to electron or muon triggers at higher level;
- the calorimeter trigger, signaling large energy releases in the electromagnetic or hadronic cells as seeds of possible large energy electrons or hadron jets to be selected at higher level, and the total missing transverse energy;
- the Muon trigger, matching XFT tracks to stubs in the muon chambers.

Level 2 Trigger

Events accepted at Level 1 output are sent to 4 asyncronous buffers and further analyzed by a second set of hardware processors at Level 2. In Level 2 events are stored in the buffers until an individual decision is made. Because of the limited number of buffers some deadtime can be generated. In normal running conditions the Level 2 deadtime can be limited to less than 10%.

The main Level 2 trigger operations are:

- add the energy deposited in adiacent towers to the Level 1 seeds, as an approximate measure of an electron or jet energy;
- combine calorimeter and shower max detector (CES) information to improve the electron signature;
- reconstruct a full COT track and associate it to an outer muon stub to improve the muon signature;
- signal tracks with large impact parameter by means of the Silicon Vertex Tracker (SVT). This important function permits to trigger on secondary vertexes from decay of long-lived beauty hadrons.

The Level 2 accept rate is about 300 Hz and the rejection factor is about 150.

Level 3 Trigger

The Level 3 trigger is a software trigger, run on a Linux PC farm where all events are fully reconstructed using `C++` codes and object-oriented techniques.

Events coming from Level 2 are addressed to the Event Builder (EVB), which associates information on the same event from different detector parts. The events can thus be fully reconstructed in the Level 3 processors. The final decision to accept an event is made on the basis of its features of interest (large E_t leptons, large missing E_t, large energy jets and a combination of such) for a physics process under study, as defined by trigger tables containing up to about 150 entries. Events exit Level 3 at a rate up to about 100 Hz and are permanently stored on tapes for further off-line analisys. Each stored event is about 250 kB large on tape.

3.2.11 Online Monitoring

During data taking the quality of collected events is continously monitored. A fraction of about $\sim 1\%$ of the on-line reconstructed events are copied into a computer center adjacent to the Control Room of the experiment where a number of "consumer programs" generate significant plots (individual trigger rates, subdetector occupancy, readout errors, hot and dead detector channels, etc.) for the CDF shift crew to evaluate and intervene in case of problems.

3.2.12 Data Processing

Raw data stored on tapes are split into streams according to trigger sets tuned to a specific physics process and are stored on fast-access disks. Data are fully reconstructed again by the CDF off-line code (*production*) using the best detector calibrations and reconstruction codes available at the time. Occasionally, if more detailed calibrations or significantly improved codes become available, data are re-processed. Re-processing is an heavy computer time-consuming operation which is performed only when significant gain in reconstructed event quality is expected. For the analysis performed in the present work, the reconstruction code versions `5.3.3_nt5` and `6.1.4` were used.

Chapter 4

Top Mass Measurement in the Semileptonic Channel

This chapter deals with the technique used in this work to measure the Top quark mass, the Template Method. The technique is described in its application to the semileptonic decay channel of the $t\bar{t}$ system. A possible extension of this method, the 2-dimensional Template Method (with the so-called *in situ* calibration of the Jet Energy Scale), is described in Appendix A. One more method to measure the mass of the Top quark which does not reconstruct the Top mass event by event (but makes extensive use of the theory), the Matrix Element (ME) method, is described in Appendix B.

4.1 Top Quark Decay

As mentioned in section 1.2.2, the Top quark decay channels that can be exploited to measure the Top mass are essentially three, depending on the number of Ws decaying leptonically in the electron or muon channels:

Full hadronic: both the Ws decay hadronically. This channel features 6 jets, no missing transverse energy and no high-energy leptons in the final state. Despite the fact that this channel has the larger branching ratio of the $t\bar{t}$ systems (44%), its study is made difficult by the dominant QCD background. The trigger is based on the number of high energy jets, but due to the large background, the S/N ratio is $\sim 1/1000$. If applying the latest neural-network selection and requesting at least one b-tag (see section 4.4.3) in the event, the S/N ratio could raise up to 1/6 [8] [9].

Single Lepton: out of the two Ws, one decays leptonically (electon or muon plus neutrino) and one hadronically. The trigger comes from the missing transverse energy ($\not\!\!E_T$) and from the high-p_T lepton. This is considered the "golden

channel" for the Top quark mass study because of the good compromise between the background contamination and branching ratio (BR), which is $\sim$ 30%. The S/N ratio is of the order of 1/1 but can become as high as 20/1 if the b-tagging is used.

Di-lepton: both the W decay leptonicaly. The background is very low, but only a few signal events of this kind can be collected because of the small BR (4/81 if only considering electrons and muons). Moreover, because of the neutrinos in the final state, the $t\bar{t}$ events cannot be fully reconstructed as a function of the Top mass because the system is underconstrained. The sample can be exploited for a mass measurement for example by scanning the $\phi_1\phi_2$ plane (neutrino angles) and find the most likely mass. The S/N ratio is about 10, but can go up to 50 if the b-tagging is used.

(Tau): the Top events decaying in τ leptons are analyzed separately. The τ's decay into hadrons or leptons and are often confused by hadronic jets.

The relative branching ratios of the Top decay channels have been given in table 1.1. Figure 4.1 shows graphically the probability of the final configurations for the $t\bar{t}$ systems.

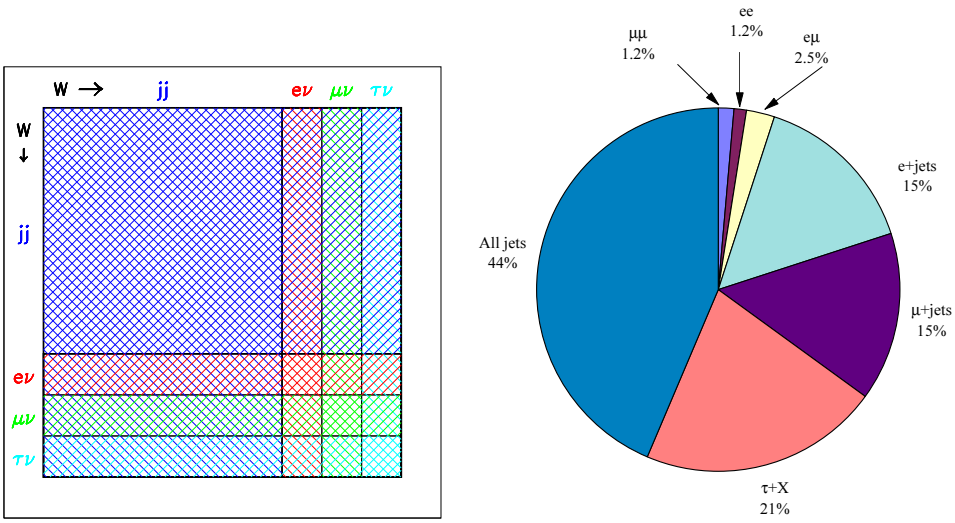

Figure 4.1: *The plot on the left shows how the W decay modes combine in a 2-W decaying system giving the realative BRs in the all-hadronic, single lepton, and dilepton states in proportion to the sectors of 2-dimensional squares. The right plot shows in a pictorial way the relative probability of the various channels. The plots are from [4].*

4.2 The L+J Top Decay

4.2.1 Signature

The neutrino from the leptonically-decayed W cannot be detected. Its four-momentum can be inferred in principle from the unbalanced energy by applying the energy-momentum conservation equations to the other remnants of the $t\bar{t}$ final state. However, because of the energy leak at small angles, the observed final state energy is less than the primary collision energy. Still the energy balance principle can be applied to the transverse energy of the system (E_T), which is zero in the initial state.

The L+J $t\bar{t}$ final state signature for events in the CDF central region consists of:

- an energetic electron detected by the CEM or an energetic muon detected by the CMUP, CMX, Miniskirt or Keystone muon chambers;
- at least four jets. When possible an additional signature is provided by jets tagged by the secondary vertex reconstruction algorithm SECVTX[1];
- a large transverse missing energy assumed to come mostly from the neutrino ν from the leptonically decaying W boson (see section 4.5.2).

In the semileptonic channel, the 4 jets have to be associated to the four original partons: two of them correspond to the hadronisation of the two b-quarks (one from the Top, one from the anti-Top) and are called *heavy flavour jets*[2], and the other two from the two lighter quarks (u, d or c, s) of the W hadronic decay.

4.2.2 Kinematics

The $t\bar{t}$ system decay has 5 vertexes (see figure 4.2). For each vertex we can write the conservation relations as in equation 4.1.

$$\begin{array}{rcccccl} \vec{0} & = & \vec{p}_T^{\,UE} & + & \vec{p}_T^{\,t} & + & \vec{p}_T^{\,\bar{t}} \quad (2\ eq.) \\ p_t^\mu & = & p_{W^+}^\mu & + & p_b^\mu & & (4\ eq.) \\ p_{\bar{t}}^\mu & = & p_{W^-}^\mu & + & p_{\bar{b}}^\mu & & (4\ eq.) \\ p_{W^\pm}^\mu & = & p_{l^\pm}^\mu & + & p_\nu^\mu & & (4\ eq.) \\ p_{W^\mp}^\mu & = & p_q^\mu & + & p_{\bar{q}}^\mu & & (4\ eq.) \end{array} \tag{4.1}$$

For the first vertex, where a gluon g gives a $t\bar{t}$ system, we can only write the transverse momenta (p_T) conservation because small angle particles are lost by the CDF detector around the beampipe. For this reason, the total energy conservation cannot be enforced and the first expression gives 2 scalar equations.

[1] See section 4.4.3.

[2] A jet from a c-quark is considered an heavy flavour jet as well.

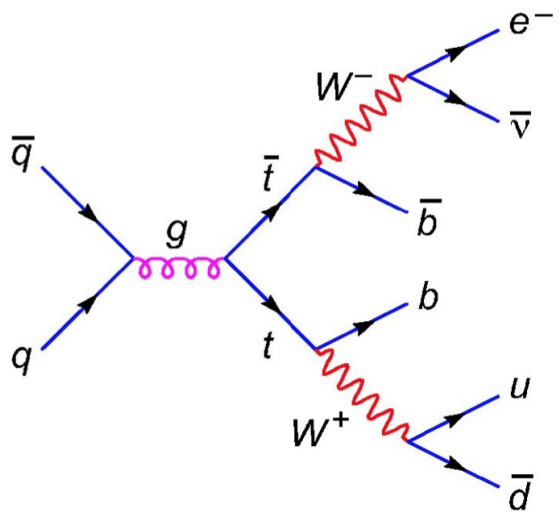

Figure 4.2: *The $t\bar{t}$ system decaying in the semileptonic channel: one Top branch has a W decaying leptonically, the other has a W decaying into light quarks.*

On the other hand, all the final products of the $t\bar{t}$ with the exception of the neutrino give signals from which we can reconstruct their full 4-momentum $p^\mu = (E/c, p_x, p_y, p_z)$. We get from each of the other expressions four scalar equations. The total number of equation we can write is 18.

The observables of which CDF can measure the 4-momenta are the lepton l (electron or muon) and the four jets coming from the hadronized $b, \bar{b}, q, \bar{q}$ partons. Of the underlying event UE which is a remnant of the $p\bar{p}$ collision besides the $t\bar{t}$ system, we can measure the two transverse momentum components.
The 4-momenta of the primary particles involved $(\nu, t, \bar{t}, W^+, W^-)$ are instead unknown, for a total of 20 unknown quantities. The contraints:

$$\begin{aligned} M_\nu &= 0 \\ M_t &= m_{\bar{t}} \\ M_{W^+} &= 80.4\ GeV/c^2 \\ M_{W^-} &= 80.4\ GeV/c^2 \end{aligned} \tag{4.2}$$

effectively reduces the number of unknown variables to 16. The kinematical system has 18 scalar equations and 16 variables. It can be solved as a function of the Top mass and of the square of the neutrino longitudinal momentum by minimizing a 2-constraint χ^2 expression (equation 4.8 and section 4.6.2).

4.3 Backgrounds

Many physics processes can give similar signatures to the one expected for a $t\bar{t}$ event. These processes are referred to as *backgrounds* (BG). When reconstructed as $t\bar{t}$ events, the overall Top mass distribution is the sum of $t\bar{t}$ events and of fake events. In order to compare the M_{top}^{reco} spectrum with a simulated one, the spectrum contributed by fake-$t\bar{t}$ events must be included. The relevant contributions to the background and the technique used to estimate it are discussed here.

We divide the BGs into two categories: the ***absolute backgrounds*** whose expected amounts N_i^{abs} are predicted by specific studies (the index i runs over the different contributions) and the ***W+mutijet backgrounds*** which is split into a number of separate channels of fractional amounts λ_i^{Wjet} relative to their total number N^{Wjet}.

4.3.1 Absolute Backgrounds

Non-W (QCD)

QCD interactions may generate 6 jets, one of which may simulate a lepton, one is lost (at least partially) in a crack or is wrongly reconstructed simulating a missing transverse energy $\not\!\!E_T$ and the other four give a signal similar to the two b-jets and the two jets from an hadronically decaying W boson of a $t\bar{t}$ event. In the background simulation, the spectrum of this background is obtained by extrapolation from data by relaxing the lepton isolation cut (see section 4.5).

Diboson

One W boson may decay leptonically and the second one hadronically. Two more jets can be found in the event, so as to reproduce the semileptonic $t\bar{t}$ signature.

Single Top

An s-channel electroweak $q\bar{q}'$ interaction may give a $t\bar{b}$ pair. After t-decay the event features three bodies $(Wb)\bar{b}$. The leptonic W decay provides the lepton and $\not\!\!E_T$ signals, while the b-quark pair gives two heavy flavour jets. If a couple of light jets are present in the event, the $t\bar{t}$ signature is met (figure 4.3, right).

Another single Top channel is expected at the Tevatron: a gq' hard interaction where the gluon splits into a $b\bar{b}$ pair. One of the b-quarks exchanges a W boson with one of the initial state quark (q') and gives a qt pair. The remaining b-quark is found in the final state qtb (the presence in the event of an additional jet may fake the signature for semileptonic $t\bar{t}$). Figure 4.3 at left shows the

interaction of the b quark from the gluon decay.

Even if Single Top is a real Top event, for the present study it is a background contamination since its topology is different from that searched for the $t\bar{t}$ system.

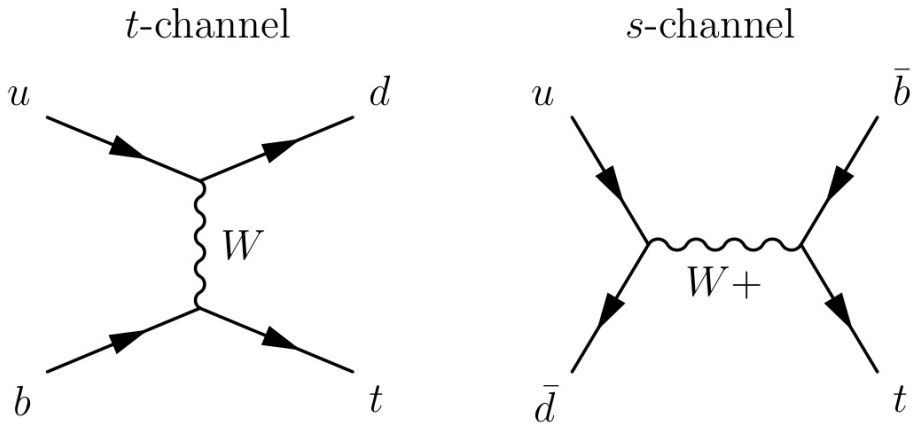

Figure 4.3: *The Single Top t-channel (left) and s-channel (right) largest order diagrams.*

4.3.2 W+multijet Background

W and associated Light Flavour jets

One W boson decays leptonically and four jets are found in the event. This is the largest background in the semileptonic $t\bar{t}$ decay. The Alpgen (kinematics) and the Herwig (showering) generators are used together to produce W+mutijets samples.

W and associated Heavy Flavour jets

One W boson decays leptonically. Two jets are produced by the hadronisation of b or c quarks, two more jets are present in the event. The different contributions to this process are $W + bb + 2p$, $W + cc + 2p$, $W + c + 3p$ (p stands for a light parton hadronizing).

4.3.3 Background Calculation

In the measurement of the Top quark mass the $t\bar{t}$ candidate events are usually divided into subsamples. Each subsample is exclusive and differs from the others for the number of tagged b-jets (see section 4.4.3). So-called *pretag* events are all events, regardless to the number of b-tags. 1tag events have a sigle b-tag and are

sometimes divided into two sub-cathegories: 1tagL and 1tagT (L and T stand for Loose an Tight) depending on the energy allowed for the least energetic of the four jets.

The 2-tag events have 2 b-tagged jets and the 0-tag events have explicitly no b-tags (see table 4.1). To limit the background, a higher energy is required for jets in this sample. The reason for dividing the candidates into subsamples is that they have different background contamination. A separate study of each sample allows a more precise mass measurement of the different spectra.

Sample	**b-tags**	**Jet 1-3** E_T (GeV)	**4***th* **jet** E_T (GeV)
pretag	any	≥ 15	≥ 15
0-tag	0	≥ 21	≥ 21
1-tagT	1	≥ 15	≥ 15
1-tagL	1	≥ 15	≥ 8
2-tag	2	≥ 15	≥ 15

Table 4.1: *Cuts defining pretag and exclusive subsamples by means of minimum jet energies and number of b-tagged jets. Note that pretags are not exactly the sum of the subsamples, due to the different jet energy cuts.*

For each subsample a BG estimation must be provided before the mass study in order to specify how many out the candidate $t\bar{t}$ events are expected to be signal. This estimation will weight the likelihood functions as described in section 4.6.

4.4 Jet Reconstruction

The raw information provided by each detector component cannot be used as it is for the physics analysis. It needs, indeed, to be processed and transformed into primary objects related to the physic process under study. In other words, the information at calorimeter level must be brought back to the parton level. This process runs backwards from the signal observed in the calorimeters and in the tracking system to the physic process who generated them (see figure 4.4).

This is especially needed for jets, which are identified as such after a suitable algorithm is applied to calorimeter signals. Clustering algorithms are applied during the online acquisition and are used for the trigger decision. Offline, when time is available for a more accurate reconstruction, the jet-objects are fully reconstructed and a number of corrections are applied in order to correct for known detector and physics effects degrading the original information. These corrections are applied to the MC and data events after parton fragmentation and detector simulation in order to reconstruct the momentum of the primary partons originating the jets.

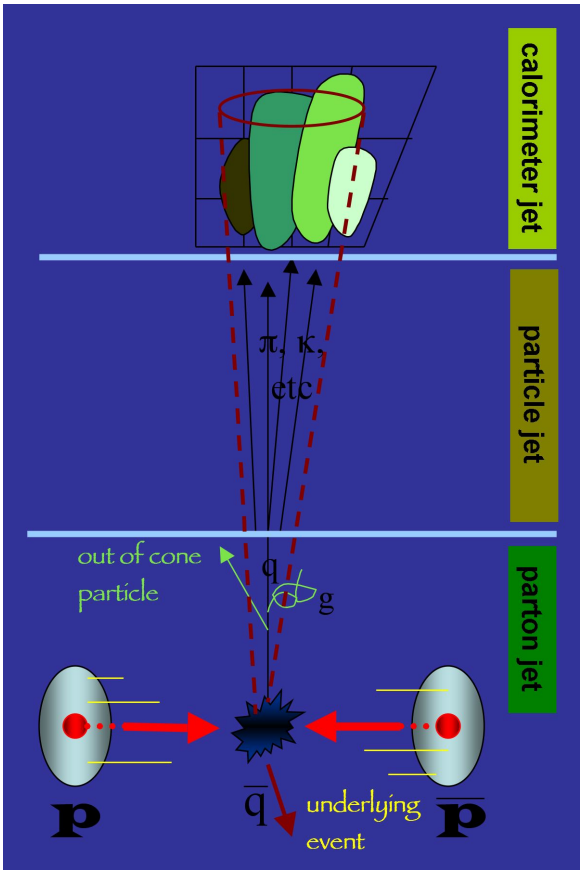

Figure 4.4: *The scheme shows the development of a jet from parton level to particle level and to detector level.*

4.4.1 Offline Clustering algorithms

CDF uses three jet algorithms to reconstruct jets: two cone-based algorithm *JETCLU*[3] and *MidPoint* and a coneless (KT) algorithm. JETCLU is the algorithm we employ here.

Preclustering

A *seed tower* is a tower having $E_T^{seed} \geq 1\,GeV$. JETCLU creates a list of seed towers and orders them by decreasing energy. Seed towers are associated with vectors having origin in the interaction point and terminating into the tower centroid. The vector module is proportional to the tower energy. Preclusters are created by combining adjacent seed towers within a preselected window in the $\eta - \varphi$ space plane. Starting from the highest E_t seed, the algorithm incorporates into the precluster the adjacent seed towers within the window

[3]The JETCLU was the only algorithm used in Run 1.

and removes them from the list. The process is iterated by adding the seeds adjacent to the previous ones until no new such seeds are found in the window (see figure 4.5).

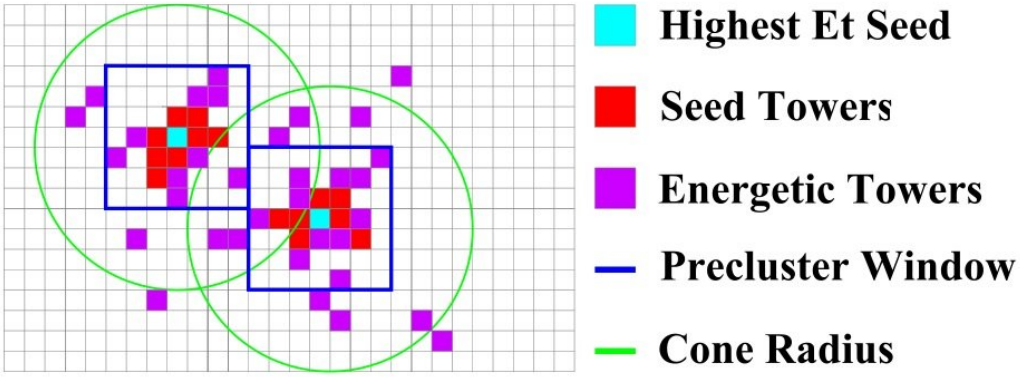

Figure 4.5: *Prelustering of two jets on the $\eta - \varphi$ plane. The green circles are the projections of the jet cone on the $\eta - \varphi$ plane.*

Clustering

The first step of the clustering process is to find for each precluster the centroid $(\eta_{centroid}, \varphi_{centroid})$ by weighting the towers by the transverse energy from booth the EM and the hadronic calorimeters. Then, a cone of radius $R = \sqrt{(\Delta\eta)^2 + (\Delta\varphi)^2}$ is created[4] around the centroid of the precluster and all towers inside this cone having $E_T > 100\ MeV$ ("energetic towers") are added to the cluster. Since this process could lead to a different tower collection, the centroid is recalculated and the clustering is repeated around the new centroid until the tower list (the sum vector) remains unchanged by a further iteration.

If there is a partial overlap between two clusters, the shared energy is calculated and compared with the energy of the smaller cluster. If the less energetic cone shares more than 75% of its energy with the other cone, the two cones are merged. Otherwise the shared energy is given to the closer cluster in the $\eta - \varphi$ space.

Once the cone have been identified, the algorithm assumes each vector to represent a massless particle which deposited all its energy in the centroid of the tower it's pointing to. The jet four-momentum is computed by summing the four-momenta of all vectors within the cone:

[4]The value of R depends on the physics analysis: for high p_T physics we use cones of $R = 0.4$ aperture, but other values as 0.7 or 1.0 are commonly employed.

$$\begin{aligned} E &= \sum_i (E_i^{had} + E_i^{EM}) \\ p_x &= \sum_i (E^{had} \sin\vartheta_i^{had} + E_i^{EM} \sin\vartheta_i^{em}) \cos\varphi_i \\ p_y &= \sum_i (E^{had} \sin\vartheta_i^{had} + E_i^{EM} \sin\vartheta_i^{em}) \sin\varphi_i \\ p_z &= \sum_i (E^{had} \cos\vartheta_i^{had} + E_i^{EM} \cos\vartheta_i^{em}) \end{aligned} \tag{4.3}$$

The jet (raw) transverse energy and momentum can be calculated as:

$$\begin{aligned} p_T &= \sqrt{p_x^2 + p_y^2} \\ E_T &= p_T \frac{E}{p} \end{aligned} \tag{4.4}$$

4.4.2 Jet Corrections

The calorimeter tower response to energy deposits is calibrated on test-beam or during the experiment using particles of known momentum.

However detector effects (for example, non linearities as e/h ratios, leackage, etc) or physics effects (for example out of cone energy, unclustered energy, etc) tend to degrade the parton four-momentum when passing to the calorimeter level. Consequently several corrections are needed.

The different corrections to jet energies are organized in levels and applied in sequence each one to the output of the previous one.

Level 0: these corrections are applied in the CEM to set the overall energy scale with electrons resulting from the Z^0 boson decay. The the same calibration is performed in CHA and WHA via J/ψ electrons about every 40 pb^{-1} of collected data. ^{60}Co radioactive sources and laser beams allow to transport the relative calibration to the entire calorimeter volume.

Level 1 are **relative corrections**. The η dependence of jet energy is corrected for. The differences are due to uninstrumented regions, different amount of material in the tracking volume and in the calorimeters, different responses by detector built with different technologies. The dijet balance technique is applied. Events with exactly two jets are selected, of which one is called *trigger* and is in the region $0.2 < |\eta| < 0.6$ where the response of the calorimeter is well understood, the other one is called *probe*. The correction consists in modifying the probe jet transverse energy in order to balance the transverse energy of the trigger. A plot of the uncorrected (left) response and of the corrected response by dijet balance (right) is reported in figure 4.6.

Levels 2 and **3** are not in use any more. Level 2 was used in Run 1 to correct for time depending variations in gain of the plug gas calorimeters. The level 3 was taking into account the differences between Run 1 and Run 2. These differences are presently accounted for by the new generations of the jet reconstruction software.

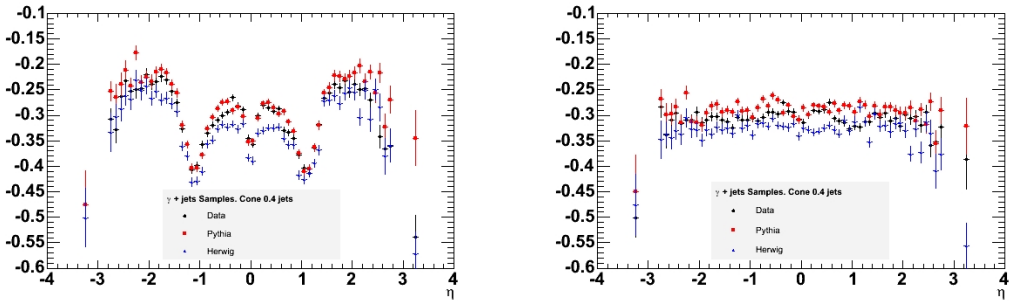

Figure 4.6: *Calorimeter response to jets: uncorrected (left) and corrected (right) by dijet balance. Events from the Phythia and Herwig generators are compared to data.*

Level 4 are **multiple $p\bar{p}$ interactions** corrections and are used to take into account the multiple $p\bar{p}$ interactions in the same bunch crossing: if more than one proton is interacting, the measured jet energy increases. The correction is derived from minimum bias data and it is parameterized as a function of the number of interaction vertices in the recorded event.

Level 5: absolute corrections. They correct the jet energy measured in the calorimeter for non-linear response of the CEM, for energy loss due to low-energy particles that couldn't reach the calorimeter or are lost in cracks. The correction is derived by comparing the same MC events at calorimeter level and at particle level as a function of p_T. Figure 4.7, left, shows this correction as a function of the jet transverse momentum.

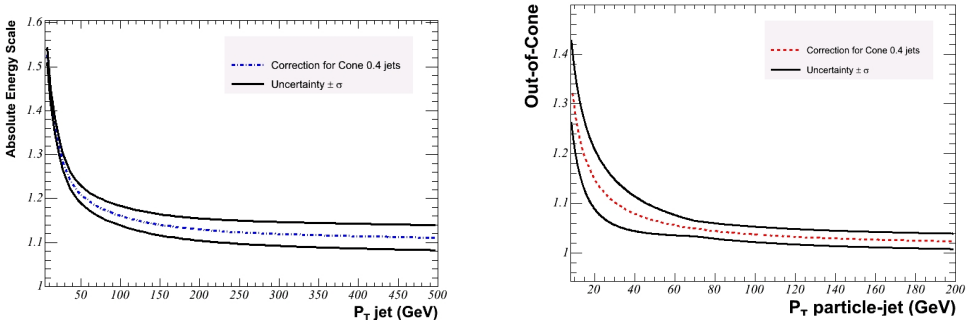

Figure 4.7: *Left: absolute jet energy correction. Right: Out of Cone jet energy correction. Both corrections are plotted as functions of jet transverse momentum. The bounds are the size of the systematic error (1σ).*

Level 6: underlying event corrections are intended to remove the energy contributed by the underlying event, which is due to spectator partons and

can contribute to a jet cluster.

Level 7 is the correction for the **out of cone** (OOC) energy. It adds to the jets the energy lost for leaked prongs outside the clustering cone (up to $R = 1.3$). Figure 4.7, right, shows the out of cone correction and its systematic error as a function of P_T.

Level 8: **splash out** corrects for the additional energy lost outside the $R = 1.3$ cone.

Figure 4.8 shows the entire set of systematic errors in measuring the jet energy. The (quadratic) sum of all contribution is shown as a black thick curve.

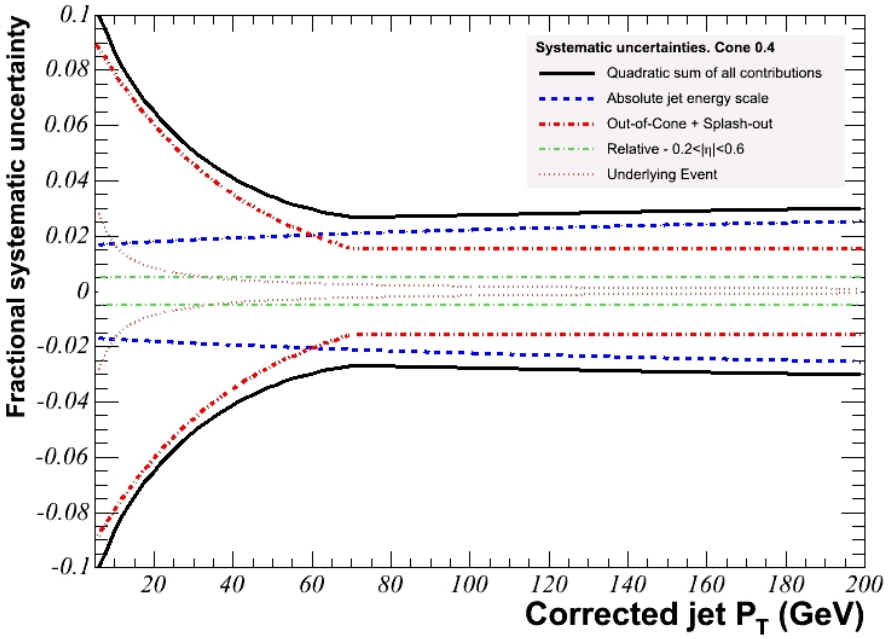

Figure 4.8: *Systematic error in the jet energy measurement as the quadratic sum of the different contributions as described in the text.*

4.4.3 b-tagging

A b-tagging algorithm, SECVTX, identifies secondary vertices from b quark decays. The first operation is to identify the primary vertex by fitting all tracks under a beamline constraint[5]. The primary vertex identification is performed

[5]The beamline is defined as a linear fit of a number of primary vertices for particular run periods. The luminous region described by the beamline has a transversal width of approximately 30 μm and a length (z direction) of ± 29 *cm fwhh*. In the primary vertex fit tracks missing the average by $> 3\sigma$ are rejected in an iterative process.

for each event using COT and silicon informations [10]. Then, the tracks with $E_T > 15\ GeV$ are checked for quality using COT and silicon information. If a secondary vertex (figure 4.9) can be reconstructed by using a minimum of two such "good" tracks, the distance between the primary and secondary vertices is computed, projected on the jet direction in the transverse plane. This distance is called L_{2D}. If $L_{2D} > 7.5 \cdot \sigma_{L_{2D}}$, then the jet is b-tagged. The SECVTX efficiency is about 60% for tagging at least 1 b-jet in a $t\bar{t}$ event. More information about b-tagging is available in [11].

Figure 4.10 shows two examples of b-tagged jets in L+J $t\bar{t}$ events.

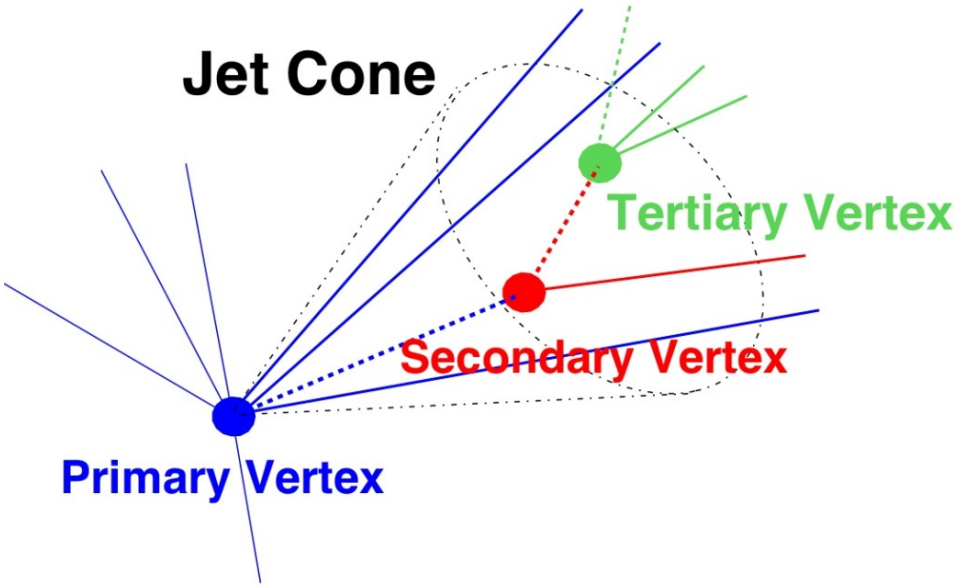

Figure 4.9: *A secondary vertex can be identified inside a jet cone (section 4.4.1) if an appropriate number of reconstructed tracks are not pointing to the primary vertex. The same procedure could in principle used to identify tertiary vertices.*

4.5 Event Selection

As for the jets (section 4.4), also lepton tracks and $\not\!\!E_T$ need to be derived from the relevant observables.

As is done in a less precise way at trigger level (section 3.2.10), the same strategy is applied off-line to decide whether the event should be accepted or not. In both cases the event selection is done in order to exclude as much as possible background contamination with minimum loss of signal yield.

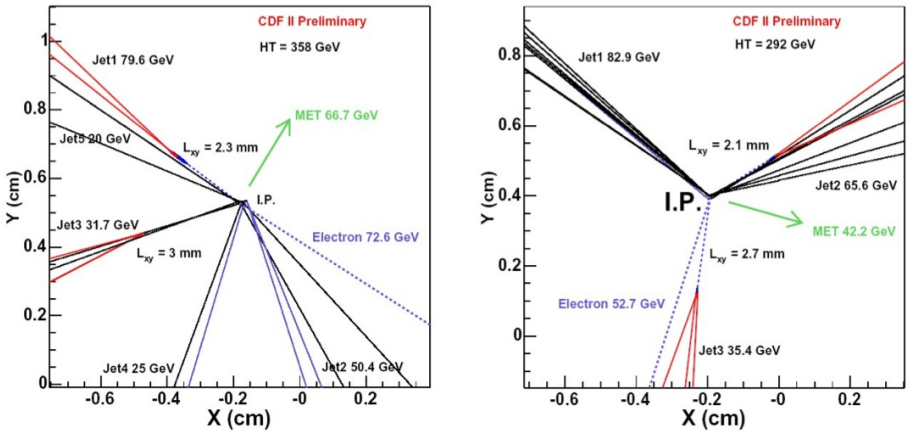

Figure 4.10: *Example of secondar vertices found by SECVTX algorithm. Left: run 167551, event 7969376. Right: run 155145, event 132579. IP is the interaction point (the primar vertex), MET is the* $\not\!\!E_T$ *and b-tagged jets are drawn in red.*

4.5.1 General Requirements

The following requirements must be met for an event to be accepted.

- An event must have at least four jets with $E_T > 15\ GeV$. In a particular sample (1TagL) the fourth jet is allowed to have $E_T > 8\ GeV$, and the sample is called "3.5 jet" event sample;
- an event is rejected when two leptonic tracks are consistent with coming from a Z^0 decay. An event is considered Z^0 production when two leptons of opposite charge and the same flavor are detected and their invariant mass is between 75 and 105 GeV;
- an event considered a QCD event according to a specific algorithm checking the $\not\!\!E_T$ direction relative to the leading jet is rejected;
- an event identified by specific algorithms as a $t\bar{t}$ event decaying in the dilepton channel is rejected;
- after an event is reconstructed, the $\chi^2 < 9$ request must be satisfied for the best jet-to-parton combination (section 4.6.1);
- the primary vertex must be within 60 cm from the $z = 0$ position.

4.5.2 Neutrinos

The presence of a neutrino from the leptonic W decay is signaled by the energy unbalance in the transverse plane. The missing transverse energy is

defined by projecting the energy contributions of all calorimeters into the transverse plane as described in equation 4.5, where $\mathbf{n_i}$ is the unit vector laying on the transverse plane and pointing to the ith tower from the event vertex.

$$\not\!\!E_T = -\Big|\Big| \sum_i E_T^i \mathbf{n_i} \Big|\Big| \tag{4.5}$$

The missing transverse energy is assumed to be due to the missing neutrino and is required to be $\not\!\!E_T > 20\ GeV$ after corrections depending on the muon momentum and on jet calorimeter response.

4.5.3 Electron Requirements

The following main criteria are required for an electron to belong to a $t\bar{t}$ candidate event:

- the electron is required to have $E_T > 20\ GeV$ and $|\eta| < 1$ (to be detected by the CEM);
- the *Isolation* is defined as $Isol = (E_{cone0.4} - E_{lepton})/E_{cone0.4}$ and measures how much calorimetric activity there is around the candidate lepton inside a $R = 0.4$ cone built around it. Isolation is required to be < 0.1;
- the ratio of calorimeter energy to track momentum E_T/p_T is required to be up to 2 for electrons having $p_T < 50\ GeV/c$ [12];
- the hadronic and electromagnetic energy deposited in the calorimeters should satisfy: $E_{had}/E_{em} < 0.055 + 0.00045 \cdot E_{em}$. This condition imposes a minimal leakage into the hadronic calorimeter as appropriate for electrons;
- if an e^+e^- pair is reconstructed as coming from a photon conversion, the event is rejected.

4.5.4 Muon Requirements

- The muon is required to have $p_T > 20\ GeV/c$ and $|\eta| < 1$ and its track should match with a stub (set of hits) in the muon chambers. Only muons from CMUP and CMX are used;
- the Isolation cut is imposed by requiring the total calorimetric energy around the muon track excluding the tower crossed by the muon to be less than 10% of the track transverse momentum;
- the muon must not be identified (by the specific algorithms) as a cosmic ray.

The trigger efficiencies are $\sim 96\%$ for electrons and $\sim 90\%$ for muons with negligible p_T dependence.

4.6 Template Method: Event Reconstruction

The event reconstruction code assumes that the observed 4 leading jets are originated by the four quarks in the $t\bar{t}$ system. However, a large part of $t\bar{t}$ events ($\sim$ 40%) [13] is expected to contain one or more jets due to gluon radiation within the four leading jets and thus to provide incorrect kinematical assignements. The gluon radiation may be produced by the incoming partons (Initial State Radiation, ISR) or by the final state quarks (Final State Radiation, FSR). Figure 4.11 shows the jets due to the ISR and FSR together with the jets from the $t\bar{t}$ system decay.

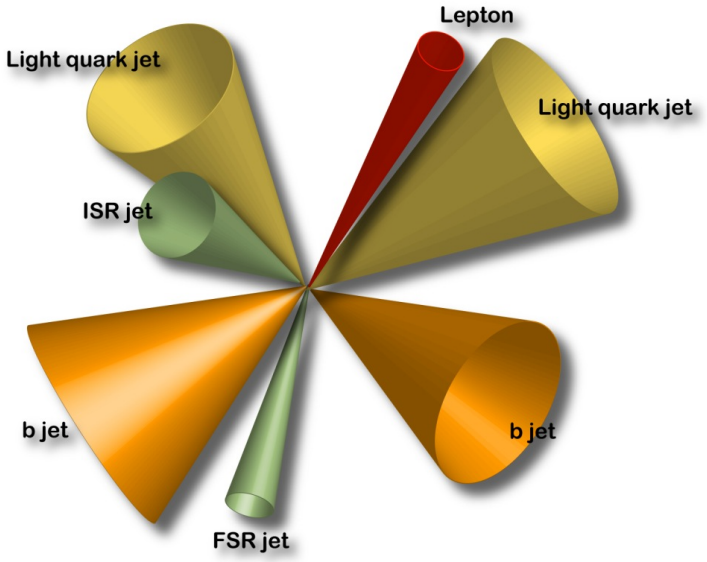

Figure 4.11: *Jets due to the $t\bar{t}$ system decay and to the ISR and FSR.*

As a consequence of the wrong assignments, the kinematically reconstructed Top mass M_{top}^{reco} should not be considered an event-by-event measurement of the mass, but rather a quantity which is strongly dependent on the Top quark mass. The real measurement will be inferred from the maximum likelihood fit as described in section 4.6.3, which consists in comparing the spectrum of the M_{top}^{reco}s with a function derived from MC simulations.

The M_{top}^{reco} value for each event is calculated with a χ^2 fit where the measured quantities and their errors are entered as input. In the L+J channel, each event can be reconstructed in 24 possible ways (see section 4.6.1 below).

4.6.1 Combinatorics

If the b-tagging algorithm is not applied, all 4 leading jets are considered interchangeable and there are 24 possible jet-to-parton assignments:

- four jets can be assigned infact to the 4 partons in $4! = 24$ different ways;
- the two jets fom the W decay can be exchanged without modify the kinematical reconstrucion;
- when solving the equation for the p_z^ν, that is a second-degree equation, we get in principle two distinguished solutions and we are not able to say which one is the correct one. For this reason each assignment provides two solutions for M_{top}^{reco}, one for each p_z^ν.

Therefore, when no tagging algorithm is applied, for each candidate event there are a total of $24 \cdot \frac{1}{2} \cdot 2 = 24$ possible reconstructed masses, called *combinations*.

If the SECVTX tagging algorithm (see section 4.4.3) is used, a fraction of the $t\bar{t}$ and BG events is tagged. If only one jet is b-tagged, the number of possible combinations is 12 because half of the combinations, those which assign the tagged b-jet to a W decay, are rejected. If two jets are b-tagged, the possible reconstructions are 4 because the only ambiguities are the interchange between the two b-quarks and the sign of p_z^ν. If three b-jets are tagged (this case is very rare), then the two leading ones are associated to the b quark.

4.6.2 Mass Reconstruction

When forming the electron and muon primary four-vectors, their masses are set to zero and all the angles are assumed to have no errors. Uncertainties as in equations 4.6 are assigned to the magnitudes of the electron and muon transverse momenta.

$$\begin{array}{rcl} \frac{\sigma_{p_T^e}}{p_T^e} & = & \sqrt{\left(\frac{0.135}{\sqrt{p_T^e[GeV/c]}}\right)^2 + (0.02)^2} \\ \frac{\sigma_{p_T^\mu}}{p_T^\mu} & = & 0.0011 \cdot p_T^\mu[GeV/c] \end{array} \tag{4.6}$$

All energy deposits that are not assigned to the 4 leading jets or to the lepton are considered unclustered energy (UE) and corrections for calorimeter response to hadrons are applied. After corrections for calorimeter calibrations, the uncertainty of $0.4 \cdot \sqrt{\sum E_T^{uncl}}$ is associated to the transverse components p_x^{UE}, p_y^{UE}, where E_T^{uncl} is the scalar sum of the transverse energies excluding the 4 jets and the lepton. The neutrino transverse momentum, that enters the χ^2 fit, is the quantity:

$$\vec{p}_T{}^{\,\nu} = -\left(\vec{p}_T{}^{\,l} + \sum \vec{p}_T{}^{\,jet} + \vec{p}_T{}^{\,UE}\right) \tag{4.7}$$

As mentioned before, the neutrino longitudinal momentum p_z^ν is a free parameter. The conservation equation determines its absolute value but not its

sign.

The reconstructed mass M_{top}^{reco} is obtained with a χ^2 fit given by equation 4.8. The fitter applies energy and momentum conservation and gives constraints to the decay subsystems. The χ^2 minimization allows the fit quantities to vary within the errors of the measured quantities. For each variation, the χ^2 value is calculated. The minimum allowed χ^2 returns M_{top}^{reco}.

$$\begin{aligned}\chi^2 &= \sum_{i=l,\ 4jets} \frac{(p_T^{i,fit} - p_T^{i,data})^2}{\sigma_i^2} + \sum_{j=x,y} \frac{(p_j^{UE,fit} - p_j^{UE,data})^2}{\sigma_j^2} \\ &+ \frac{(M_{jj} - M_W)^2}{\Gamma_W^2} + \frac{(M_{l\nu} - M_W)^2}{\Gamma_W^2} + \frac{(M_{bjj} - M_{top}^{reco})^2}{\Gamma_t^2} + \frac{(M_{bl\nu} - M_{top}^{reco})^2}{\Gamma_t^2}\end{aligned} \tag{4.8}$$

The first term accounts for the partons and the lepton transverse momenta to be fitted to the values of their observables. The second does the same with the unclustered energy transverse components. The two following terms account for the difference between the invariant masses M_{jj}, $M_{l\nu}$ (the two light-jets system and the lepton-neutrino system) and the W mass $M_W = 80.42\ GeV$. For M_W a gaussian distribution is assumed with width $\Gamma_W = 2.12\ GeV$ as in its natural Breight-Wigner shape.

The last two terms compare the fitted masses of the systems $bl\nu$ (b-jet, lepton and neutrino) and bjj (b-jet and two light jets) to the free parameter M_{top}^{reco}. For M_{top} a gaussian distribution is also assumed with width $\Gamma_t = 1.5\ GeV$ as predicted by theory for a Top quark mass $M_{top} = 175\ GeV$.

The above procedure yields an overconstrained system and there are several possible reconstructions per each event. A reconstructed Top mass is provided for each of the allowed jet-to-parton associations. Since for a semileptonic $t\bar{t}$ decay with no use of b-tag information there are 24 possible reconstructions (as seen in section 4.6.1), the M_{top}^{reco} is computed 24 times. The χ^2 is minimized once for each of the 24 possible combinations. Each minimisation associates a M_{top}^{reco} value to a χ^2 value, which is the quality factor for that reconstruction. The obtained combinations are ordered by increasing χ^2 and the first one (lowest χ^2) is entered into the mass spectrum.

4.6.3 The Final Fit

We define the Top quark mass as the parameter M_{top} giving the best agreement between the data mass spectrum and a number of mass spectra obtained with simulation techniques, called Montecarlo[6] (MC). The technique is called Template Method (TM) and consists in a likelihood fit. It works as follows:

[6]Montecarlo is a technique of data simulation. The name Montecarlo, which is an european town known for its casinos, recalls to casuality.

- A mass range of inspection is chosen. For example, if we want to measure a mass that we expect to be about 170 GeV, we set a mass range from 140 to 200 GeV in order to cover 3 or more expected sigmas around the expected mass value. A number of masses (20 for example) is chosen in the range. If necessary, tighter steps in the more sensitive zone could be added;

- for each of the chosen masses M_i we produce a large number[7] N of $t\bar{t}$ events at parton level using a MC technique. In the physics event generation, the same event is never repeted. Particle interactions with the detector are simulated, including a number of factors accounting for the inefficiencies of the subdetectors and for the non instrumented zones. Smearings due to experimental measurement uncertainties are applied as well. The MC events are then reconstructed as described in section 4.6.2 and an optimal M_{top} is found as the one corresponding to the best (lowest value) of χ^2 (equation 4.8). The obtained masses are collected into histograms which are normalized to unity, thus providing a probability density function (p.d.f.) for the mass M_i. This distribution is called *Mass Template* (see figure 4.12);

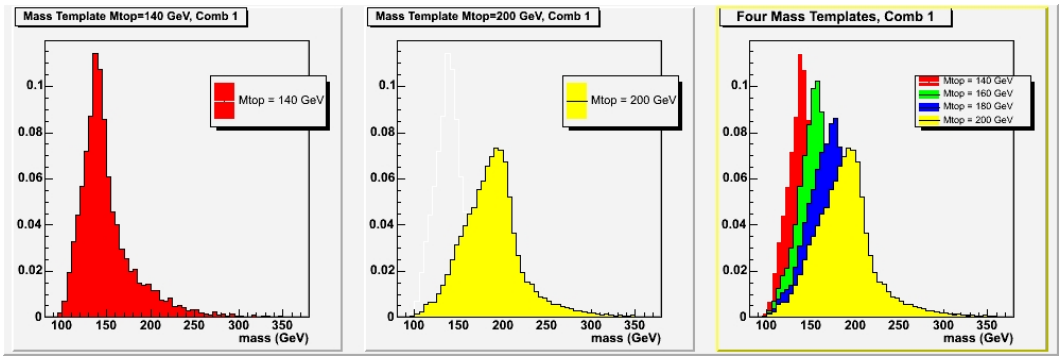

Figure 4.12: *The first two plots from the left show two mass templates (M_{top} = 140 GeV and M_{top} = 200 GeV) generated by Montecarlo. The right plot shows four superimposed masses.*

- MC samples are generated to simulate the background (BG) events. Every BG event passing the same selection criteria as data is an event simulating a $t\bar{t}$ signals and must be taken into account to generate the expected mass spectrum. There is a single BG template, in which the different BG contributions are combined according to their expected fractions;

- a program finds the parameters of a parametric function $f_{signal}(M_{top})$ fitting every mass templates (signal parameterization, see figure 4.13 on

[7]For example, 10^3 or 10^4 events.

the left). The adopted function is the sum of two gaussians (intended to account for the well measured events) and of the integrand of a Γ function (intended to account for events where the incorrect combination is chosen) [10] and enforces 18 parameters as in equation 4.9:

$$\begin{aligned} P^{signal}(M_{top}^{reco}; M_{top}) &= \alpha_7 \cdot \frac{\alpha_2^{1+\alpha_1}}{\Gamma(1+\alpha_1)} \cdot (M_{top}^{reco} - \alpha_0)^{\alpha_1} \cdot e^{-\alpha_2(M_{top}^{reco}-\alpha_0)} \\ &+ \alpha_8 \cdot \frac{1}{\alpha_4 \cdot \sqrt{2\pi}} \cdot e^{-\frac{1}{2}\left(\frac{M_{top}^{reco}-\alpha_3}{\alpha_4}\right)^2} \\ &+ (1 - \alpha_7 - \alpha_8) \cdot \frac{1}{\alpha_6\sqrt{2\pi}} \cdot e^{-\frac{1}{2}\left(\frac{M_{top}^{reco}-\alpha_5}{\alpha_6}\right)^2} \end{aligned} \tag{4.9}$$

with:

$$\alpha_i = p_i + p_{i+9} \cdot (M_{top} - 175) \tag{4.10}$$

To find the 18 p_i parameters the program performs an unbinned likelihood fit;

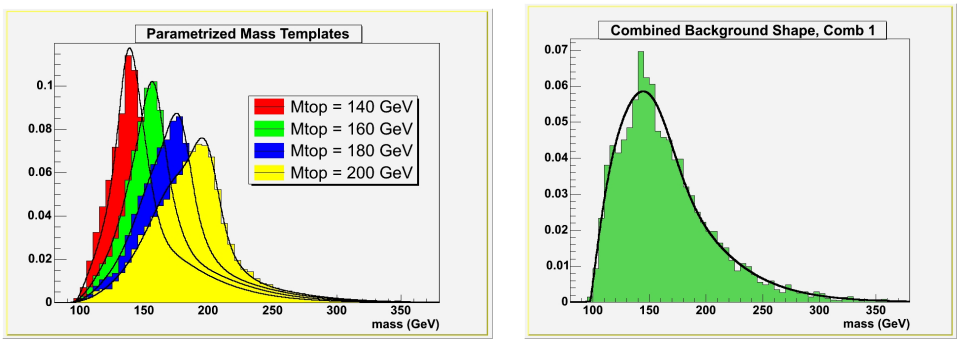

Figure 4.13: *Left plot shows four mass templates parameterized as described by equation 4.9. The right plot shows the BG combined sample with the parameterization described in equation 4.11.*

- a program determines a number of parameters for a parametric function f_{BG} to fit the BG histogram. There is no variation with M_{top} here, because background events do not depend on the Top mass[8] (background parameterization, see figure 4.13 on the right);

$$P^{BG}(M_{top}^{reco}) = \frac{p_2^{1+p_1}}{\Gamma(1+p_1)} \cdot (M_{top}^{reco} - p_0)^{p_1} \cdot e^{-p_2(M_{top}^{reco}-p_0)} \tag{4.11}$$

[8] If the BG from Single Top is taken into account, the function should theoretically depend on M_{top}. However, the single Top contamination in the $t\bar{t}$ sample is so small that this dependance is neglected.

- the two parametric functions $P^{sig}(M_{top}^{reco}; M_{top})$ and $P^{BG}(M_{top}^{reco})$ are combined in a likelihood function as in equation 4.13 where n_s and n_b are respectively the expected number of signal and background events.

  When the probability $p(D; n_s, n_b, M_{top})$ of observing our data set D given the values of n_s, n_b, M_{top} is expressed by summing on all possible values of the actual values of signal and BG events N_s and N_b (with $N_s + N_b = N$), the Poisson fluctuations

  $$P(N_s, n_s) = \frac{e^{-n_s} {n_s}^{N_s}}{N_s!} \qquad \text{and} \qquad P(N_b, n_b) = \frac{e^{-n_b} {n_b}^{N_b}}{N_b!} \tag{4.12}$$

  are introduced into the equation. The term $P(N, n_s + n_b)$ in equation 4.13 arises from the simplification of the resulting expression.

$$\mathscr{L}^{shape}(M_{top}) = \frac{e^{-(n_s+n_b)}(n_s+n_b)^N}{N!} \prod_{i=1}^{N} \frac{n_s \cdot P^{sig}(M_{top,i}^{reco}; M_{top}) + n_b \cdot P^{BG}(M_{top,i}^{reco})}{n_s + n_b} \tag{4.13}$$

$$\mathscr{L}^{constr} = e^{-\frac{1}{2}\left(\frac{n_b - n_b^{est}}{\sigma_{n_b}^{est}}\right)^2} \tag{4.14}$$

  Equation 4.14 constraints the number of BG events with a Gaussian distribution centered in the estimated number n_b^{est} which has the uncertainty $\sigma_{n_b}^{est}$. Unconstrained fit results like the one provide in table 5.12 are obtained by removing this term.

$$\mathscr{L} = \mathscr{L}^{shape} \times \mathscr{L}^{constr} \tag{4.15}$$

  The ith term of equation 4.15 gives the probability of observing the reconstructed mass $M_{top,i}^{reco}$ while the signal distribution is $P^{signal}(M_{top,i}^{reco}; M_{top})$, the the background distribution is $P^{BG}(M_{top,i}^{reco})$ and the BG is constrained;

- equation 4.15 is maximized with respect to n_s, n_b and M_{top} to provide their measurement. In particular, **the value of M_{top} for which $\mathscr{L}$ is maximum is defined as the measured Top pole mass**.

  The statistical error on the measurement on M_{top} is obtained by changing the value of the Top mass step by step away from its optimal value found by the fitter program, and letting the other parameters vary to meet the maximum likelihood values. By this process a $\mathscr{L}(M_{top})$ is found. Figure 4.14 is an example of $-\ln \mathscr{L}(M_{top})$ for $M_{top} \in [156; 214]$ GeV/c^2. The statistical uncertainty is defined when $-\ln \mathscr{L}(M_{top})$ changes by 0.5 units from its minimum.

This procedure for the error determination would be exact only for a gaussian likelihood function. However, a likelihood function will approach a Gaussian in the limit of large statistics and this is usually a good approximation even with limited statistics as long as the likelihood has a single maximum and its logarithm is roughly parabolic.

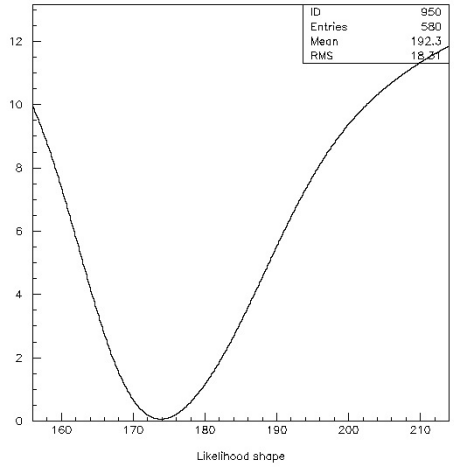

Figure 4.14: *Negative logarithm of the likelihood function depending on M_{top} only. The final likelihood fit provides a measurement of the Top mass which corresponds to the minimum of this function.*

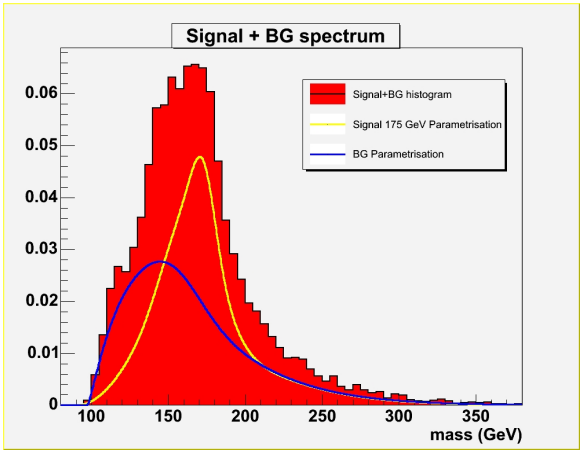

Figure 4.15: *This figure illustrates the fitting process. The overall mass spectrum is obtained by summing the signal spectrum from* $M_{top} = 175\ GeV$ *and a BG sample. The spectra were obtained selecting events with at least 4 jets. The two spectra were combined using as S/N a realistic ratio for a pretag sample. The continous lines are the parameterizations for the signal and for the BG contributions.*

Chapter 5

Multiple χ^2 Template Analysis of Run 2 Data

5.1 Framework

The CDF data acquisition system (DAQ) can include or not include in the event record the Silicon detector (section 3.2.2). In the first case the recorded events are listed in a *goodsilicon Good Run List (goodsi GRL)*, in the second case they enter the *no silicon Good Run List (nosi GRL)*. The nosi GRL is larger than the goodsi GRL because sometimes the Silicon Tracker is switched off to prevent damages if the beam is unstable, if the cooling system is overloaded or in other critical situations. This particular analysis does not make use of Silicon Vertex information (as b-tagging) because it runs on a pretag sample (see section 4.3.3). For this reason we don't need to require the events to belong the goodsi GRL, and we can increase the number of events in our sample by using the nosi GRL.

The detector data, and the Montecarlo simulated data as well, are organized sets of event files containing the relevant information for each event. The format of those files is the typical one used by `ROOT`[1], which is called *ntuple*. The ntuple contains a structured collection of informations easy to access by running the `ROOT` program. CDF uses its own ntuples, whose version is enhanced from time to time by using more sophistiated corrections to the physical processes or more recent calibrations or by storing some additional variables.

We require all the events (data and MC) considered for this analysis to:

[1] `ROOT` is an Object Oriented program for physics applications which includes a `C++` interpreter.

- belong to the pretag sample (nosi GRL);
- count 4 or more jets in the event having $p_t \geq 15\ GeV$;
- be reconstructed by the fit procedure as described in equation 4.8 returning a $\chi^2 < 9$.

The so-called datasets (files containing detector data) containing the first fb^{-1} of data collected by CDF are organized as in table 5.1.

Dataset	Lepton	Time period	Run range	pb^{-1} nosi/si GRL
`bhel0d`	e	up to 22 Aug 2004	138425 - 186598	362 / 333
`bhmu0d`	μ	up to 22 Aug 2004	138425 - 186598	362 / 333
`bhel0h`	e	4 Dec 2004 - 5 Sep 2005	190697 - 203799	399 / 363
`bhmu0h`	μ	4 Dec 2004 - 5 Sep 2005	190697 - 203799	399 / 363
`bhel0i`	e	5 Sep 2005 - 6 Feb 2006	203819 - 212133	269 / 258
`bhmu0i`	μ	5 Sep 2005 - 6 Feb 2006	203819 - 212133	269 / 258

Table 5.1: *Datasets organized by CDF according to lepton trigger, period of data-taking, run number, integrated luminosity.*

5.2 Blessing

A common procedure in the CDF Experiment, when a study Group wants to validate an analysis, is to ask for the *blessing*. The blessing is a procedure by which a study is described in detail to the Group of CDF scientists working on a similar subject and to the whole Collaboration. After the presentation, where a number of sanity checks (section 5.7) and the measures of the "blind samples" (5.7.3) made on simulated events are shown, the Group can allow the proponents to analyze the detector data. After all results are shown, the Group submits to the proponents some questions to test the study procedure. Once the proponents have answered the questions and convinced the entire CDF community, the Group *Conveners* convene a meeting where the analysis is "blessed" and the authors and any CDF collaborator are entitled to make the results of the analysis public.

The study reported in this thesis have been blessed at Fermilab December 14, 2006. The blessed plots, results and tables are indicated in their caption.

5.3 Reconstruction Rank

As mentioned above, the candidates are required to have one lepton over 20 GeV in p_T, $\not\!\!E_T > 20\ GeV$, and at least 4 jets with $E_t > 15\ GeV$. These four

leading jets are attributed to the four quarks in the decay of the $t\bar{t}$ pair. Once these events are reconstructed by the Fitter program, each of them provides 24 kinematical reconstructions. Each reconstruction is associated to a χ^2 value as in equation 4.8. The reconstructions are ordered by increasing χ^2 value and ranked from 1 to 24. As mentioned in section 4.6, the reconstruction corresponding to the lowest value of χ^2 (rank=1) was in the past usually chosen by the Template Method. We are exploiting the three lower ranks in this analysis.

Within MC simulations we can check how many times the association indicated by the best χ^2 is expected to be the correct one. First of all we find that only in about 54% of events the four leading jets are generated by the four decay quarks from the $t\bar{t}$ system.

Misleading assignements are generally due to the association of the decaying quarks to jets from gluon radiation (initial or final, see section 4.6).

Within these events, the jet-to-parton association corresponding to the lowest χ^2 has the best chance to be the correct one, but this happens only about 50% of the times. In the remaining cases the correct combination belongs to the other associations, with decresing probability with increasing χ^2 rank (see figure 5.1). The even bins in figure 5.1 are less populated than the odd ones because their entries are often rejected to avoid double counting, which can occur whenever the 2nd degree equation for the neutrino longitudinal momentum determines appoximatively the same Top mass value. We reject the second solution if the mass differs less than 100 MeV from the mass returned by the first solution.

Whenever the first combination is not the correct one, a not optimal mass value is entered into the spectrum, providing a *"combinatorial background"*.

The idea of the present study (see also [14], [15] and [16]), is to recover part of the mass information contained in the combinations beyond the first χ^2 one. One could consider making use of all of them, but the mathematical and computing effort whould be significant and probably not justified given the very low probability of the large χ^2 combinations of being the correct ones (see figure 5.1). As a reasonable compromise (see also section 5.7.4) we chose to include the 3 best combinations in the study.

5.4 Event Selection

As mentioned in section 5.1, we study here the data and MC events disregarding any b-tag information. To select the pretag events we mainly used the standard criteria proposed by the CDF Top Properties Group for Winter 06 analyses. The only differences are:

- we use the `GRL 13a` version with no silicon requirement for all datasets.

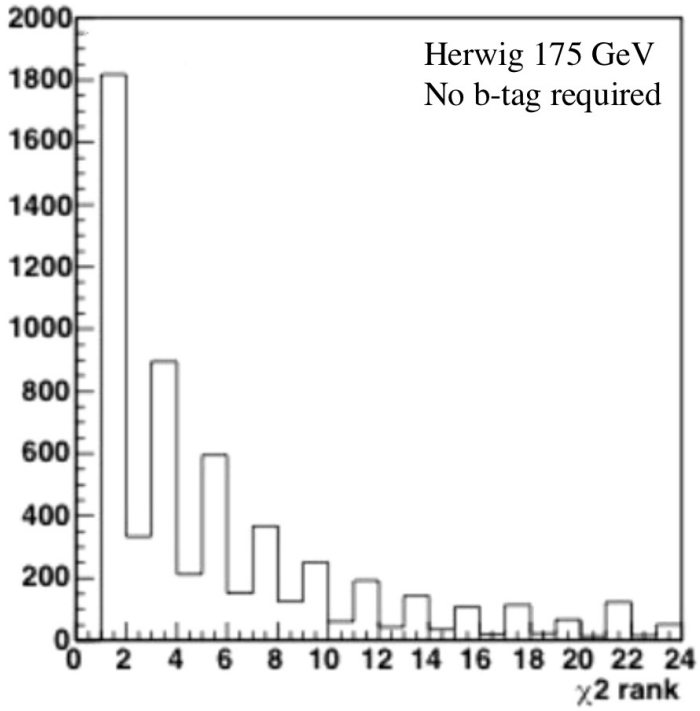

Figure 5.1: *The plot shows for the Herwig MC simulation with* $M_{top} = 175\ GeV$ *how many times the* χ^2 *ranks correspond to the correct jet-to-parton association. The plot deals with events where the four leading jets are associated with the four* $t\bar{t}$ *decay quarks. We note that the* χ^2 *rank =1 point corresponds to the correct association in less than* 50% *of times. The* $2n$*th bins are less populated than the* $(2n-1)$*th ones because their entries are often rejected to avoid double counting. As mentioned in the text, this happens when the two solutions for the neutrino longitudinal momentum determine appoximatively the same Top mass. We reject the second solution whenever its mass differs less than* 100 MeV *from the first one. Blessed plot.*

- we use the `JetCorrections` version `06b` for all datasets.

The number of selected events from our 1 fb^{-1} data sample in the goodsilicon and nosilicon cases are reported in table 5.2. Since these are data events, we don't know how many of them are BGs and how many are decaying $t\bar{t}$ systems. In the following paragraph we will estimate the amount of BG in the selected 645 events.

Selected Top Candidates CDF Run2 Preliminary, $1fb^{-1}$			
dataset	goodsilicon	nosilicon	nosilicon $\chi^2 < 9$
`bhel0d`	140	150	141
`bhmu0d`	75	91	84
`bhel0h`	151	170	155
`bhmu0h`	92	103	95
`bhel0i`	117	120	108
`bhmu0i`	61	62	62
Total	646	700	**645**

Table 5.2: *Number of selected events using the goodsilicon GRL (left column), the nosilicon GRL (central column) and nosilicon GRL after the* $\chi^2 < 9$ *cut.*

5.4.1 Expected Number of Signal and BG Events

To estimate the BG amount and composition we made use of a number of findings from an existing study which was performed by the CDF Top Properties Group for the Winter 2006 analyses [17]. That study was based on a tagged 695 pb^{-1} data sample (the pretag data corresponding to the same time period are 760 pb^{-1}). We start from an estimate of the BG amount and composition for that sample, and scale the results to our 1030 pb^{-1} nosilicon sample.

We first divide the BGs into two categories: the *absolute backgrounds* whose expected values $N^{tag}_{i,abs}$ are predicted by specific studies and published in [18], and the *W+jet backgrounds* in a number of exclusive channels which are estimated as fractions λ^{Wjet}_i of the total number of tagged W + multiple jet backgrounds N^{tag}_{Wjet} (section 4.3). $N^{tag}_{t\bar{t}}$ is the number of tagged Top events.

$$N^{tag} = N^{tag}_{t\bar{t}} + \sum_{i=2}^{8} N^{tag}_{i,abs} + \sum_{i=17}^{22} N^{tag}_{Wjet,i} \tag{5.1}$$

The i-index in the sum runs over the BG contributions reported in table 5.3. We introduce the Top fraction $f = N_{t\bar{t}}/N_{tot}$ and divide equation 5.1 by N_{tot} in order to obtain an expression in terms of the tag efficiencies:

$$\varepsilon_{tagevent} = f \cdot \varepsilon_{t\bar{t}} + \sum_{i=1}^{7} \varepsilon^{abs}_i \lambda^{abs}_i + \frac{N_{Wjet}}{N_{tot}} \sum_{i=1}^{6} \varepsilon^{Wjet}_i \lambda^{Wjet}_i \tag{5.2}$$

where ε^{abs}_i and ε^{Wjet}_i are the tagging efficiencies of the absolute and W+multijet contributions, $\lambda^{abs}_i = N_i/N_{tot}$ and λ^{Wjet}_i is the i-*th* fraction of the overall tagged W+jets sample.

We built then a likelihood function (equation 5.3) describing the probability to get $f \cdot N_{tot}$ $t\bar{t}$ signals and we used the algorithm MINUIT to maximize

it, assuming a binomially distributed (B) tagged candidates and Gaussian distributed (G) signals and backgrounds:

$$\mathscr{L} = B(N_{tag}, N, \varepsilon_{tagevent}, (1-\varepsilon_{tagevent})) \times \prod_i G_i(n_i, \sigma_i) \tag{5.3}$$

The likelihood equation is minimized with respect to f, allowing the γ_i parameters to vary within 1σ.

$$\begin{aligned} -\ln\mathscr{L} &= -\ln(\varepsilon_{tagevent}^{N_{tag}}(1-\varepsilon_{tagevent})^{N-N_{tag}}) + \tfrac{1}{2}\left(\tfrac{\gamma_1-\varepsilon_{t\bar{t}}}{\sigma_{\varepsilon_{t\bar{t}}}}\right)^2 \\ &+ \textstyle\sum_{i=2}^{8} \tfrac{1}{2}\left(\tfrac{\gamma_i - N_{abs,i}^{tag}}{\sigma_{N_{abs,i}^{tag}}}\right)^2 + \sum_{i=9}^{16} \tfrac{1}{2}\left(\tfrac{\gamma_i-\varepsilon_i^{abs}}{\sigma_{\varepsilon_i^{abs}}}\right)^2 \\ &+ \textstyle\sum_{i=17}^{22} \tfrac{1}{2}\left(\tfrac{\gamma_i - N_{Wjet,i}^{tag}}{\sigma_{N_{Wjet,i}^{tag}}}\right)^2 + \sum_{i=23}^{29} \tfrac{1}{2}\left(\tfrac{\gamma_i-\varepsilon_i^{Wjet}}{\sigma_{\varepsilon_i^{Wjet}}}\right)^2 \end{aligned} \tag{5.4}$$

The background processes appearing in equation 5.4 are given in table 5.3. Indexes from 9 to 16 refer to the tagging efficiencies of processes with the tag rates $N_{abs,i}^{tag}$ with $i = 2...8$. Indexes from 23 to 29 refer to efficiencies of processes having tag fraction λ_i^{Wjet} with $i = 17$ to 22.

The fractions of the W+jets backgrounds, the expected number of absolute background events and all the tagging efficiencies central values and relative uncertainties are taken from [18].

BG cathegory	BG process	BG sample	i
Absolute	Non-W (QCD)	BG3	2
	WW	BG4	3
	WZ	BG4	4
	ZZ	BG4	5
	$Z \to \tau\tau$	BG4	6
	single top t	BG5	7
	single top s	BG5	8
W+multijet	Wbb, 1B matched	BG2	17
	Wbb, 2B matched	BG2	18
	Wcc, 1C matched	BG2	19
	Wcc, 2C matched	BG2	20
	Wc	BG2	21
	W+ light jets	BG1	22

Table 5.3: *BG processes whose contribution is taken into account by maximizing the likelihood giving the $t\bar{t}$ fraction as described in the text. The W+HF jets BSs are indicated together with the number of matched jets from b or c quarks [19].*

The procedure described above is encoded in a program which performs the likelihood maximization using the constants γ_i reported in the above mentioned study. For the 695 pb^{-1} goodsilicon case (468 candidates) the program returns 219 ± 26 BG events. The more likely BG composition, before any χ^2 cut, is 172 W+jet (141 W+mistag and 31 W+HF), 30 non-W (QCD) and 17 diboson (WW/WZ). The contribution from Single Top processes is expected to be less than one event and is therefore neglected. The pre-χ^2 cut composition is then $f_{BG_1} = 64.4\%$ W+mistags, $f_{BG_2} = 14.1\%$ W+HF, $f_{BG_3} = 13.7\%$ non-W, $f_{BG_4} = 7.8\%$ diboson. We make use of these fractions to derive the BG rate in our larger event sample.

In 760 pb^{-1} nosi runs we observe 482 candidates. We scale the goodsilicon estimated BG to this luminosity and obtain $219 \cdot 760/695 = 239$ BG events in 760 pb^{-1}. The luminosity is used as scale factor because the two data sets were acquired together during the same data-taking period.

Our final data sample includes 1030 pb^{-1}. The observed $t\bar{t}$ events in the 1030 pb^{-1} noslicon GRL are 700 (see table 5.2). In order to allow for fluctuations of event rate we normalize the expected BG to the 700 candidates actually observed. This gives an estimated background of 347 events. To propagate the BG estimation throught the events passing the χ^2 cut, we calculate individually the χ^2 cut efficiencies (see table 5.4) for each BG and combine them to obtain an overall BG cut efficiency.

$$\varepsilon_{\chi^2_{cut}}(BG_{tot}) = \sum_{i=1}^{4} \varepsilon_{\chi^2_{cut}}(BG_i) \cdot f_{BG_i} = 0.882 \tag{5.5}$$

Name	Process	pre-χ^2 cut ratio	χ^2 cut eff	post-χ^2 cut ratio
BG1	$W + L.F.$	64.4 %	0.865	63.3%
BG2	$W + H.F.$	14.1 %	0.873	13.9%
BG3	QCD	13.7 %	0.941	14.6%
BG4	WW/WZ	7.8 %	0.931	8.2%

Table 5.4: *Composition of our combined BG sample. $W \rightarrow L.F.$ is the process having index 22 in table 5.3, $W \rightarrow H.F.$ corresponds to indexes from 17 to 21. The ratios in the last column are normalized to 100%.*

We apply then the computed $\varepsilon_{\chi^2_{cut}}(BG)$ of the χ^2 cut. 306 events out of 347 pass the cut. Noticeably, the signal-to-noise ratio turns out to be (645-306)/306=1.11, which is the same as obtained in the 760 pb^{-1} sample after $\chi^2 < 9$ cut.

We conclude that in our sample of 645 events (fourth column in table 5.2), 306 are expected to be BG and 339 to be $t\bar{t}$ signals. In the pseudo-experiments (PE) these numbers are fluctuated as explained below.

We obtain the non-W (QCD) BG shape from the data events when they fail the lepton isolation cut. For an event to enter the QCD BG sample we require an electron or muon with isolation > 0.2 and $\not\!\!E_T > 20\ GeV$.

5.4.2 Pseudoexperiments

In order to perform a number of sanity checks, study the systematic uncertainties, determine the weight factors needed to add the information from the 3 best χ^2 combinations and analyze the blind samples we performed a large number of pseudo-experiments (PEs). A pseudo-experiment is a collection of MC events where the ratio between the number of signal and BG event is the same as the expected in the data and the total number of events is exactly the same as the selected data. Since there is an uncertainty on the BG amount, this number is allowed to fluctuate from a PE to another following a gaussian probability distribution having the same width as the estimated uncertainty. The PEs allow to obtain a large number of events which are similar to the unique data sample in order to permit statistical studies. Since in one PE set the signal is extracted from a single MC run where a specific M_{top} is assumed, it is mandatory to produce many PE's by varying the input Top mass.

Therefore, we build each PE by extracting at random a number of events from the BG sample (with the ratios indicated in table 5.4, last column). The total number of BG events in each PE is fluctuated around the central value of 306 with a Gaussian distribution. The width of the distribution was estimated by the uncertainty in the BG contamination propagated through the scaling process and increased by 10% to account for possible additional fluctuations due to beam-beam overlapping events in the recent high luminosity runs[2]. This calculation gives:

$$\sigma(N_{BG}) = 26.4 \cdot \frac{760}{695} \cdot \frac{700}{482} \cdot 0.882 \cdot (1 + \sqrt{\frac{1}{700} + \frac{1}{482}} + 0.1) = 42.9 \qquad (5.6)$$

We assumed $\sigma(N_{BG}) = 44$ in our PEs.

5.4.3 Data/MC Comparison

After the selection of the events we can compare data and simulations by displaying some interesting kinematical quantities. Figure 5.2 shows the transverse energy distribution of the five leading jets in the selected data and in MC events. For the same events, figure 5.3 reports the distributions of the lepton transverse

[2]The results of the PEs turned out to be insensitive to fluctuations in BG rates.

momentum, of $\not\!\!E_T$ and of the number of jets. The Kolmogorov-Smirnov tests (table 5.5) indicate in general a good agreement since the p-values are, as expected, flatly distributed between 0 and 1.

	Compare	KS p-value.
lepton p_T	0d vs MC	0.13
lepton p_T	0h vs MC	0.02
lepton p_T	0i vs MC	0.15
$\not\!\!E_T$	0d vs MC	0.50
$\not\!\!E_T$	0h vs MC	0.77
$\not\!\!E_T$	0i vs MC	0.36
E_t jet1	0i vs MC	0.98

Table 5.5: *The table reports the Kolmogorov-Smirnov (KS) tests of agreement between the data and MC ($M_{top} = 175\ GeV$) on the P_t and $\not\!\!E_T$ distributions (figure 5.3). The data are divided in three samples corresponding to three different time periods of data-taking. The visible good agreement in the transverse energy distributions is confirmed by the KS test, which is reported as well as an example.*

5.5 Spectrum Parameterization

As customary in the Template Method (described in section 4.6), we determine the parameters of an analytical function fitting the mass spectrum returned by the simulation of the signal as a function of the assumed Top mass. 30 parameters have been included in the function fitting the signal in order to describe the spectra as accurately as required by the available statistics of more than 1 fb^{-1}[3]. We used the 21 mass templates[4] ranging from 150 to 200 GeV in 2.5 GeV steps.

The function fitting the BG samples[5], which do not depend on M_{top}, has been improved with respect to past Template analyses. The number of parameters has been increased from 3 to 6 by adding an additional Gaussian function to the original simple integrand of a Γ function.

As mentioned in section 5.3, in this study the three best combinations are used, so that the Top mass is measured three times. For this reason the templates are parameterized three times as well. The reduced χ^2 values obtained

[3]The fitting function is the sum of the integrand of a Γ function and of four Gaussians. Each of these functions depends on M and on three parameters. Since M itself is allowed to depend linearly on M_{top}, (two parameters), the total number of parameters is $3 \cdot 5 \cdot 2 = 30$.

[4]These mass templates were obtained by using the MC generator `Herwig 6.508`.

[5]The BG samples were obtained using the `Alpgen v1.3.3` and `Herwig` generators.

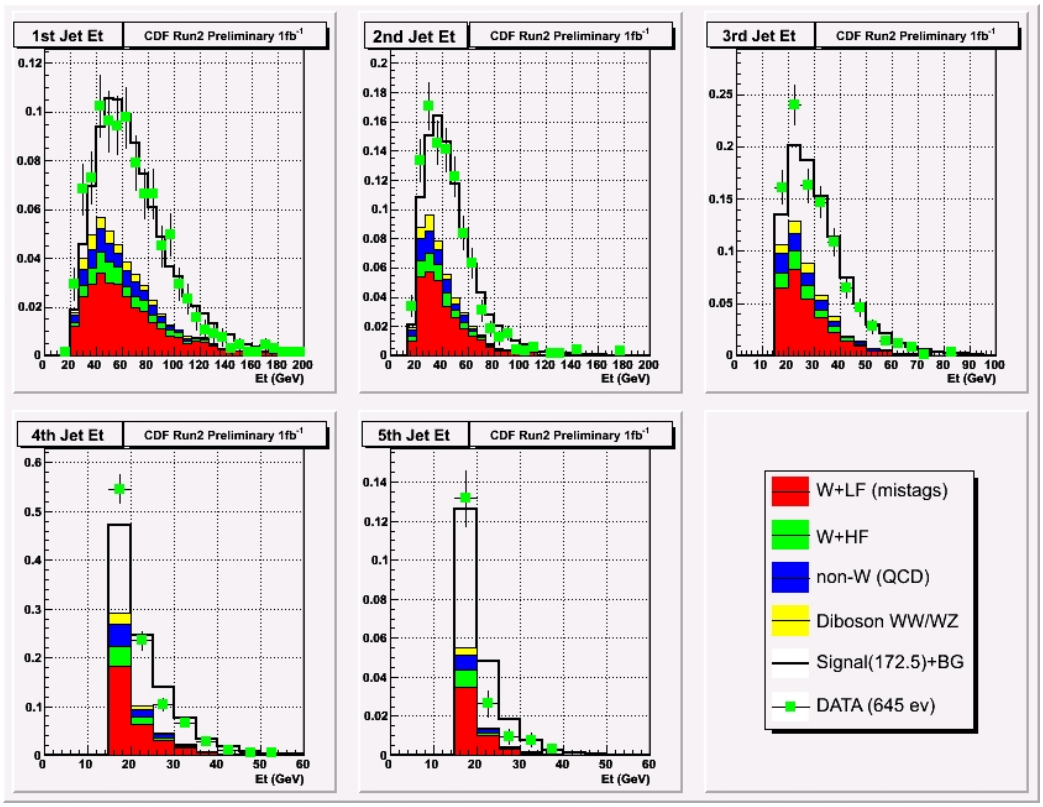

Figure 5.2: *Transverse energy distributions of the five leading jets in the selected data and MC events. Blessed plot.*

for fitting respectively the first, second and third combination of the signal templates are 1.1334, 1.0838, 1.1725.

Figure 5.4 shows the three combined background samples together with the parameterization obtained. The first combination histogram and analytic function show an isolated peak at about 110 GeV at first sight surprising. However, it could be explained as follows:

When the background events are reconstructed as if they were Tops, because of the 15 GeV jet p_t cut (see table 4.1 for the pretag sample) which is much lower than the 81 GeV mass of the W, the χ^2 turns out to be best when the two most energetic jets (closer to the W mass) are assigned to the hadronic W. The two remaining less energetic jets (closer to the 15 GeV cut) are then taken as b-jets and associated to the Ws to form the t and $t\bar{t}$ mass. The fitter is thus biased to indicate a Top mass not much more than by 15 GeV of the W mass, which amounts to about $105 - 115$ GeV as in the peak in question. The second and third combinations would correspond to assignments of higher energy jets as b-jets, and the Top mass would result larger with a larger χ^2 since the W

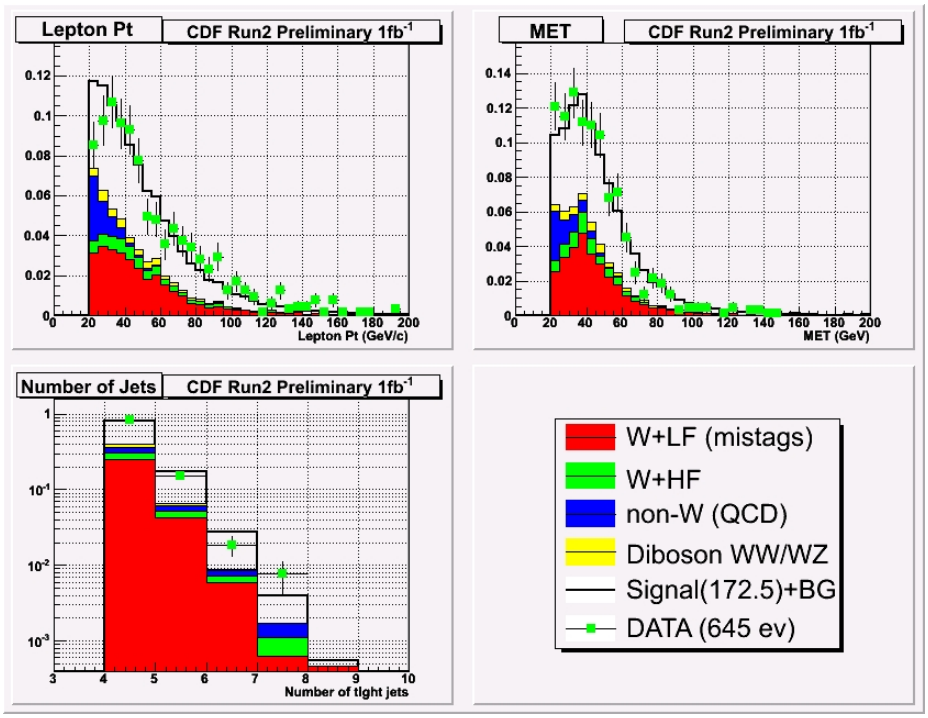

Figure 5.3: *Distributions of lepton transverse momentum, $\not\!\!E_T$ and number of jets in the selected data and MC samples. Blessed plot.*

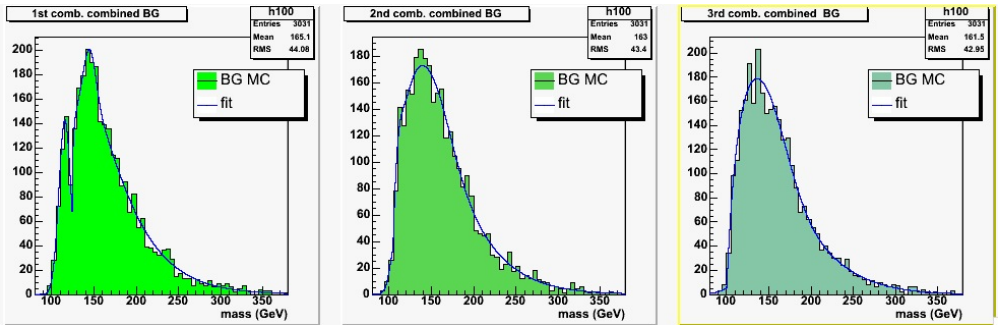

Figure 5.4: *Mass distributions of BG events (all channels added) in the three combinations. The histograms show the MC events, the fitted continous curves are the sum of two Gaussians and of the integrand of a* Γ *function.*

mass is still imposed on the hadronic W by the fitter. The peak at low mass would be washed out and the χ^2 be less good.

As a check of this interpretation we made a test by increasing the 15 GeV jet p_T cut and we observed this peak disappearing.

The three parameterizations for four out of the 21 mass templates are shown in figure 5.5.

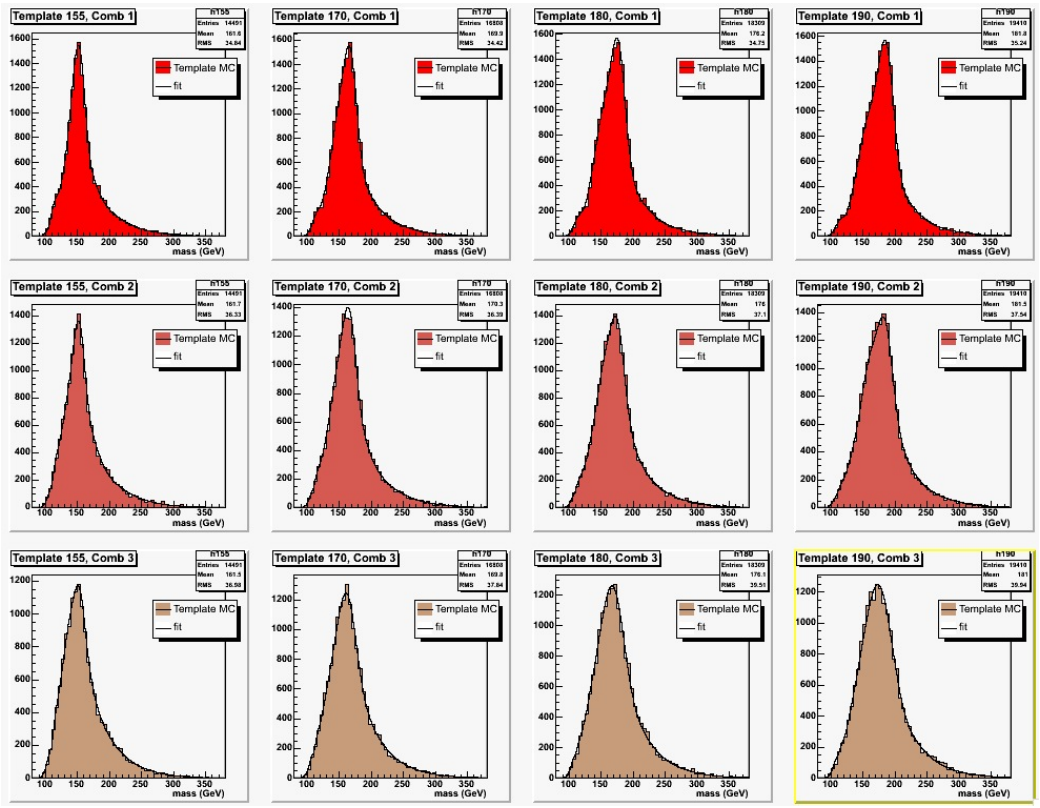

Figure 5.5: *Left to right: mass templates for* 155, 170, 180, 190 GeV/c^2 *Top masses and (top to bottom) for the first, second and third combination. As expected, the higher the combination rank, the wider the template is. This is due to the decreasing fraction of correct combinations in the samples.*

Three mass distributions have been parameterized for the three best reconstructions of the candidate events. They allowed three separate (albeit correlated) measures of the Top mass. The following paragraph will introduce the adopted method for combining together the results of the three measures.

5.6 The BLUE Method

Correlated measures of the same quantity cannot be simply combined with a weighted mean. To allow the combination of our three measures of the Top mass, the BLUE method was used as appropriate.

5.6.1 Introduction to BLUE

The BLUE method (Best Linear Unbiased Estimate) [20] is a statistical procedure for combining different correlated measurement of the same physical quantity. The correlations are taken into account by means of the error matrix E.

In order to apply BLUE, one computes a set of parameters α_i to be used as weights to linearly combine the single measures x_i:

$$x_{combined} = \sum_i x_i \alpha_i \tag{5.7}$$

with the constrain:

$$\sum_i \alpha_i = 1 \tag{5.8}$$

The parameters vector α_i is computed in such a way as to minimize the combined variance given by equation 5.9, where E_{ij} is the correlation matrix.

$$\sigma^2_{combined} = \sum_i \sum_j E_{ij} \alpha_i \alpha_j \tag{5.9}$$

In our 3-dimensional problem the combined variance is:

$$\sigma^2_{combined} = \begin{pmatrix} \alpha_1 & \alpha_2 & \alpha_3 \end{pmatrix} \begin{pmatrix} \sigma_1^2 & \sigma_{12} & \sigma_{13} \\ \sigma_{12} & \sigma_2^2 & \sigma_{23} \\ \sigma_{13} & \sigma_{23} & \sigma_3^2 \end{pmatrix} \begin{pmatrix} \alpha_1 \\ \alpha_2 \\ \alpha_3 \end{pmatrix} \tag{5.10}$$

By deriving equation 5.10 with respect to two independent αs and imposing the derivatives to be 0 one finds the minimum $\sigma^2_{combined}$ value. The solution provides the three α values by imposing unitarity (equation 5.8).

This method guarantees the combined variance to be not larger than the smallest variance given in input.

All error matrix elements are needed to minimize the combined variance. Since the matrix is symmetric, in the 3D case we need to calculate 6 independent matrix elements.

The 3 off-diagonal elements can be obtained as:

$$\sigma_{ij} = \rho_{ij} \sigma_i \sigma_j \tag{5.11}$$

$$\rho_{ij} = \frac{\sigma_{ij}^{PE}}{\sigma_i^{PE} \sigma_j^{PE}} \tag{5.12}$$

5.6.2 3 Best χ^2s Using BLUE

To determine the 6 independent elements of the correlation matrix, we run a large number of PEs. The analysis of the PEs must preserve the correlations between the three combinations. Each PE delivers for each event the mass values returned by the first, second and the third combination which are entered into separated spectra. The results of the fits to the three spectra are filed together in a row.

The calculation of the the weights α_i and of the combined mass and combined measurement error m_B and σ_B proceeds as follows:

- from the full PE sample, we compute the correlation factors $\rho_{12}, \rho_{13}, \rho_{23}$ according to equation 5.12;
- for the n-*th* PE we calculate the n-*th* covariances $\sigma_{12}, \sigma_{13}, \sigma_{23}$ obtaining the full error matrix (equation 5.11) from its parameter set $m_1, m_2, m_3, \sigma_1, \sigma_2, \sigma_3$ (as well as for *the* data set). A covariance is calculated as $\sigma_{ij}^N = 1/N \sum_{ij}(x_i - \bar{x})(y_j - \bar{y})$;
- we calculate the n-*th* set of $\alpha_1^{(n)}, \alpha_2^{(n)}, \alpha_3^{(n)}$ factors;
- from the three α distributions, the mean is computed. The $\bar{\alpha_1}, \bar{\alpha_2}, \bar{\alpha_3}$ weights are applied to every single PE of the sample. The three α distributions for $M_{top} = 175\ GeV$ are reported color-coded in figure 5.6 (left). In the same figure (right) their mean values as a function of M_{top} are shown. The $\bar{\alpha_1}, \bar{\alpha_2}, \bar{\alpha_3}$ values for $M_{top} = 175\ GeV$ are reported in table 5.6;

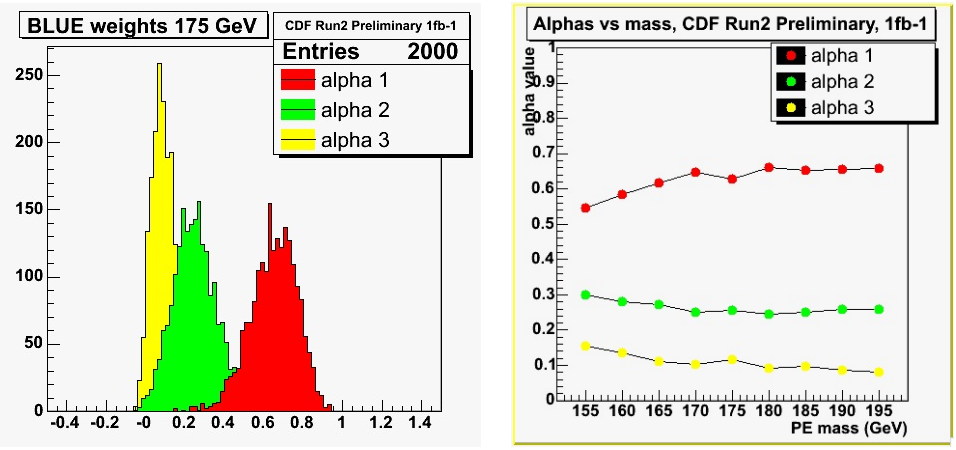

Figure 5.6: *Left: Alpha distributions for* $M_{top} = 175\ GeV$. *Right: alpha values as a function of* M_{top}. *Both plots are blessed.*

- once the α values are available, one more loop over the PEs is made to compute their BLUE-mass and its error, $m_B^{(n)}$ and $\sigma_B^{(n)}$;
- the distributions of $m_B^{(n)}$ and $\sigma_B^{(n)}$ are fitted to Gaussian functions. The two central values of the fits give the pair (m_B, σ_B). The distributions of m_B^ns and σ_B^ns for $M_{top} = 175\ GeV$ and $M_{top} = 170\ GeV$ are shown in figure 5.7.

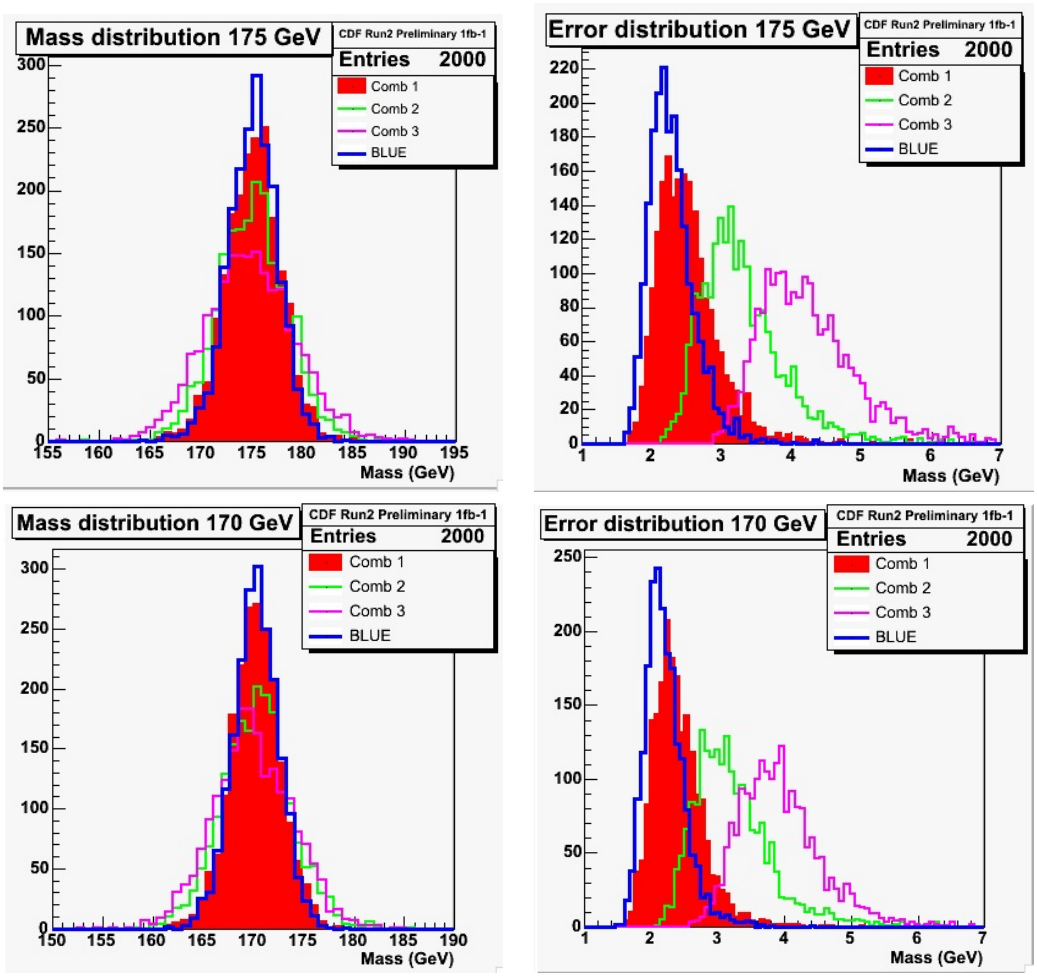

Figure 5.7: *Top left: The mass returned by the three combinations and the BLUE mass for $M_{top} = 175\ GeV$. Top right: Error distributions for the three combinations and for the BLUE combined. Although the errors of the second and third combination are larger, the information provided by these combinations reduce the BLUE errors below those of the first combination. Bottom: same distributions as in the top row, for $M_{top} = 170\ GeV$. Blessed plots.*

The procedure is slightly different for the data and for the calculation of

the systematic uncertainties. The $\rho_{12}, \rho_{13}, \rho_{23}$ values are not derived from the PEs, but are chosen as the values calculated from the template corresponding to $M_{top} = 175\ GeV$ which are reported in table 5.6. In the same table, the α values calculated for the same input mass are reported as well as an example.

Correlation factor	value
$\rho_{12}(175)$	0.3728
$\rho_{13}(175)$	0.2979
$\rho_{23}(175)$	0.3314
α (weights)	value
$\alpha_1(175)$	0.627 ± 0.003
$\alpha_2(175)$	0.255 ± 0.002
$\alpha_3(175)$	0.118 ± 0.002

Table 5.6: *Correlation factors and alpha values for $M_{top} = 175\ GeV$ MC. These values are used in the study of the systematic uncertainties and for the data, while in the analysis of the mass templates the correlation factors are computed as a function of the Top mass.*

5.7 Sanity Checks

A number of quality ("sanity") checks have been performed to prove that the adopted parameterization and the fit procedure are able to correctly reconstruct known input masses. A "blind" test is run to reconstruct the Top masses in simulated samples which are later compared to the input masses who were known only to the member of the CDF Collaboration who generated them.

5.7.1 Reconstructed Masses

Figure 5.8 shows the output masses versus 9 input values of the Top mass, from 155 to 195 GeV. Each point was obtained by running 2000 PEs.

The slopes of the fitting straight lines are 0.983 ± 0.008, 1.013 ± 0.011, 0.990 ± 0.003 for the first, second, third combination. The slope relative to the BLUE reconstruction is 0.992 ± 0.006. In all cases the slopes are fully consistent with 1.0.

The masses found in the reconstruction of a number of events are shown in table 5.7. The means of the error distributions in each set of PE's are reported in figure 5.9.

5.7.2 Pull Distributions

The *pull* variable is defined as:

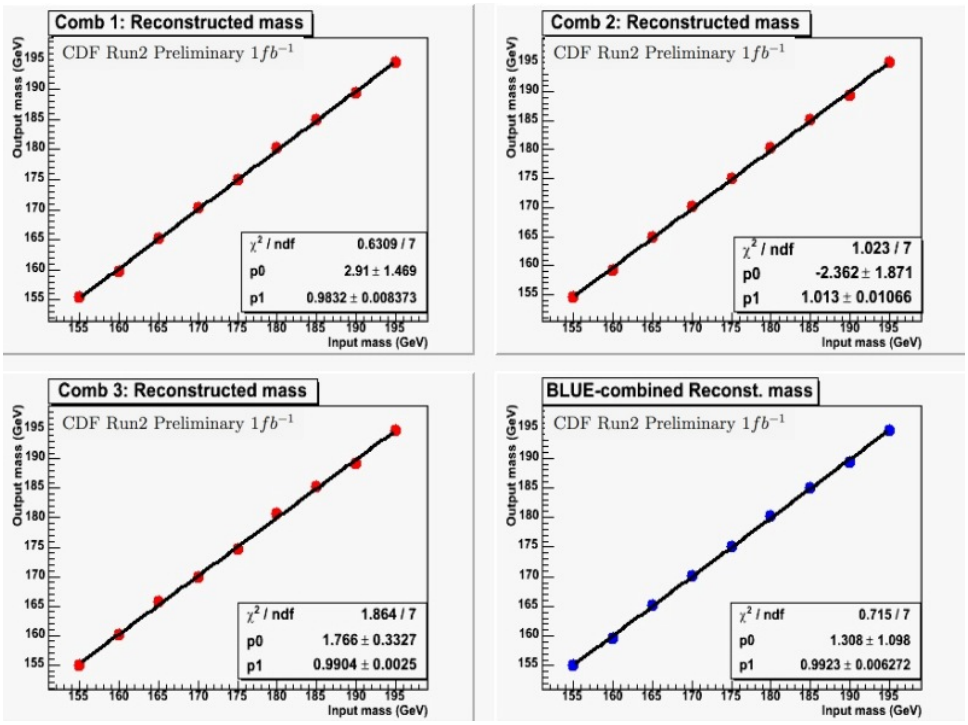

Figure 5.8: *Reconstructed masses versus input masses. Blessed plots.*

$$pull = \frac{M^{fit} - M^{true}}{\sigma^{fit}} \tag{5.13}$$

The pull gauges the goodness of the mass reconstruction. It expresses, in units of the statistical error, how much the measure differs from the input MC value. The pull distributions found in our PE's for $M_{top} = 175\ GeV$ and fitted to Gaussians are shown in figure 5.10.

The parameters of the Gaussians are close to the expected values of $y = 0$ (mean) and $y = 1$ (width). The means and widths of the pull distributions have been computed for 9 mass templates and are reported in figure 5.11. The parameters of the linear fits shown in the figure as red straight lines are reported in table 5.8.

To estimate the error in the pull values due to the limited number of PEs, we proceed as follows:

- we choose a reference mass template: $M_{top} = 170\ GeV$;
- the single bins of the mass distribution are fluctuated poissonianly 400 times, getting 400 new spectra. This is done for combinations 1, 2, 3;
- we analyze each variation of the original spectrum using our standard

Input mass (GeV/c^2)	Comb	Mass (GeV/c^2)	σ (GeV/c^2)	Improvement (%)
155	1	155.4	2.3	
	2	154.5	2.7	
	3	154.9	3.4	
	BLUE	155.0	2.1	-10.7
160	1	159.7	2.3	
	2	159.2	2.8	
	3	160.2	3.6	
	BLUE	159.6	2.1	-10.5
165	1	165.3	2.3	
	2	164.9	3.0	
	3	165.8	3.8	
	BLUE	165.3	2.1	-8.3
170	1	170.2	2.4	
	2	170.2	3.2	
	3	169.9	3.9	
	BLUE	170.2	2.2	-8.2
175	1	175.1	2.5	
	2	175.0	3.2	
	3	174.7	4.1	
	BLUE	175.0	2.2	-8.8
180	1	180.2	2.4	
	2	180.3	3.2	
	3	180.7	4.3	
	BLUE	180.3	2.2	-7.8
185	1	184.9	2.4	
	2	185.1	3.2	
	3	185.4	4.4	
	BLUE	185.0	2.2	-8.9
190	1	189.4	2.3	
	2	189.4	3.2	
	3	189.2	4.6	
	BLUE	189.4	2.1	-9.1
195	1	194.6	2.4	
	2	195.2	3.2	
	3	194.9	4.7	
	BLUE	194.7	2.1	-10.1

Table 5.7: *Results of measurements on pseudodata sets extracted from the mass templates and background samples. The measurements for the three best combinations are compared with the BLUE measurement. The estimated improvement in the error obtained with BLUE is about* 10%.

procedure and generating for each of them 400 pseudo-experiments, then we fit them. We distribute the fitted masses and errors from the fits and file the means and the widths of the distributions;

- for each variation and for each combination we plot the pull distribution and fit it to a Gaussian. The means are entered into a "means" histogram and the widths into a "widths" histogram;
- the "means" and "widths" histograms are fitted to Gaussians whose widths provide the error on the pull mean and on the pull width for $M_{top} = 170\ GeV$;
- for the masses $i \neq 170$, to allow for the different number of events passing

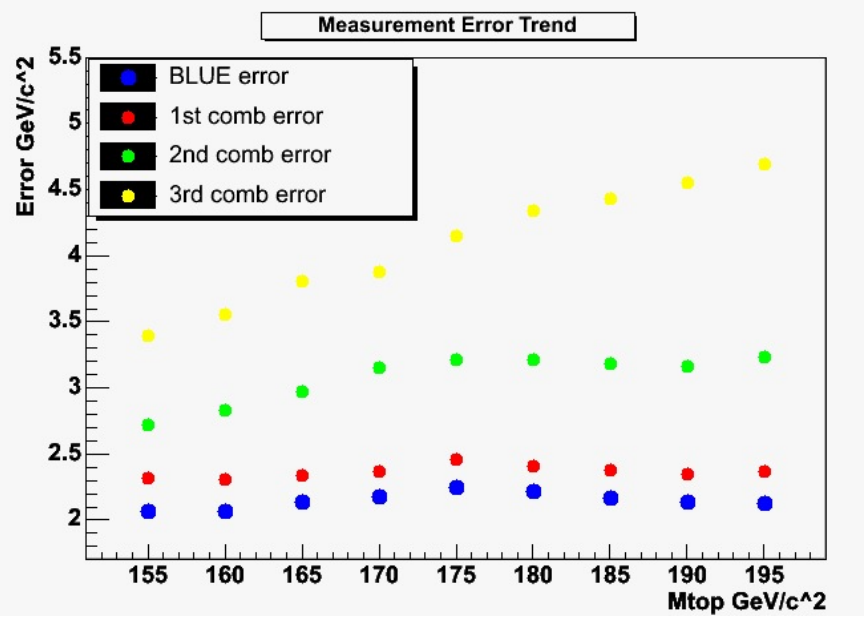

Figure 5.9: *The measurement errors as a function of M_{top} are reported for the three best combinations and for the BLUE-combined one.*

the cuts, we correct the error by the factor $\sqrt{N_{170}/N_i}$.

As the first, second, third combination reconstructed masses, the BLUE-reconstructed masses can be compared with the nominal values to provide a quality check of the capability to reconstruct the masses by using the 3-Best χ^2s technique. The comparison between the three combinations and the BLUE one is reported in figure 5.12, where the pull means and widths are shown in the top plots. The bottom plot shows the residuals between the input and the reconstructed masses.

Combination	p_0^{mean}	p_0^{width}
1	-0.022 ± 0.043	0.992 ± 0.024
2	-0.046 ± 0.045	0.999 ± 0.023
3	0.000 ± 0.044	0.967 ± 0.018
BLUE	-0.020 ± 0.054	0.989 ± 0.009

Table 5.8: *Parameters of the straight lines fitting the pull means and widths as a function of the Top mass. The means and widths are in good agreement with the expectations of 0.0 and 1.0.*

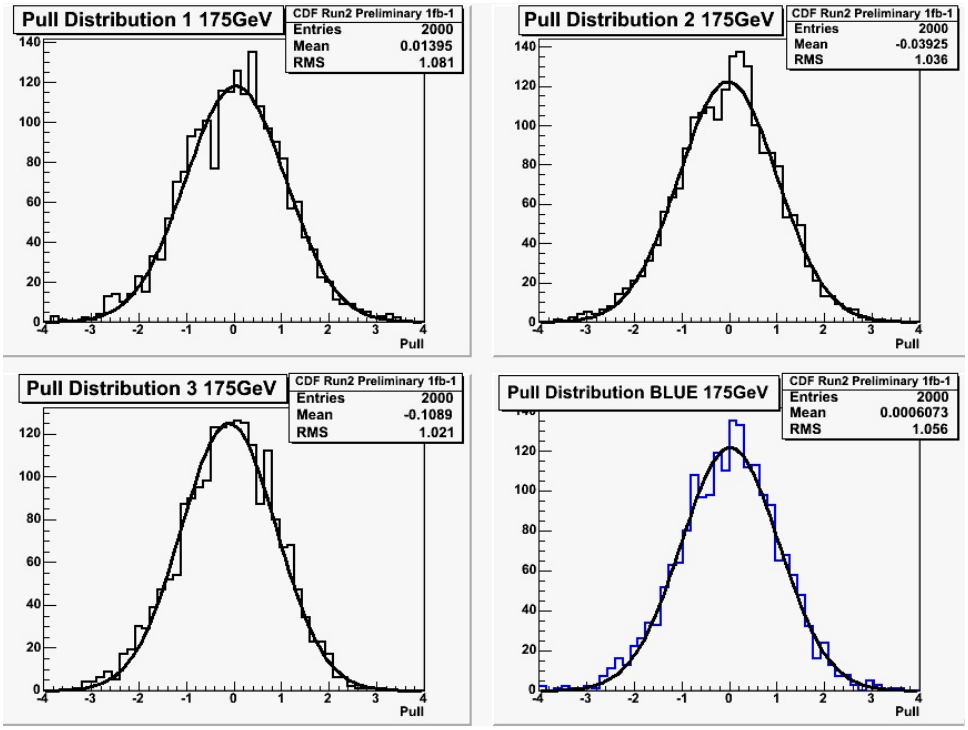

Figure 5.10: *Pull distributions for* $M_{top} = 175\ GeV$.

5.7.3 Top Mass in the Blind Samples

Five blind samples have been analyzed. We report on figure 5.13, left, in random order, the residuals between the true and the measured values with the 3-Best χ^2 technique. In figure 5.13, right, the residuals of the Pythia samples (the two last points of the right figure) are shifted by the generator systematic uncertainty (see section 5.8). The error bars give the statistical error of a single measurement of the blind masses. The single PE used for this calculation had 3358 signal events and 3031 BG events. Even before correcting for the known systematic uncertainty of the Pythia sample, the comparisons are fully satisfactory.

5.7.4 2-Best χ^2s

We tested the amount of information provided by the third combination by comparing our results to those obtained with the same method exploiting only the first two combinations. With 2 combinations only the weight calculation becomes much simpler:

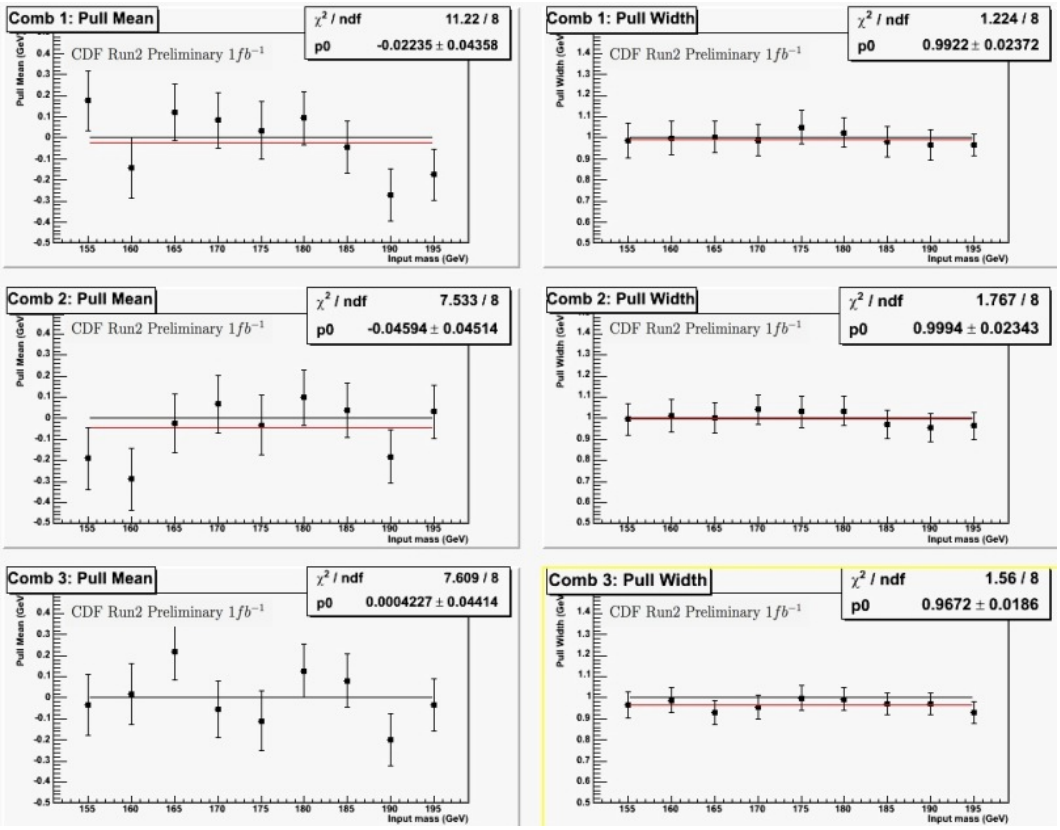

Figure 5.11: *Pull distribution means (left) and widths (right). The rows correspond to the three combinations, in order up to down. The relatively large error bars are due to the limited statistics. The red horizontal lines show the fits to a constant. Blessed plots.*

$$\alpha_1 = \frac{\sigma_2^2 - \sigma_{12}}{\sigma_1^2 + \sigma_2^2 - 2\sigma_{12}} \tag{5.14}$$

$$\alpha_2 = 1 - \alpha_1 \tag{5.15}$$

Table 5.9 reports the comparison for three representative masses. It is found that the third combination improves the statistical error by only about $1-2\%$[6]. This modest improvement allows to conclude that no effort would be justified in exploiting more than three combinations with this technique.

[6]This improvement due to the presence of the third combination corresponds to about 13 % of the whole 3-Best χ^2s method with respect to the single best combination.

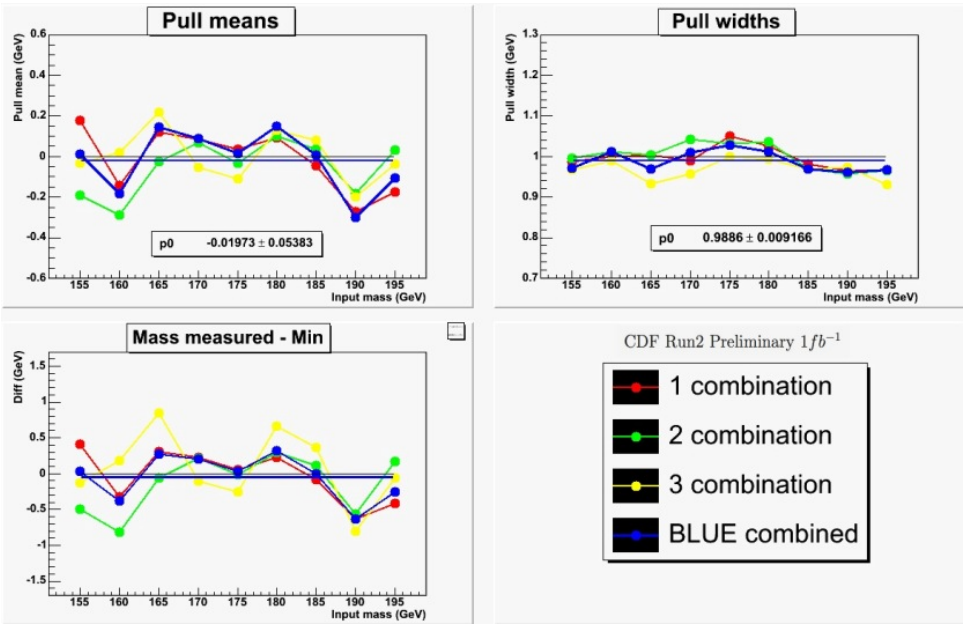

Figure 5.12: *Pull means and widths of the three best combinations and the BLUE over the studied mass range. Blessed plots.*

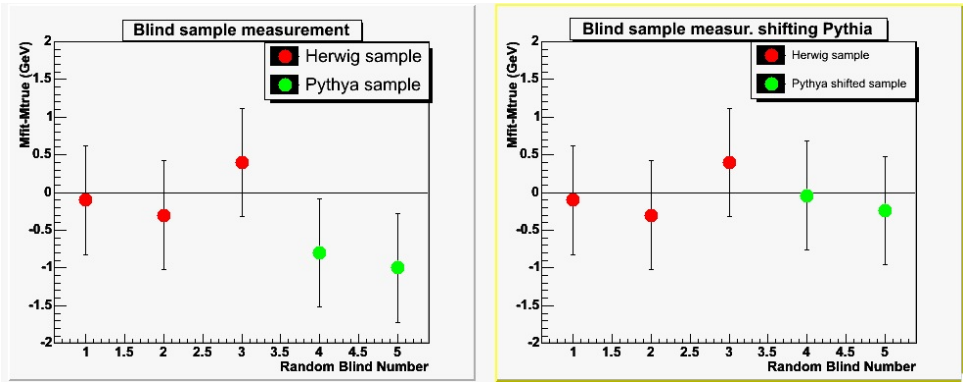

Figure 5.13: *Left: residuals between the fitted value and the nominal value of 5 blind samples in random order. Red color Herwig, green Pythia. Right: the two residuals of the Pythia samples are shifted by the generator systematic uncertainty quoted in table 5.11. Blessed plots.*

5.8 Systematic Uncertainties

We estimate now the relevant systematic contributions to the overall measurement error of the Top mass.

M_{top}	Method	Measure (GeV)	α_1	α_2	α_3	improvement (%)
165	Best	165.3 ± 2.3	1	0	0	0
	2-Best	165.2 ± 2.2	0.677	0.323	0	-7.29
	3-Best	165.3 ± 2.1	0.617	0.272	0.110	-8.15
175	Best	175.1 ± 2.5	1	0	0	0
	2-Best	175.1 ± 2.3	0.695	0.305	0	-7.32
	3-Best	175.0 ± 2.3	0.627	0.255	0.118	-8.53
185	best	184.9 ± 2.4	1	0	0	0
	2-Best	184.9 ± 2.2	0.706	0.294	0	-7.56
	3-Best	186.0 ± 2.2	0.652	0.250	0.098	-8.82

Table 5.9: *Masses from the 3-Best-χ^2 compared with the standard Best-χ^2 and the 2-Best-χ^2. This test shows how much information is contributed by the third combination. The modest contribution by the third combination indicates that using more than 3 combinations whould not provide any further improvement. Compare also with figure 5.1.*

5.8.1 Choice of the ρ_{ij} Factors

As described in section 5.6.2, we adopt a single set of correlation factors when calculating the systematic uncertainties of the data. We have tested that this simplification does not introduce any significant bias. This test was made by using a set of correlation factors appropriate to another mass when applying BLUE to measure a particular mass. We calculated the ρ_{ij} triplets for the masses $160, 175, 190\ GeV$, and studied a number of mass templates adopting the $\rho_{ij}^{160}, \rho_{ij}^{175}, \rho_{ij}^{190}$ values in the BLUE calculation. The results are reported in table 5.10.

M_{in} GeV	$M_{fit}(\rho_{160})$ GeV	$M_{fit}(\rho_{175})$ GeV	$M_{fit}(\rho_{190})$ GeV	max ΔM GeV	max $\Delta\sigma$ GeV
160	159.6 ± 2.1	159.6 ± 2.1	159.7 ± 2.0	0.03	0.07
165	165.3 ± 2.1	165.3 ± 2.1	165.3 ± 2.1	0.02	0.08
170	170.2 ± 2.2	170.2 ± 2.2	170.2 ± 2.1	0.02	0.06
175	175.0 ± 2.3	175.0 ± 2.3	175.0 ± 2.2	0.01	0.05
180	180.3 ± 2.2	180.3 ± 2.2	180.3 ± 2.2	0.01	0.02
185	185.0 ± 2.2	185.0 ± 2.2	185.0 ± 2.2	0.02	0.06
190	189.4 ± 2.2	189.4 ± 2.1	189.4 ± 2.1	0.01	0.06

Table 5.10: *The correlation factors calculated for the masses $160, 175, 190\ GeV$ are used to measure the templates $M_{top} = 160, 165, 170, 175, 180, 185, 190\ GeV$. The results are practically the same, proving that the choice of an inappropriate correlation factors triplet does not affect the mass measurement.*

The errors vary within less than 0.1 GeV when changing the ρs. This proves that the ρ can be computed for a reference mass and be applied to all studies. Therefore, the systematic uncertainties can be studied by means of a single ρ triplet. We chose the triplet obtained from $M_{top} = 175\ GeV$ whose values are reported in table 5.6.

5.8.2 Systematic Errors

Every time we model the detector, a physic process or their interaction, we introduce in the final measure some systematic uncertanty due to the imperfections of the model.
We estimate *a posteriori* the influence of these uncertainties using large samples of MC events [21] generated by changing the relevant quantity by $\pm 1\sigma$. The sample is selected and fitted with the same standard criteria used to generate and analyze the mass templates, the BG samples and the signal samples. A set of 2000 PEs is finally extracted from the signal sample and mixed with BG contamination using the same BG and signal p.d.f.'s as in the measurement. The shift in the fitted Top mass median is taken as systematic uncertainty associated with the variated quantity.

The final systematic errors have been estimated using the BLUE method and are listed in table 5.11.

The Pythia and Herwig generators are used to simulate $t\bar{t}$ final states. The two generators produce small differences in the final state and in the reconstructed Top mass. We evaluate the error associated to the generator choice as the difference between the measured mass in Pythia and Herwig $t\bar{t}$ samples with input mass $M_{top} = 178\ GeV/c^2$.

The BG shape is affected by our imperfect knowledge of the Q scale. We estimated the error in the BG shape as the maximum difference in the measured mass when using the default BG shape and the BG shapes with $4m_W^2$ and $M_W^2/4$ as Q^2 scales. This study was limited to W+LF and W+HF to represent all BG processes since these processes contribute over 77% of the entire BG sample.

The error associated to the uncertainty in the Jet Energy Scale (JES) is estimated by studying separately the contributions described in section 4.4.2. The Relative, Absolute, Underlying event, Out of Cone, Splash Out contributions were variated within $\pm 1\sigma$. The JES error is taken for each of them as half the difference between the masses measured with the jet energies shifted up and down by one standard deviation. Examples of the resulting shifts are reported in section 4.4.

The errors associated to the uncertainty in Initial and Final state gluon radiation are taken as one half the difference between the masses measured when decreasing or increasing the radiations by large amounts. This is done by CDF by using MC samples specifically produced for this purpose.

The error associated to the particular choice of Λ_{QCD} in the MRST parton distribution functions is taken as half the difference in the mass measured with choosing $\Lambda_{QCD} = 228\ MeV$ and $\Lambda_{QCD} = 300\ MeV$[7]. The error associated to the uncertainty in the CTEQ6M structure functions is obtained as one half the difference in the mass measured with altering the 20 eigenvectors by $+\sigma$ and $-\sigma$.

Three further contributions were added: 0.72 GeV to take into account an error which could come from an incorrect estimation of the BG amount (calculated as half the difference of the measures obtained using 306 BG events and 406 BG events), 0.22 GeV due to an uncertainty on the lepton P_t [22] and 0.60 GeV to take into account the b-jet uncertainty in the JES.

We assign an error due to the limited number of PEs performed to gauge each systematic uncertainty as shown in the last columns of table 5.11. Each uncertainty enters the final squared sum with the value reported in the last column, obtained as squared sum of the sub-contribitions. The values entering the sum are assigned an error which takes into account the limited MC statistics.

To evaluate this error we run a single PE using all the available 3031 BG events, and 3358 signal events in order to keep the correct signal/BG ratio. This PE gives a statistical error of 0.72 GeV. Since the sample composition is about half BG and half signal, we assume each of the two to contribute to the statistical error by $0.72/\sqrt{2} = 0.51\ GeV$ and take this as the BG contribution to the limited statistics error. The signal contribution is instead scaled by the ratio between the available signal events in the MC and the 3358 used in the test.

When the error assigned to a systematic uncertainty is larger than the estimated value, as happens in the PDF, we use the error itself as systematic uncertainty estimator.

5.9 Data Fit

After the templates were set, the likelihood fit were demonstrated to be unbiased and the systematic errors were studied, we fitted the data sample. To apply BLUE to the data we used the correlation factors chosen for the

[7]The two MC ntuples generated by using the Phythia generator at the indicated Q-scales are `ttopir` and `ttopjr` .

Systematic errors, CDF Run2 Preliminary, $1fb^{-1}$

Category	Source	Calculation	Value GeV/c^2	Sum GeV/c^2
Generator	Pythia - Herwig	`|ttopel-ttophl|`	0.76 ± 0.04	**0.76** $\pm$ 0.51
BG shape		def. BG - $4M_W^2$ BG	0.61 ± 0.04	**0.61** $\pm$ 0.55
JES	L1: Relative		0.83 ± 0.04	
	L5: Absolute		2.82 ± 0.04	
	L6: Underl. Event		0.34 ± 0.04	
	L7: Out Of Cone		2.46 ± 0.04	
	L8: Splash Out		0.37 ± 0.04	
	Total	Squared sum		**3.86** $\pm$ 0.55
Gluon Radiations	ISR	$\frac{1}{2}$|`ttopbr` − `ttopdr`|	0.68 ± 0.04	
	FSR	$\frac{1}{2}$|`ttopfr` − `ttopmr`|	0.16 ± 0.04	
	Total	Squared sum		**0.70** $\pm$ 0.51
PDF	MRST72-CTEQ5L	|`ttopir` − `ttopel`|	0.26 ± 0.04	
	MRST75-MRST72	|`ttopjr` − `ttopir`|	0.06 ± 0.04	
	40 CTEQ6 series		0.22 ± 0.04	
	Total	Squared sum		0.35 $\pm$ **0.51**
BG estimation		$\frac{1}{2}$|406 BG - 306 BG|	0.72 ± 0.04	**0.72** $\pm$ 0.39
Lepton P_t	FLAME study	[22]	0.22	**0.22**
b-jet uncert.			0.60	**0.60**
Tot. Uncert.		Squared sum		**4.2**

Table 5.11: *The estimated values of the systematic uncertainties. Results from this table have been blessed.*

systematic errors as reported in section 5.8.1 and table 5.6. The three fitted spectra are reported in figure 5.14 (top) together with the relative likelihood shapes (bottom). We tested the agreement between the data mass spectrum and the best p.d.f. resulting from the maximum likelihood fit. We used the Kolmogorov-Smirnov test and we run it for the three best combinations. The test returned the values $KS_1 = 0.904$, $KS_2 = 0.998$, $KS_3 = 0.953$.

The mass measured on the three combinations and the BLUE mass are shown in table 5.12. By applying BLUE on these three measurements, we obtained an improvement of 5.1% with respect to the first combination measure.

According to the MC studies reported in table 5.7, the expected average improvement is about 10%. The distribution of the improvements as predicted by MC simulations is displayed in figure 5.15 ($M_{top} = 175\ GeV$). The probability of getting an improvement smaller than the one observed in our data is about 23%. This shows that our finding corresponds to a rather normal fluctuation.

The final measure of the Top mass is then:

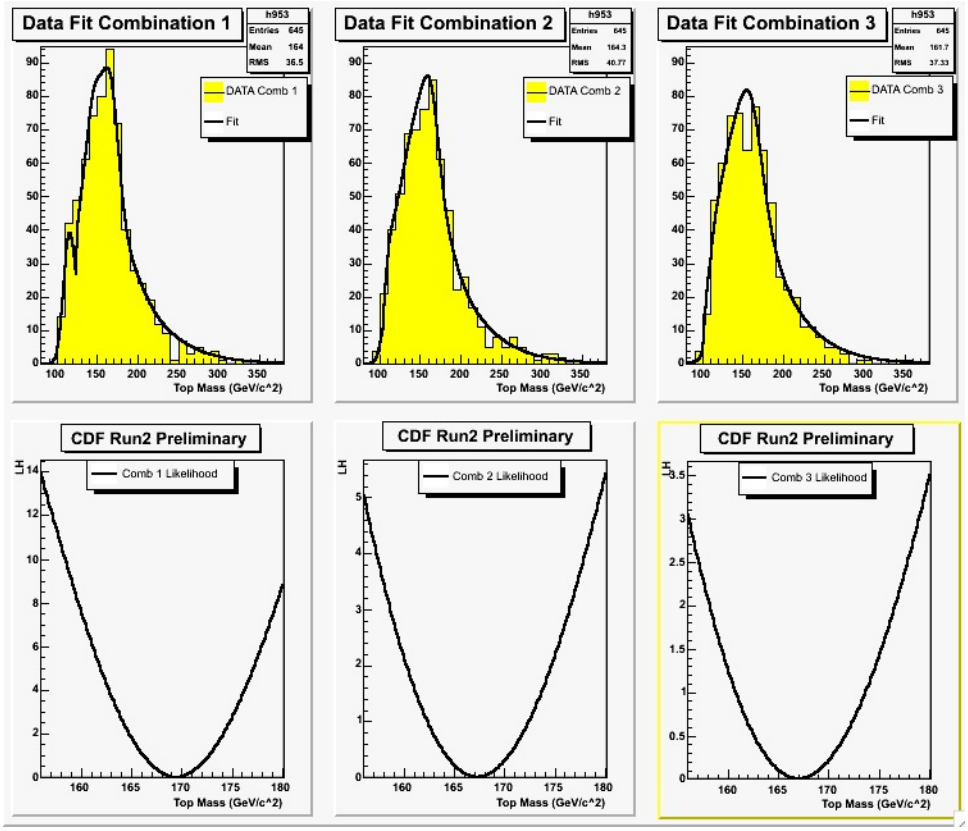

Figure 5.14: *The fitted data histograms (top) and their corresponding likelihoods (bottom). Blessed plot.*

$$M^{top} = 168.9 \pm 2.2(stat) \pm 4.2(syst)\ \frac{GeV}{c^2} \tag{5.16}$$

Results from other studies on the Top mass by CDF and DØ in all the $t\bar{t}$ decay channels are reported in Appendix C.

Data Fit (stat err only), CDF Run2 Preliminary, $1fb^{-1}$

	Constrained fit	Unconstrained fit
1 Comb	169.5 ± 2.3 GeV	169.8 ± 2.4 GeV
2 Comb	167.3 ± 3.6 GeV	168.7 ± 4.2 GeV
3 Comb	167.0 ± 4.6 GeV	169.3 ± 5.7 GeV
α_1	0.758	0.841
α_2	0.165	0.120
α_3	0.077	0.038
BLUE	**168.9 ± 2.2 GeV (stat)**	169.6 +- 2.4 GeV (stat)
Improvement	5.1%	4.0%

Table 5.12: *The results on the data fits. The BLUE-combined measurement is obtained, as mentioned in the text, using the correlation factors from* $M_{top} = 175\ GeV$. *The quoted errors are statistical only. The results reported in the table have been blessed.*

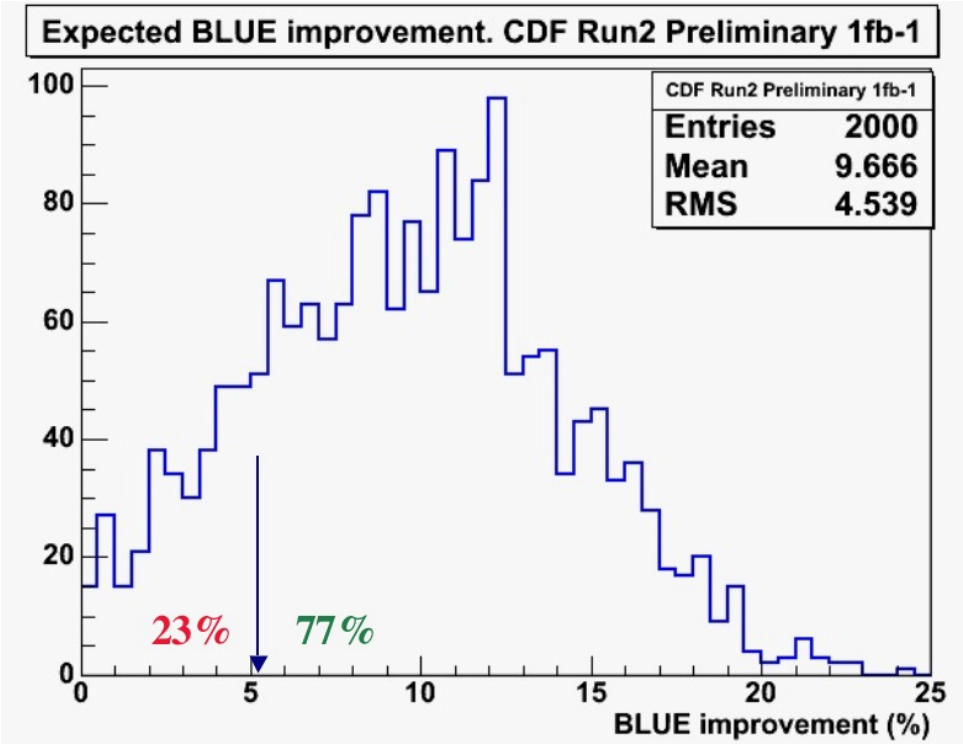

Figure 5.15: *Distribution of expected relative improvement in statistical error of the BLUE mass over the best combination mass. The plot is obtained with 2K PEs run on the template mass* $M_{top} = 175\ GeV$.

Chapter 6

Conclusions

6.1 Resumé

In this work we analyzed the first 1 fb^{-1} of data recorded by the CDF detector (section 3.2) and delivered by the Tevatron Collider(section 3.1.7) up to February 2006. These data were studied searching for the typical signature of the Top quark pairs in the semileptonic channel (sections 1.2.2 and 4.1).

The data sample collected was studied by comparing to a sample composed of simulated signal and background events with the Template Method (see section 4.6). An improved method, the *3-Best* $\chi^2 s$, was applied (chapter 5) to the standard template procedure in order to improve the statistical resolution. An improvement of 5.1% on the statistical error was obtained on the data.

6.2 Next Steps

The combination of the technique shown in this work with other techniques is expected to produce the best final Top mass measure. In particular, we believe that the best result could be obtained by combining the *3-Best* $\chi^2 s$ and the 2-dimensional TM (TMT2D) (see appendix A) because the TMT2D reduces by ~ 2 with the present statistics the error due to JES. Moreover, the JES error becomes statistically limited rather than being a systematic error as in the 1-dimensional TM. The *3-Best* $\chi^2 s$ can further reduce the statistical error, as shown in chapter 5.

The application of the *3-Best*χ^2s method here described to the TMT2D method could improve, in the pretag sample, the statistical+JES error by the average improvement of $\sim 10\%$ (as from figure 5.15); in this case the overall error of this TM analysis the measure could be very close or even smaller than

the one from ME+JES (see appendix B and C), being however less dependent on theoretical assumptions. We consider this development of the present study to be very realistic and worth to be attempted as soon as possible.

.

Appendix A

Bidimensional Template Method (TMT2D)

A new technique [21] was recently applied to the Top quark mass study which makes use of the Template Method. This technique improves the TM by running a 2-dimensional likelihood fit on the reconstructed Top mass M^{reco} and on the the invariant reconstructed mass of the two light jets[1] M_{jj} which are attributed to the W decay.

The jet energy scale is varied within the uncertainty to make M_{jj} approach at best the known W mass.

In order to allow the likelihood fit run on the reconstructed W mass, some templates are created by variating the jet energy scale (JES) by 1,2,3 σ as shown in figure A.1.

The likelihood equation 4.15 becomes:

$$\mathcal{L}(M_{top}) = \mathcal{L}^{sig} \times \mathcal{L}^{BG} \times \mathcal{L}^{M_{jj}} \tag{A.1}$$

The new term, due to the dijet reconstructed mass, is obtained as follows:

$$\mathcal{L}^{M_{jj}} = \prod_{k=1}^{N \cdot C_i} \frac{n_s P_s(M_{jj,k}; M_{top}, \Delta_{JES}) + n_b P_b(M_{jj,k})}{n_s + n_b} \tag{A.2}$$

where C_i (combinatorics in reconstructing the hadronic W mass) is $C_i = 1, 3, 6$ when the event is double-tagged, single-tagged, non-tagged. The other symbols are as in section 4.6.

[1] When the event is double-tagged, there is no ambiguity on the light jet identification. When the event is single-tagged or non-tagged, the M_{jj} is affected by a combinatorial background as reported in section 4.6.1 for the M^{reco} (3 combinations for the single-tagged and 6 for the non-tagged). All possible reconstructions are associated to a χ^2 value according to equation 4.8 and the reconstruction corresponding to the lowest χ^2 value is chosen.

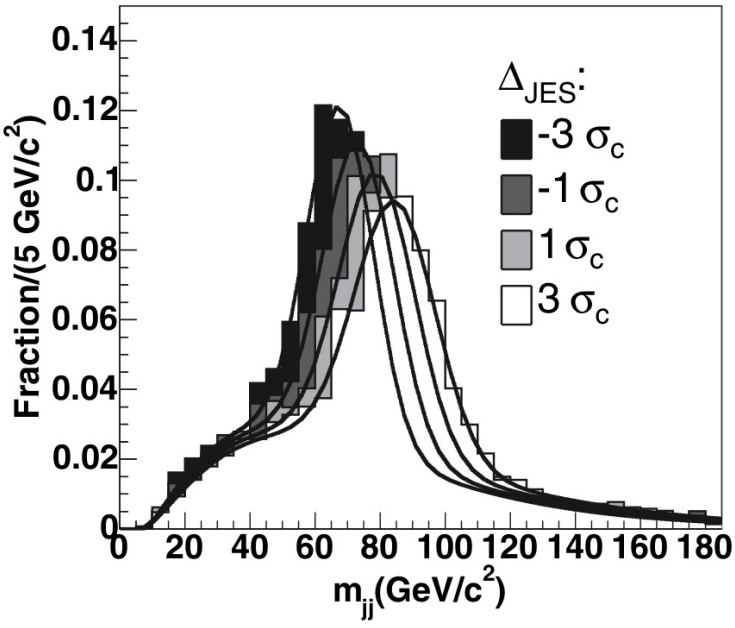

Figure A.1: *Templates used to parametrize the variation of JES from* -3σ *to* 3σ*. The plot is for* $M_{top} = 180$ *GeV and for double-tagged events [21].*

The 2-dimesional likelihood shape, studied separately for the different subsamples (table 4.1) of double-tagged, single-tagged, non-tagged events, appears as in figure A.2. Since the fit takes into account the JES, this method returns a statistical error on the Top mass that includes the JES error and a systematic error. The JES is known, in the 1-dimensional TM, to be responsible for the largest part of the systematic error. In this new analysis it contributes to the statistical error only.

With the two dimensional fit the error on JES was reduced by about a factor of two. A next step being considered to allow a further improvement with the TM would be to exploit three combinations in event reconstruction, as done in this thesis for the one-dimensional fit.

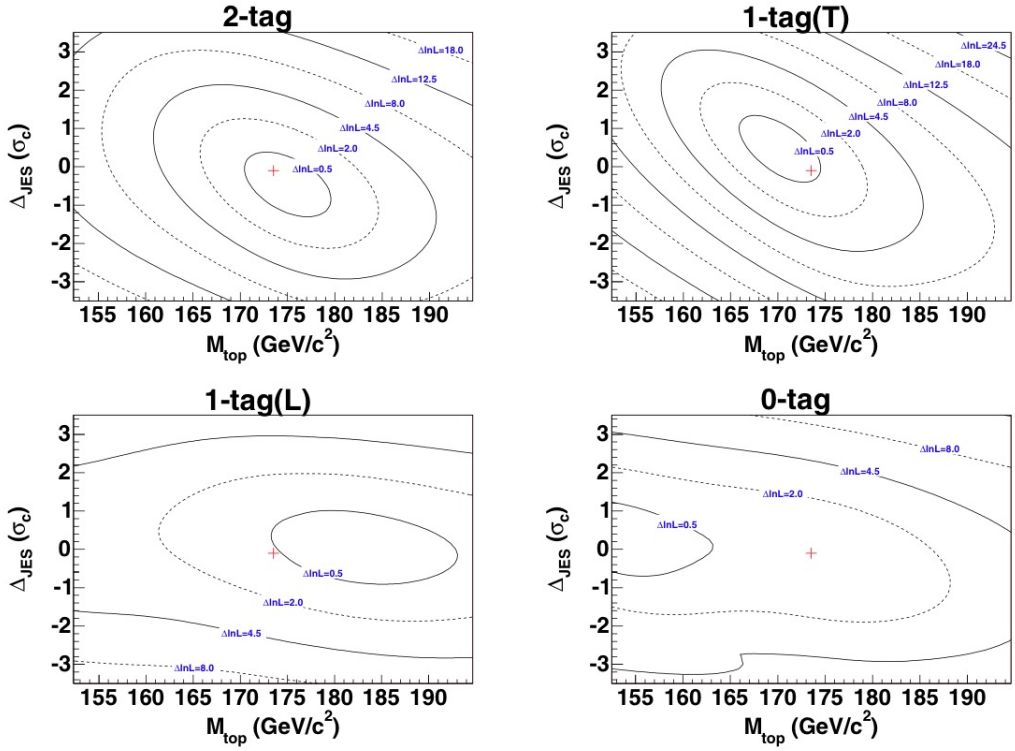

Figure A.2: *The likelihood shapes are 2-dimensional. The top-left plot is relative to the double-tagged event subsample, the top-right and bottom-left to the single-tagged event subsample (Tight and Loose cuts on jet energy respectively), the bottom-right to the non-tagged events. Contours of equal likelihood value are traced. The cross shows the point of maximum likelihood position in the combined fit [21].*

Appendix B

The Matrix Element Method (ME)

The Template Method and the Matrix Element Method (ME) are the two Top mass reconstruction methods providing the best results. We introduce here briefly the ME method which was applied by the DØ Collaboration to the Run 1 data [23]. Other methods exist, such as the Decay Length Technique (L_{xy}), the Neutrino Weight Method [24] [25], the Dynamical Likelihood Method (DLM) developed by CDF [26] which is similar to the ME method, the Ideogram Method and more.

The main idea of the ME Method is to obtain a Likelihood function for a combination of N $t\bar{t}$ and BG events as the product of single event likelihoods:

$$L(\vartheta) = \prod_{i=1}^{N} f(x_i; \vartheta) \tag{B.1}$$

where ϑ is a vector of primary interaction parameters and x_i is a vector of measured quantities. Once the L function is determined, the mass measure and its associated error are given by $L_{MAX} \pm s$ as from the following equation.

$$-\ln L(\vartheta) = -\ln L_{MAX} + \frac{s^2}{2} \tag{B.2}$$

Among the ϑ parameters we are interested in M_{top}. The function f is given by the probability $\mathscr{P}(x; M_{top})$ of each particular *observed* event to be a $t\bar{t}$ decay $\mathscr{P}_{t\bar{t}}(x; M_{top})$ or to be a BG event $\mathscr{P}_{BG}(x)$:

$$\mathscr{P}(x; M_{top}) = \sum_{j=1}^{k} c_j \mathscr{P}_j(x; M_{top}) \tag{B.3}$$

where the $\mathscr{P}_j$ can be $\mathscr{P}_{t\bar{t}}$ or one of the $\mathscr{P}_{BG}$s. Currently, ME analyses use one single BG probability function which is modeled on the $W + 4p$ BG[1]. If c_1 is the Top fraction in the sample, the $\mathscr{P}$ is:

$$\mathscr{P}(x, c_1; M_{top}) = c_1 \cdot \mathscr{P}_{t\bar{t}}(x; M_{top}) + (1 - c_1) \cdot \mathscr{P}_{BG}(x) \tag{B.4}$$

It is necessary to connect the probability to *observe* an event $\mathscr{P}(x; M_{top})$ to the probability to *produce* it $P(x; M_{top})$ by considering the acceptance function, which accounts for the geometric acceptance of the detector and the selection rules estabilished at trigger and offline level.

$$\mathscr{P}_{t\bar{t}}(x; M_{top}) = \frac{Acc(x)P_{t\bar{t}}(x; M_{top})}{\int Acc(x)P_{t\bar{t}}(x; M_{top})dx} = \frac{Acc(x)P_{t\bar{t}}(x; M_{top})}{\langle Acc(x)\rangle_{t\bar{t}}(M_{top})} \tag{B.5}$$

A similar equation can be written for the probability to observe a BG event. When the likelihood will be minimized, terms like the common acceptance on the numerator of equation B.5 will not affect the result because the weak dependence on M_{top} can be neglected. Equation B.1 becomes:

$$L(M_{top}) = \prod_{i=1}^{N} \Big[c_1 \frac{P_{t\bar{t}}(x_i; M_{top})}{\langle Acc(x)\rangle_{t\bar{t}}(M_{top})} + (1 - c_1) \frac{P_{BG}(x_i)}{\langle Acc(x)\rangle_{BG}} \Big] \tag{B.6}$$

A further important ingredient is a function allowing to transform the *parton-level* y-quantities to the measured *detector-level* x-quantities, so that it becomes possible to relate the probability functions of observed variables to the interaction parton states. Such transfer function $W(x, y)$, if we assume that lepton, neutrino and jets angles are well measured, can be written as follows:

$$W(x, y) = \delta^3(p_l^y - p_l^x)\delta^3(p_\nu^y - p_\nu^x) \prod_{j=1}^{4} \frac{1}{(p_j^x)^2} \delta^2(\Omega_j^y - \Omega_j^x) \prod_{i=1}^{4} W_{jet}(E_i^y - E_i^x) \tag{B.7}$$

The function $W_{jet}(E_i^y - E_i^x)$ is the probability of measuring a jet with energy E^x if the jet corresponds to a parton of energy E^y. This function is parametrized as the sum of two gaussians describing the $(E_{jet}^{measured} - E_{parton})$ distribution. Once the transfer function is defined, we can write an expression for $P_{t\bar{t}}(x; M_{top})$ (and in a similar way for $P_{BG}(x)$) in order to compare the measured event properties with the knowledge we have of the physics of $t\bar{t}$ production and decay:

$$P_{t\bar{t}}(x; M_{top}) \propto \int d\sigma(y) dq_1 dq_2 f(q_1) f(q_2) W(x, y) \tag{B.8}$$

[1] In the rare case of single Top EW production the BG depends on M_{top}.

where $f(q_{1,2})$ are the structure functions of the incident partons, $d\sigma(y)$ is the parton-level differential cross section, x and y are the sets of detector-level and parton-level 4-vectors. The differential cross-section can be written for a 6-partons final state as the L+J channel is, as:

$$d\sigma \propto \sum_{perm,\nu} \frac{|\mathcal{M}|^2}{\sqrt{(q_1 \cdot q_2)^2 - m_1^2 m_2^2}} d\Phi_6 \tag{B.9}$$

where Φ_6 is the six-particles phase-space and $\mathcal{M}$ is the matrix element (amplitude). The sum is over the 12 (in pretag events) possible parton assignments to the jets and the two algebraic solutions for the neutrino momentum (see section 4.6.1). The 32-D problem of knowing the 4-vectors of 6 outgoing and 2 incoming particles reduces to five undetermined variables after allowing for the 27 available constraints (8 known masses of incoming and outgoing objects, 4 conservation equations, 8 well-measured angles, 3 lepton energy and angles considered well measured, 4 incoming momentum components (assumed to be zero).

We have:

$$d\Phi_6 = \delta^4\Big(q_1 + q_2 - \sum_{i=1}^{6} p_i\Big) \prod_{i=1}^{6} \frac{d^3 p_i}{(2\pi)^3 2E_i} \tag{B.10}$$

Equation B.8 can be now extended by equations B.9 and B.10 and simplified by using the constraints to eliminate the integrals over q_1, q_2, p_T^ν and ignoring the incoming quark masses so that $\sqrt{(q_1 \cdot q_2)^2 - m_1^2 m_2^2} \propto |q_1||q_2|$. We get:

$$P_{t\bar{t}}(x; M_{top}) \propto \int \sum_{perm,\nu} \frac{|\mathcal{M}|^2 f(q_1) f(q_2)}{|q_1||q_2| E_l E_\nu} \times \prod_{i=1}^{N_{jet}=4} \frac{d^3 p_i}{E_i} W(E_i^{jet}, E_i^{parton}) \delta(\Omega_i^{jet} - \Omega_i^{parton}) \tag{B.11}$$

The total squared matrix element $\mathcal{M}$ [27] for the production and the decay process $q\bar{q} \to t\bar{t} \to (W^+ b)(W^- \bar{b}) \to (\bar{e}\nu b)(d\bar{u}\bar{b})$ averaged over the initial quark's color and spin and summed over the final colors and spins is computed as:

$$\sum |\mathcal{M}|^2 = \frac{g_s^4}{9} \mathcal{T}\bar{\mathcal{T}}(2 - \beta^2 \sin^2 \theta_{qt}) \tag{B.12}$$

where θ_{qt} is the angle between the incoming q and the t quarks, g_s is the strong coupling constant and β is the t-quark velocity in the $q\bar{q}$ system rest frame. A similar equation can be written for the BG process probability. The $\mathcal{T}$ factor comes from the process $t \to W^+ b \to \bar{e}\nu_e b$ and the $\bar{\mathcal{T}}$ comes from the process $\bar{t} \to W^- \bar{b} \to d\bar{u}\bar{b}$. Both factors depend on the Top and W widths and their kinematical and pole masses, on the angles involved in each intermediate decay vertex in the product's rest frame and on the weak coupling constant.

As customary for this method, equation B.11 coordinates are eventually changed from cartesian to spherical to allow for some simplifications before integrating on the new variables. The integration is performed numerically by using MC integration codes like VEGAS.

Equation B.11 (and the similar one for the BG) allows to associate to the observables of a candidate $t\bar{t}$ a probability density function. Figure B.1 shows an example of probability functions calculated for twenty MC events generated at $M_{top} = 178\ GeV$. In figure B.2 we see the negative log-likelihood obtained with the same twenty events as from equation B.2.

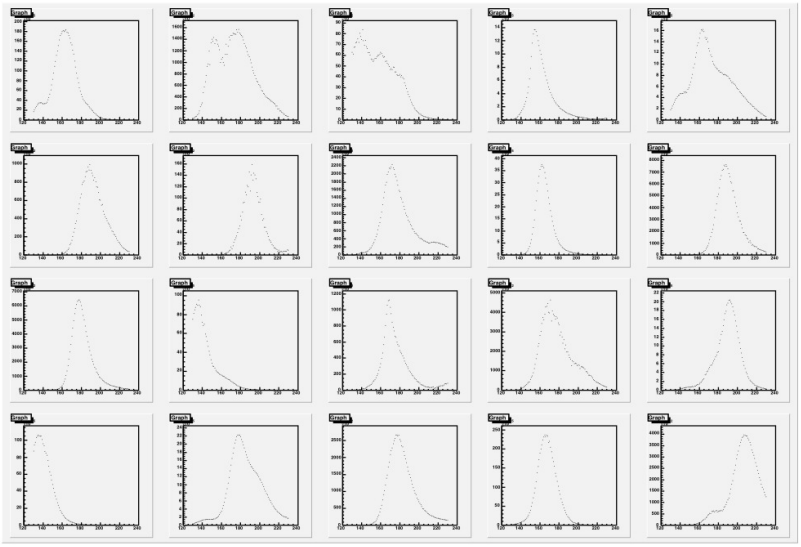

Figure B.1: *Unnormalized probability functions for twenty MC events ($M_{top} = 178\ GeV$) of being originated from $t\bar{t}$ states, the Top having the mass reported on the x-axis.*

The ME method, as discussed above, makes use of all known theoretical knowledge to the observed quantities in order to extract as much information as possible. In doing that it relies on theoretical assumptions and applies mathematical simplifications. Although this can be considered as a weakness of the principle, the method has the advantage of accounting for all the possible jet-to-parton combinations. A smaller statistical errors with respect to the Template Method is accordingly obtaines.

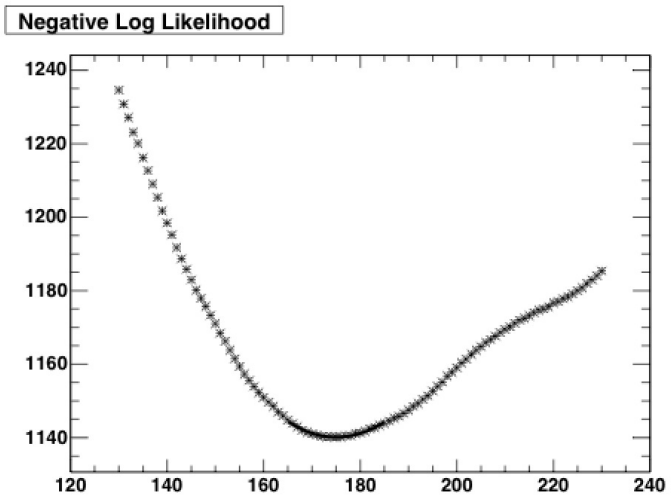

Figure B.2: *Negative log-likelihood obtained from the twenty MC events shown in figure B.1.*

Appendix C

Available Top Quark Mass Measurements (Spring 2007)

Figure C.1 shows a number of recent mass measurements by the DØand the CDF experiments. The combination of all channels of both experiments has an error of about 1.1%.

Up to now (March 2007) the best single measurement is the CDF measurement in the single lepton channel (top line in table C.1).

Method	pb^{-1}	channel	M_{top}	Stat err	Syst. err.
ME+JES in situ	1030	L+J	170.9	2.2 (JES)	1.4
TMT2D	1030	L+J	173.4	2.5 (JES)	1.3
TMT1D 3-Best	1030	L+J	168.9	2.2	4.2
ME	1030	DIL	164.5	3.9	3.9
TMT1D	1020	HAD	174.0	2.2	4.8
TMT1D+ME	943	HAD	171.1	3.7 (JES)	2.1
All best	1030	ALL	170.9	1.4	1.9

Table C.1: *Most relevant measures of the Top mass in the three main decay channels at CDF as at March 2007 after analyzing about* 1 fb^{-1} *of data. The last line reports the combination of the best measurements in each channel. The statistical errors labeled "JES" account also for the Jet Energy Scale systematics. Masses and errors are in* GeV/c^2.

The present analysis, done by making no use of *b*-tag information, was performed to show the effectiveness of the *3-Best* $\chi^2 s$ method applied to the Template Method. More precise measurements were obtained at CDF by making

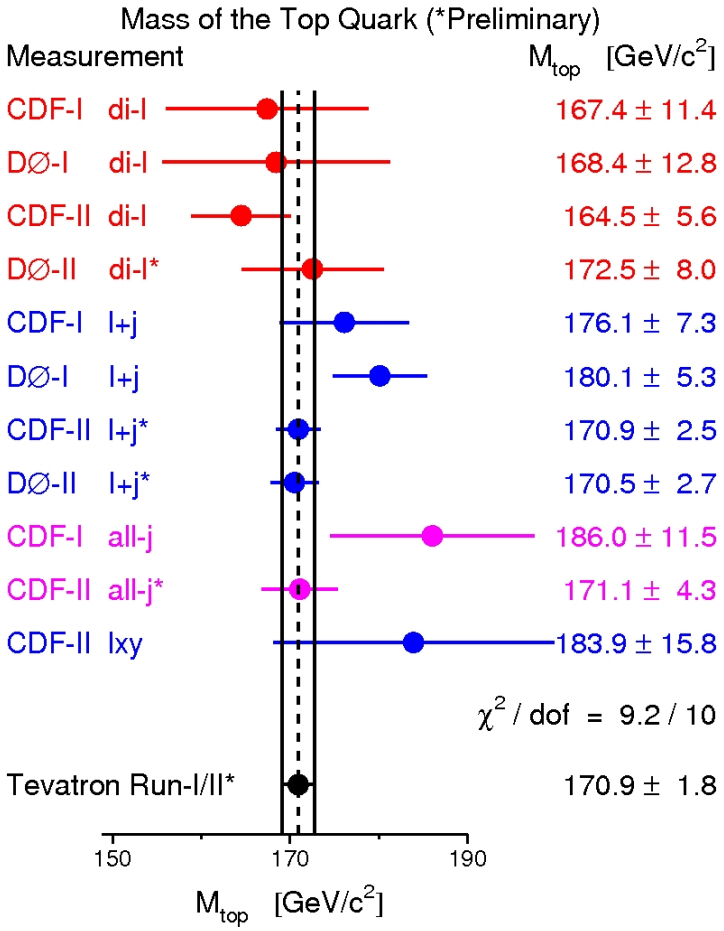

Figure C.1: *Comparison of a number of measurements of teh Top quark mass by the DØ and the CDF experiments.*

use of b-tag information. However, with the *3-Best* $\chi^2 s$ it is possible to reduce the statistical error by recovering some information which is lost when using the first combination only. We measured a Top mass of $168.9 \pm 2.2 \pm 4.2$ GeV where the statistical error was improved by about 5% making use of the BLUE technique applied to the Template Method. By MC simulations an average improvement of this error by more than 10% is predicted in average.

Index

Bibliography

[1] Andrea Bocci. *Search for $W/Z \rightarrow jets + \gamma$ Events in Proton-Antiproton Collisions at the Fermilab Tevatron.* PhD thesis, Rockefeller University, 2004.

[2] E. Shabalina for the CDF and DØ Collaborations. Top quark production at the Tevatron. *Eur. Phys J C 33, s01, s472-s474*, 2004.

[3] Salvatore Rappoccio. *Measurement of the $t\bar{t}$ Production Cross Section in $p\bar{p}$ Collisions at $\sqrt{s} = 1.96TeV$.* PhD thesis, Harvard University, 2005.

[4] D. Rainwater D. Chekraborty, J. Konisgberg. Reviwe of Top Quark Physics. *arXiv/hep-ph/0303092*, 2003.

[5] The CDF Collaboration. Evidence for Top Quark Production in $p\bar{p}$ Collisions at $\sqrt{s} = 1.8$ TeV. *CDF Internal Note 2595*, 2004.

[6] A. Artikov M. Giunta *et al.* CDF Central Preshower and Crack Detector Upgrade. *submitted to Nucl. Inst. and Meth. A in Feb, 2007*, 2007.

[7] A.A.V.V. *The CDF II Detector Technical Design Report.* FERMILAB-Pub-96/390-E, 1996.

[8] The CDF Collaboration. Measurement of the $t\bar{t}$ Production Cross Section in $p\bar{p}$ Collisions at $\sqrt{s} = 1.96$ TeV in the all Hadronic Decay Mode. *Phys. Rev. D74, 072005 (2006)*, 2006.

[9] A. Castro. F. Margaroli. Measurement of the top mass in the all-hadronic channel using the tmt method (1.02 fb^{-1}). *CDF Internal Note 8420*, 2006.

[10] The CDF Collaboration. Top quark mass measurement using the Template Method in the Lepton + Jet Chanel at CDF II. *CDF Internal Note 7532*, 2005.

[11] The CDF Collaboration. Measurement of the Cross Section for $t\bar{t}$ Production in $p\bar{p}$ Collisions using the Kinematics of Lepton + Jets events. *Phys. Rev. D71, 052003 (2005)*, 2005.

[12] R. Erbacher *et al.* Preliminary Event Selection and $t\bar{t}$ Signal Acceptance of the Winter 2005 Top Lepton + Jets Sample. *CDF Internal Note 7372*, 2005.

[13] Affolder *et al.* Measurement of the Top Quark mass with the Collider Detector at Fermmilab. *Phys Rev. D63 032003*, 2001.

[14] M. Giunta *et al.* Improving the Top mass measurement in L+J by using the 3 Best Combinations. *CDF Internal Note 8430*, 2006.

[15] M. Giunta et al. Reducing the top mass statistical error by using 3 reconstructed masses per event. *CDF Internal Note 8177*, 2006.

[16] G. Chlachidze G. Velev G. Bellettini, J. Budagov. Top mass analysis using 3 Best χ^2 permutations. *CDF Internal Note 6770*, 2003.

[17] A. Taffard and Top Properties Group M. Tecchio. http://www-cdf.fnal.gov/internal/physics/top/RunIITopProp/gen6/EvtSelWinter06.html.

[18] S. Budd *et al.* Mesaurement of the t-tbar Production Cross Section in SECVTX-Tagged Lepton + Jets Events. *CDF Internal Note 8037*, 2006.

[19] The CDF Collaboration. Measurement of the $t\bar{t}$ cross section in $p\bar{p}$ collisions at $\sqrt{s}$ = 1.96 TeV using lepton + jets events with secondary vertex b-tagging. *Phys. Rev. D 71, 052003*, 2005.

[20] L. Lions D. Gibaut. How to combine correlated estimates of a single physical quantity. *NIMA A270 (1988) 110-117*, 1988.

[21] The CDF Collaboration. Top quark mass measurement using the Template Method in the lepton + jet channel at CDF II. *Phys. Rev. D73, 032003*, 2006.

[22] Brian Mohr Florencia Canelli. Measurement of the top quark mass using the Matrix Element Analysis Technique in the lepton+jets channel with 940 pb^{-1}. *CDF Internal Note 8375*, 2006.

[23] The DØ Collaboration. An Improved Measurement of the Top Quark Mass. *Nature 429, 638 (2004)*, 2004.

[24] The CDF Collaboration. Measurement of the Top quark mass using the Template Method on dilepton events in $p\bar{p}$ collisions at sqrt(s)=1.96 TeV. *Phys. Rev. D 73, 112006 (2006)*, 2006.

[25] The CDF Collaboration. Measurement of the Top quark mass using Neutrino ϕ Weighting Method in the Dilepton Events at CDF. *CDF Internal Note 7759*, 2005.

[26] Kunitaka Kondo. Dynamical Likelihood Method for Reconstruction of Events with Missing Momentum. *Journal of Physics Society of Japan Vol. 57, No. 12, December 1988 pp. 4126-4140*, 1988.

[27] Gregory Mahlon and Stephen Parke. Maximizing spin correlations in top quark pair production at the tevatron. *Physics Letters B*, 411:173, 1997.